Master Thesis:
Upgrade and Calibration of Super-Kamiokande's Inner Photodetectors
(スーパーカミオカンデ光電子増倍管の改良型導入と較正)

Xia, Junjie
Department of Physics
Graduate School of Science, University of Tokyo
Student ID: 35-176375
E-mail: seanxia@icrr.u-tokyo.ac.jp
Supervisor: Prof. Kajita, Takaaki

July, 2019

Abstract

In the year of 2018∼2019, Super-Kamiokande (Super-K) has completed a detector upgrade to its 5th running phase. One of the major improvements is the 136 new Photomultiplier tubes (PMT) of better photon detection efficiency that were installed to replace the broken ones inside the tank. Those PMTs are designed for Hyper-Kamiokande (Hyper-K)—the next generation of large underground water Cherenkov experiment. Thus their operation in Super-K will be the very first step of realizing Hyper-K in the near future. Other than the measurements and tuning of those new PMTs, this work has also improved and developed new methods for the calibration of Super-K. The individual variance of PMT's charge response has been reduced by ∼75%, meanwhile the drift in photon multiplication factor has been corrected so that the present value is close to the initial one over 10 years ago. In addition, the detector timing has been calibrated with lower systematic uncertainties. The results of these calibrations are now being implemented into the physics analysis of Super-K. Meanwhile the framework and softwares developed this time will serve as a sample reference for the next upgrade in 1∼2 years, when Super-K will for the first time dissolve Gadolinium (Gd) salt into its water.

Acknowledgements

Throughout these 2 years there are many great people who have helped and guided me along the path of research. First of all, I would like to express my sincere gratitude to my advisor Prof. Takaaki Kajita who has always been patient and supportive. Other than this great experience of working at Super-K, he has also always been encouraging me to explore where my interests truly lie in. Studying and working with Prof. Kajita is really joyful with absolutely 0 stress in all discussions or group meetings we had. At the meantime I am grateful to Kimihiro Okumura-sensei and Chieko Mashima-san as well, who helped with both my research and living in Japan when Prof. Kajita was not available given to his super busy schedule.

I could never achieve the results in this work without the help from people including Prof. Shigetaka Moriyama, Yusuke Koshio-sensei, Yasuhiro Nishimura-sensei, Yasuhiro Nakajima-sensei, Patrick de Perio, and Hidekazu Tanaka-sensei. Leading the Super-K calibration group during this detector upgrade period, Prof. Moriyama was the goal keeper of the whole Super-K calibration who did not let any problem pass his supervision. From the very beginning he has kindly helped me getting familiarized with the Super-K system and working flows. Meanwhile throughout this calibration work, I have received tons of valuable suggestions from him, as well as Koshio-sensei, Nakajima-sensei, Nishimura-sensei, and Tanaka-sensei to improve the analyses. This calibration was not an easy job, and I still remember those days when I stayed in the mine overnight taking data with them. From them I have seen a physicist's academic rigor and unyieldingness. Patrick was truly a great mentor and friend of mine. Together we worked out a lot for the new calibration software and I have learned so many in coding from him.

The life in Kamioka to be honest was not so amusing, especially when one needs to drive more than 15 km for the nearest convenience store. But thanks to my friends: Akira Takenaga-san, Takumi Suzuki-san, Kouhei Okamoto-san, Nobuyuki Kato-san, Toshiki Mochizuki-san, Takeshi Okada-san, and Shuichi Imaizumi-san the time in Kamioka was memorable with free rides and parties and BBQs.

Last but not the least I would like to say thanks to all of the Super-K collaborators. Working in such a large collaboration, I still feel connected to every other colleagues for everyone was so warmhearted and easy to access. I really look forward to the future journey here as a PhD student.

Contents

List of Figures **3**

List of Tables **5**

1 Introduction **6**

2 Neutrinos **7**

2.1 The Standard Model 7

2.1.1 Neutrino Interactions in the Standard Model 7

2.1.2 Higgs Mechanism 8

2.2 Neutrino Oscillations 11

2.2.1 Three-Generation Mixing 11

2.2.2 Derivation of Neutrino Oscillations 12

2.2.3 Measurements of Neutrino Oscillations 15

3 The Super-K and Hyper-K Experiments **16**

3.1 Overview of Super-K 16

3.2 Cherenkov Radiation 17

3.3 ID and OD 19

3.3.1 Optically Separated Water Tank 19

3.3.2 The Super-K 50 cm Venetian Blind PMT 21

3.4 Water 22

3.5 Data Acquisition 24

3.6 Prospects for Hyper-K 24

4 The Hyper-K 50 cm Box&Line PMT **26**

4.1 The Box&Line Dynodes 26

4.2 High Photon Detection Efficiency 27

4.3 Charge and Time Responses 28

4.4 Gain Stability 28

4.5 Background Noises 30

5 2018 Detector Upgrade **32**

5.1 Pre-Calibration of Hyper-K 50 cm B&L PMTs 32

5.1.1 Experiment Setting up 32

5.1.2 Data Collection 35

5.1.3 Systematic Error Corrections 35

5.1.4 Measurements 39

5.2 Voltage Adjustment 43
5.2.1 Data Collection 43
5.2.2 New Voltage Determination 44
5.2.3 No Change Channels 49
5.2.4 New Voltage Results 49
5.2.5 Uncertainties 52
5.3 Timing Calibration 57
5.3.1 Overview 57
5.3.2 Time Peak Fitting 59
5.3.3 T-Q Curve Fitting 61
5.3.4 Global Timing Offset 65
5.3.5 Timing Correction Quality Checks 66
5.3.6 Bad Channels 69

6 Inputs to Super-K Detector Simulation **70**
6.1 SPE Charge Distribution for Hyper-K PMTs 70
6.2 Timing Resolution 72

7 Conclusions and Outlook **74**

References **77**

List of Figures

2.1 The Standard Model of Elementary Particles 8
2.2 The Feynman diagrams of neutrino interactions with Charged Current (left) by gauge boson $W^{\pm}$ and Neutral Current (right) by Z. 11
2.3 CPT, CP, and T transformations that relate different flavor transition channels 15
3.1 Schematic view of Super-K tank and its surroundings 17
3.2 A particle moving at speed βc emits Cherenkov light cone in a medium with refractive index $n > 1$ 18
3.3 Cherenkov radiation spectrum in water 19
3.4 Cross section of the Super-K water tank 20
3.5 Super module of PMTs 21
3.6 Super-K 50 cm PMT design and QE spectrum 22
3.7 Venetian blind dynode display and the Monte Carlo simulation of secondary electron trajectories 22
3.8 The Super-K water purification system 23
3.9 Super-K water temperature in vertical direction 23
3.10 Neutrino mass hierarchy sensitivity after 10 years of Hyper-K data collection (1.9 Mton·year exposure 25
3.11 Constraints on δ_{CP} after 10 years of Hyper-K exposure 25
4.1 Hamamatsu R12600 50 cm B&L PMT 27
4.2 Box&Line dynode layout 27
4.3 Measured QE of six 50cm B&L PMTs 28
4.4 Hyper-K B&L PMT charge and time resolution. 29
4.5 B&L PMT linearity measurement 29
4.6 B&L PMT gain stability measurements. 30
4.7 Hyper-K B&L PMT dark hits 31
5.1 Schematic view of the dark room dark room 33
5.2 Residual magnetic field at the 7 PMT positions 33
5.3 Schematic plot of the electronic circuit 34
5.4 Hyper-K 50 cm B&L PMT data samples 36
5.5 Channel variation measured by the reference PMT 37
5.6 Pedestal fluctuation over time 38
5.7 Gain stability check with the reference PMT 39
5.8 Pre-calibration voltage scan example 40
5.9 Reference PMT afterpulse rate 40
5.10 Fitted and raw data PVR 41

5.11 Measurement and selection of 145 Hyper-K 50 cm PMTs 42
5.12 Schematic view of voltage adjustment experimental set up 44
5.13 The spiky feature of SPE charge distribution 45
5.14 Effect of bin width on the spiky feature 46
5.15 Super-K PMT SPE fitting example with exponential tail 47
5.16 Super-K PMT SPE fitting example with error function skewed Gaussian 48
5.17 Hyper-K PMT SPE fitting example with error function modified Gaussian 48
5.18 Voltage scan examples for 3 generations of PMT 50
5.19 Example of rejected PMT from the voltage scan 50
5.20 Gain comparison for SK-IV and SK-V 51
5.21 The average voltage curves of 3 PMT generations and the adjusted SK-V voltages 52
5.22 ϕ dependence check for SPE peaks 53
5.23 Occupancy dependence check for SPE peaks 55
5.24 The systematic and statistical uncertainties from fitting of SPE peak. . . 56
5.25 SPE peak check from the 2 different processes 56
5.26 Time walk effect demonstration 58
5.27 Timing calibration set ups 58
5.28 Example of time-charge 2-D display 60
5.29 The smearing effect to the time peak in the 2nd Q bin 61
5.30 The difference in time peak between the raw and smeared data 61
5.31 Examples of raw time data peak fitting 62
5.32 T-Q curve fitting problem in empty Q bins 62
5.33 Extrapolation example with PMT channel 9999 64
5.34 Determination of the 0 order constant in T-Q curve. 64
5.35 Global timing difference between the 2 TQ maps 65
5.36 The difference between data and fitting in all Q bins of PMT 00014 . . . 66
5.37 Data&fitting agreement check of all ID PMTs 67
5.38 Verification of the time walk effect correction 67
5.39 Comparison to LINAC data taken during SK-IV 68
5.40 Example of scattered distribution in T-Q 2-D display. 69
6.1 Ni-Cf data of Hyper-K PMTs 71
6.2 Fitting the SPE charge distribution of Hyper-K PMTs with Ni-Cf data . 72
6.3 Fitting of the integrated timing distribution of Super-K and Hyper-K PMTs. 73
6.4 The timing resolutions of Super-K and Hyper-K PMTs 74

List of Tables

2.1 Latest measurements of the neutrino mixing angles and mass squared difference. . . . 16
3.1 The Super-K running periods. The last column shows the corresponding front-end electronic system of each phase. . . . 18
3.2 QBEE system specifications [20] . . . 24
4.1 Minimum requirements of the Hyper-K ID PMTs from [21]. . . . 26
5.1 Currents and voltages applied to each pair of Helmholtz coils in all 3 spatial directions. . . . 34
5.2 The coordinates of the diffuser ball in the tank. . . . 44
5.3 Run information of the SN-LD data. The 3rd column shows the voltage difference of each PMT from the SK-IV setting. . . . 45
5.4 The breakdowns of 62 no change PMTs in the voltage adjustment. . . . 49
5.5 The voltage curve parameter averages of 3 PMT generations. . . . 51
5.6 Sinusoidal function fitting results of SPE peak ϕ dependences. . . . 53
5.7 Systematic and statistical uncertainties in SPE peak for the 3 PMT generations. . . . 55
5.8 The differences in average SPE peak calculated by charge peak - ADC count converted peak. The first column represents the voltage setting for each row. The 3 generations of PMT are also listed. The peak differences are written in units of pC. . . . 57
5.9 Averages of the fitted parameters from the time walk effect corrected T-Q data of all ID PMTs. The standard deviation in each parameter was assigned as the uncertainty. . . . 68
5.10 PMT channels with similar feature to Figure 5.40. In the "largely scatterd" case the data were too scattered that no T-Q curve could be fitted. In the "less severe" case there were some small "blobs" of scatter but still a usable T-Q curve could be fitted. . . . 69

1 Introduction

Neutrino, a neutral lepton that only interacts through the weak coupling and gravitational force, has been one of the most popular topics of particle physics study for generations of people. Thanks to its low interaction rate, a neutrino may survive an extremely long distance to an observer, which makes it a good messenger of astrophysical sources where other particles are easily scattered and absorbed along the track. However, the exact same merit also makes it incredibly hard to detect. Over the past several decades, the progress in neutrino physics study was prominent. The observation of Supernova 1987A's neutrino by Kamiokande experiment [1] has manifested the great potential of neutrinos in astrophysics research. Later on the neutrino oscillation proven by Super-K experiment [2] and SNO experiment [3] has opened a gate to new physics beyond the Standard Model.

Started in 1996, Super-K has been pioneering in neutrino observation for more than 20 years. In 2018, it has ended its longest running period, which lasted for more than 10 years, for a full scale detector upgrade. One of the major purposes was to prepare Super-K for the future operation with Gd dissolved water, or so called SK-Gd. The upgrade started in June 2018 and ended in January 2019, with a variety of refurbishments finished including a new water circulation system, leakage proof upgrading, rust and dust removal inside the tank, PMT replacement, etc. In total there were 136 PMTs installed to replace the dead channels of Super-K Inner Photodetector (ID). Those new PMTs are Hamamatsu R12860 50cm Box&Line PMTs, which are designed for the next generation experiment—Hyper-Kamiolande (Hyper-K).

Chapter 2 gives a summary of the Standard Model, the Higgs mechanism and Electroweak symmetry breaking, and the theoretical background and experimental measurements of neutrino oscillations.

Chapter 3 briefly introduces the Super-K experiement and its successor Hyper-K, with their design and detection mechanism. Meanwhile Chapter 4 focuses on various advantages of the new 50cm B&L PMT.

A detailed description about the 2018 detector upgrade is given in Chapter 5. section 5.1 describes the measurement and quality check of 50cm B&L PMTs before their installation. Section 5.2 and 5.3 talk about the major calibration tasks involved in this work respectively—the voltage adjustment and timing calibration of all ID channels after the installation of new PMTs.

Finally Chapter 6 talks about the application of calibration data from this work to Super-K's Monte Carlo (MC) simulation and its implication for the future analysis.

2 Neutrinos

This section introduces the physics and mathematical backgrounds of the Standard Model and neutrino oscillation. Most of the discussion follows the books by C. Giunti and C. W. Kim [4], M. Srednicki [5], and M. Thompson [6].

2.1 The Standard Model

The Standard Model of particle physics is the theory describing three fundamental forces: the electromagnetic, weak and strong couplings, and the elementary particles involved in these interactions. As shown in Figure 2.1, the particles composing matters are named fermions meanwhile the fundamental force carriers are named bosons. In the family of fermions the particles can be further divided into 2 groups according to their electric charges, i.e. quarks with fractional charges (+2/3 or -1/3) and leptons with integer charges (-1 or 0). Besides the 12 fermions shown in Figure 2.1, each has its own antiparticle with exactly opposite electric charge except for neutrinos. Therefore all the charged fermions are known as Dirac fermions given to the discrepancy between their antiparticles and themselves, while it is still unclear whether neutrinos are Majorana or Dirac fermions.

2.1.1 Neutrino Interactions in the Standard Model

For the lepton sector of the Standard Model, 2 fundamental forces are available: electromagnetic interaction mediated by photon and weak by $W^{\pm}$ and Z bosons. The aforementioned 4 gauge bosons arises from the spontaneous symmetry breaking of electroweak symmetry $SU(2) \times U(1)$ through the Higgs Mechanism. After the symmetry breaking, electromagnetic interaction acts on a particle's charge eigenstate, while weak interaction acts on flavor. Therefore due to the lack of a finite charge, neutrinos can only interact through the weak forces as shown by Figure 2.2, in which the $l^{\mp}$ represents all 3 generations of the charged leptions (anti-leptons) and $\nu_l(\bar{\nu}_l)$ represents the corresponding neutrino (anti-neutrino). To conserve the lepton number in one interaction, neutrino ν_l can only interact with lepton l^-, while anti-neutrino $\bar{\nu}_l$ is only associated with anti-charged lepton l^+.

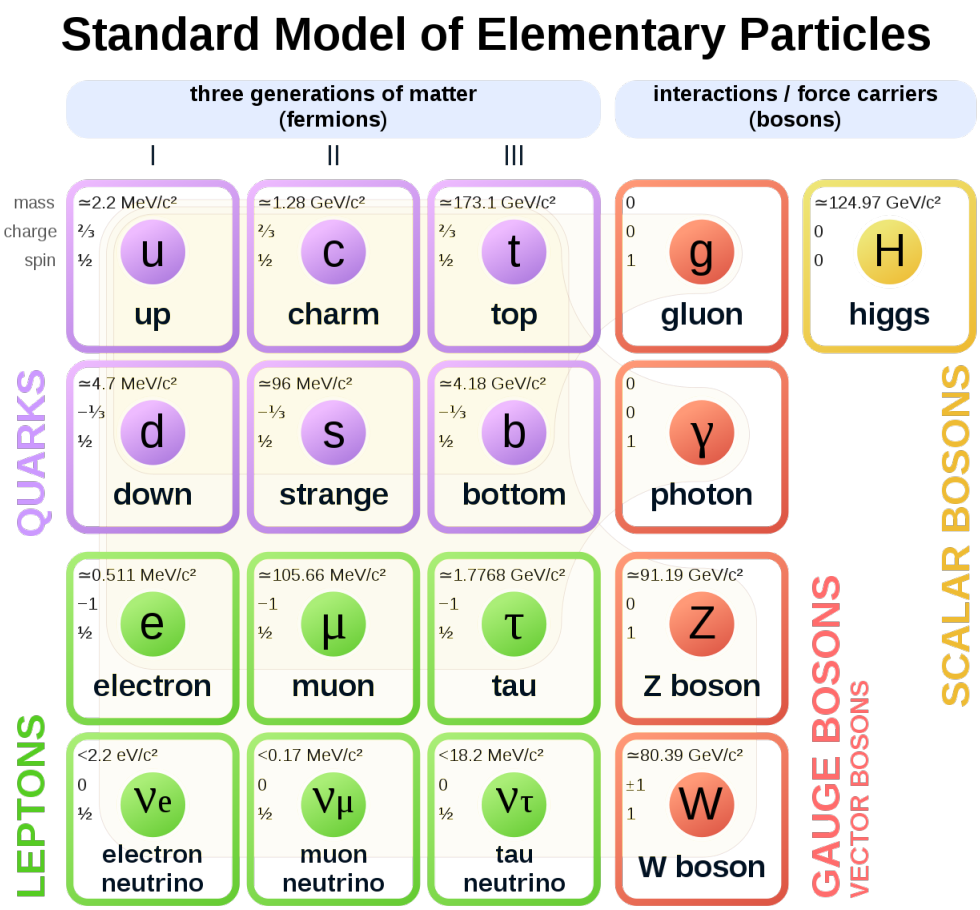

Figure 2.1: The Standard Model of Elementary Particles [7]

2.1.2 Higgs Mechanism

To understand why such interactions shown in Figure 2.2 are so "weak", we can start with the minimal Higgs model of 2 complex scalar fields in weak isospin doublet:

$$\phi = \begin{pmatrix} \phi^+ \\ \phi^0 \end{pmatrix} = \frac{1}{\sqrt{2}} \begin{pmatrix} \phi_1 + i\phi_2 \\ \phi_3 + i\phi_4 \end{pmatrix} \tag{2.1}$$

where ϕ^0 is a neutral scalar field and differs from the charged field ϕ^+ by 1 unit of charge. The Lagrangian for this doublet is

$$\mathcal{L} = (\partial_\mu \phi)^\dagger (\partial^\mu \phi) - V(\phi) \tag{2.2}$$

where $V(\phi)$ is the Higgs potential

$$V(\phi) = \mu^2 \phi^\dagger \phi + \lambda (\phi^\dagger \phi)^2$$

For negative μ^2, at the potential minimum the fields satisfies

$$\phi^\dagger\phi = \frac{1}{2}(\phi_1^2 + \phi_2^2 + \phi_3^2 + \phi_4^2) = \frac{v^2}{2} = -\frac{\mu^2}{2\lambda}$$

Since photon after symmetry breaking is massless, the minimum of the Higgs potential must be non-zero for the neutral field ϕ^0. Expanding this field about the minimum with the Higgs field $h(x)$ while removing the Goldstone fields by gauge transformation gives

$$\phi(x) = \frac{1}{\sqrt{(2)}}\begin{pmatrix} 0 \\ v + h(x) \end{pmatrix}$$

To find the masses of gauge bosons and the interaction terms in the resulted Lagrangian, or Salam-Weinberg model, first switch the derivative in Eq.2.2 to a covariant one

$$\partial_\mu \to D_\mu = \partial_\mu + ig_W \mathbf{T}\cdot\mathbf{W}_\mu + ig'\frac{Y}{2}B_\mu \tag{2.3}$$

where $\mathbf{T} = \frac{1}{2}\sigma$ are the $SU(2)$ symmetry generators. According to the Glashow-Salam-Weinberg model, the hypercharge of Higgs doublet $Y = 1$. From

$$D_\mu\phi = \frac{1}{2\sqrt{(2)}}\begin{pmatrix} 2\partial_\mu + ig_W W_\mu^{(3)} + ig'B_\mu & ig_W[W_\mu^{(1)} - iW_\mu^{(2)}] \\ ig_W[W_\mu^{(1)} + iW_\mu^{(2)}] & 2\partial_\mu - ig_W W_\mu^{(3)} + ig'B_\mu \end{pmatrix}\begin{pmatrix} 0 \\ v + h \end{pmatrix} \tag{2.4}$$

the $(D_\mu\phi)^\dagger(D^\mu\phi)$ term in the Lagrangian that determines gauge bosons masses turns out to be

$$\underbrace{\frac{1}{8}v^2 g_W^2\left(W_\mu^{(1)}W^{(1)\mu} + W_\mu^{(2)}W^{(2)\mu}\right)}_{W^\pm} + \underbrace{\frac{1}{8}v^2\left(g_W W_\mu^{(3)} - g'B_\mu\right)\left(g_W W^{(3)\mu} - g'B^\mu\right)}_{Z,\gamma} \tag{2.5}$$

Through the symmetry breaking $W^{(1)}$ and $W^{(2)}$ Goldstone bosons combine into the $W^\pm$ bosons of weak interaction, and $W^{(3)}$ and B ended up with the Z boson and photom γ.

Since the mass term of scalar field in the Lagrangian are

$$\frac{1}{2}m_W^2 W_\mu^{(1)}W_\mu^{(1)} \text{ and } \frac{1}{2}m_W^2 W_\mu^{(2)}W_\mu^{(2)}$$

the mass of the W Goldstone boson is therefore

$$m_W = \frac{1}{2} g_W v \tag{2.6}$$

which is determined by the coupling constant of the $SU(2)_L$ gauge interaction g_W and the Higgs field vacuum expectation value. The two W Goldstone bosons construct the basis of charged $W^{\pm}$ bosons through a linear combination:

$$W^{\pm} = \frac{1}{\sqrt{2}}(W^{(1)} \mp iW^{(2)})$$

Meanwhile the masses of the other 2 Goldstone bosons can be found by diagonalizing the matrix

$$\begin{pmatrix} g_W^2 & -g_W g' \\ -g_W g' & g'^2 \end{pmatrix}$$

After diagnolization the second part in Eq. 2.5 can be rewritten in the diagonal basis (A_μ, Z_μ) by

$$\frac{1}{8} v^2 \begin{pmatrix} A_\mu & Z_\mu \end{pmatrix} \begin{pmatrix} 0 & 0 \\ 0 & g_W^2 + g'^2 \end{pmatrix} \begin{pmatrix} A^\mu \\ Z^\mu \end{pmatrix}$$

where

$$\begin{aligned} A_\mu &= \frac{g' W_\mu^{(3)} + g_W B_\mu}{\sqrt{g_W^2 + g'^2}} \\ &= \cos\theta_W B_\mu + \sin\theta_W W_\mu^{(3)} \\ Z_\mu &= \frac{g_W W_\mu^{(3)} - g' B_\mu}{\sqrt{g_W^2 + g'^2}} \\ &= -\sin\theta_W B_\mu + \cos\theta_W W_\mu^{(3)} \end{aligned}$$

Relating the interaction term from the diagonal basis to the corresponding mass term in the Lagrangian and find

$$m_A = 0 \ \text{ and } \ m_Z = \frac{1}{2} v \sqrt{g_W^2 + g'^2} \tag{2.7}$$

which can be identified as the massless photon and massive Z boson in the flavor basis.

Thus as shown by Eq. 2.6 & Eq. 2.7, the weak interaction gauge bosons $W^{\pm}$ and Z gain their masses from the Higgs field. With the experimental measurements for the two masses at around 80 GeV and 91 GeV respectively, the coupling constant of weak interaction is accordingly much smaller than that of the electromagnetic interaction due to the $\frac{1}{-q^2-m^2}$ dependence of the propagator.

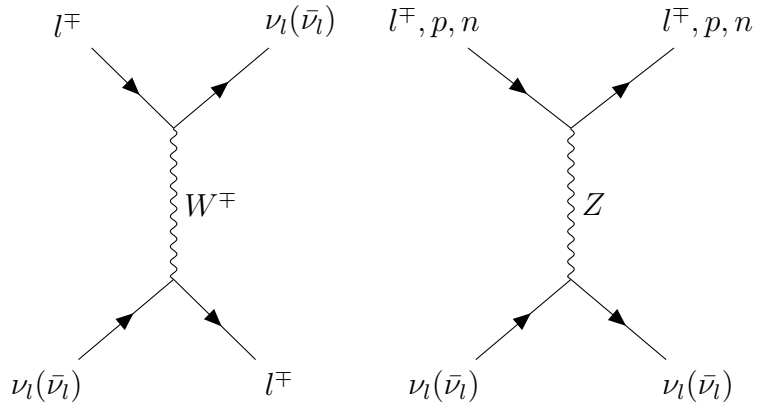

Figure 2.2: The Feynman diagrams of neutrino interactions with Charged Current (left) by gauge boson $W^{\pm}$ and Neutral Current (right) by Z.

2.2 Neutrino Oscillations

The Standard Model has predicted neutrinos as massless, left handed fermions. However, with multiple experiments having verified the non-zero probability of neutrino oscillations, it becomes obvious that neutrinos are massive particles. So far the neutrino oscillation has remained as the only experimentally verified phenomenon beyond the scope of the Standard Model.

2.2.1 Three-Generation Mixing

The reason of neutrino oscillation originates from the difference in 2 eigenbases. In the Standard Model, there are 3 flavor eigenstates of neutrinos forming a complete orthonormal basis: ν_e, ν_μ, and ν_τ, labeled according to their partner charged leptons in a Charged Current (CC) weak interaction. Meanwhile, one can also construct a mass eigenbasis for the free particle Hamiltonian: ν_1, ν_2, and ν_3. It has been verified that these 2 bases are not the same. The rotation matrix linking on to the other can be written as

$$\begin{pmatrix} \nu_e \\ \nu_\mu \\ \nu_\tau \end{pmatrix} = \begin{pmatrix} U_{e1} & U_{e2} & U_{e3} \\ U_{\mu 1} & U_{\mu 2} & U_{\mu 3} \\ U_{\tau 1} & U_{\tau 2} & U_{\tau 3} \end{pmatrix} \begin{pmatrix} \nu_1 \\ \nu_2 \\ \nu_3 \end{pmatrix} \tag{2.8}$$

where the mixing matrix U is named the PMNS matrix after Pontecorvo, Maki, Nakagawa, and Sakata in reverence to their contributions to the neutrino mixing model.

In Eq.2.8, only 3 generations of neutrino are considered. Note that the degree of the eigenbasis can be larger than 3 with the existence of sterile neutrinos, which are candidate sources of the neutrino masses. In the three-generation case of the Standard Model, the PMNS matrix can be further parameterized by 3 mixing angles θ_{12}, θ_{23}, θ_{13}, and 1 CP-violating δ_{CP} phase in the case of Dirac neutrinos or 2 phases λ_2, λ_3 of Majorana neutrinos.

$$
\begin{aligned}
U &= \begin{pmatrix} U_{e1} & U_{e2} & U_{e3} \\ U_{\mu 1} & U_{\mu 2} & U_{\mu 3} \\ U_{\tau 1} & U_{\tau 2} & U_{\tau 3} \end{pmatrix} \\
&= \begin{pmatrix} c_{12}c_{13} & s_{12}c_{13} & s_{13}e^{-i\delta_{CP}} \\ -c_{23}s_{12} - s_{23}c_{12}s_{13}e^{i\delta_{CP}} & c_{23}c_{12} - s_{23}c_{12}s_{13}e^{i\delta_{CP}} & s_{23}c_{13} \\ s_{23}s_{12} - c_{23}c_{12}s_{13}e^{i\delta_{CP}} & -s_{23}c_{12} - c_{23}s_{12}s_{13}e^{i\delta_{CP}} & c_{23}c_{13} \end{pmatrix} \begin{pmatrix} 1 & 0 & 0 \\ 0 & e^{-i\frac{\lambda_2}{2}} & 0 \\ 0 & 0 & e^{-i\frac{\lambda_3}{2}} \end{pmatrix} \\
&= \begin{pmatrix} 1 & 0 & 0 \\ 0 & c_{23} & s_{23} \\ 0 & -s_{23} & c_{23} \end{pmatrix} \begin{pmatrix} c_{13} & 0 & s_{13}e^{-i\delta_{CP}} \\ 0 & 1 & 0 \\ -s_{13}e^{-i\delta_{CP}} & 0 & c_{13} \end{pmatrix} \begin{pmatrix} c_{12} & s_{12} & 0 \\ -s_{12} & c_{12} & 0 \\ 0 & 0 & 1 \end{pmatrix} \underbrace{\begin{pmatrix} 1 & 0 & 0 \\ 0 & e^{-i\frac{\lambda_2}{2}} & 0 \\ 0 & 0 & e^{-i\frac{\lambda_3}{2}} \end{pmatrix}}_{\text{exists only if Majorana neutrinos}}
\end{aligned}
$$

where $c_{ij} = \cos\theta_{ij}$ and $s_{ij} = \sin\theta_{ij}$ for $(i, j = 1, 2, 3)$.

2.2.2 Derivation of Neutrino Oscillations

Since the neutrino mass states $|\nu_k\rangle$ are eigenstates of Hamiltonian with energy eigenvalue E_k, the Schrodinger equation

$$i\frac{d}{\mathrm{d}t}|\nu_k(t)\rangle = \mathcal{H}|\nu_k(t)\rangle$$

implies that the neutrino mass evolve in time as plane waves:

$$|\nu_k(t)\rangle = e^{-iE_k t}|\nu_k\rangle \quad (k = 1, 2, 3) \tag{2.9}$$

Yet since the flavor eigenstates are the observables, applying the PMNS matrix on the mass eigenstates to map to the flavor states

$$|\nu_\alpha(t)\rangle = \sum_k U^*_{\alpha k} e^{-iE_k t} |\nu_k\rangle \quad (\alpha = e, \mu, \tau) \tag{2.10}$$

such that

$$|\nu_\alpha(t=0)\rangle = \sum_k U^*_{\alpha k} |\nu_k\rangle = |\nu_\alpha\rangle$$

Using the unitary relation $U^\dagger U = \mathbf{1}$ and rewrite the mass states as a combination of flavor states

$$|\nu_k\rangle = \sum_\alpha U_{\alpha k} |\nu_\alpha\rangle \tag{2.11}$$

Substituteing Eq.2.10 with Eq.2.11 gives

$$|\nu_\alpha(t)\rangle = \sum_{\beta=e,\mu,\tau} \Big(\sum_k U^*_{\alpha k} e^{-iE_k t} U_{\beta k} \Big) |\nu_\beta\rangle \tag{2.12}$$

Thus, the initial single flavor state $|\nu_\alpha\rangle$ becomes a superposition of different flavor states at $t > 0$ given to the non-diagonality of the PMNS matrix U. The transition probability is then

$$\begin{aligned} P_{\nu_\alpha \to \nu_\beta}(t) &= |\, \langle \nu_\beta | \nu_\alpha(t) \rangle \,|^2 \\ &= \sum_{k,j} U^*_{\alpha k} U_{\beta k} U^*_{\alpha j} U_{\beta j} e^{-i(E_k - E_j)t} \\ &= \sum_{k,j} U^*_{\alpha k} U_{\beta k} U_{\alpha j} U^*_{\beta j} \exp\Big(\frac{-i\Delta m^2_{kj} t}{2E} \Big) \end{aligned} \tag{2.13}$$

where in the case of ultra-relativistic neutrino

$$\begin{aligned} E_k &= \sqrt{\mathbf{p}^2 + m_k^2} \approx E + \frac{m_k^2}{2E} \\ E &= |\mathbf{p}| \\ \Delta m^2_{kj} &= m^2_k - m^2_j \end{aligned}$$

However since a neutrino's travel time is usually unknown in experiment, it is practical to substitute $t = L$ since the speed of neutrino's approximates the speed of light c. Thus

$$P_{\nu_\alpha \to \nu_\beta}(L,E) = \sum_{k,j} U^*_{\alpha k} U_{\beta k} U_{\alpha j} U^*_{\beta j} \exp\Big(\frac{-i\Delta m^2_{kj} L}{2E}\Big) \tag{2.14}$$

Therefore by observing the non-zero probability of neutrino oscillations, one can measure the 3 mixing angles θ_{12}, θ_{23}, and θ_{13} of the PMNS matrix as well as the mass squared difference Δm^2_{ij} among the 3 neutrino generations.

The oscillation of anti-neutrinos can be derived in a similar way. Again starting from the rotation between flavor and mass eigenbasis of anti-neutrinos

$$|\bar{\nu}_\alpha\rangle = \sum_k U_{\alpha k} |\bar{\nu}_k\rangle \tag{2.15}$$

one can finally achieve the transition probability of anti-neutrinos as

$$P_{\bar{\nu}_\alpha \to \bar{\nu}_\beta}(L,E) = \sum_{k,j} U_{\alpha k} U^*_{\beta k} U^*_{\alpha j} U_{\beta j} \exp\Big(\frac{-i\Delta m^2_{kj} L}{2E}\Big) \tag{2.16}$$

The difference between neutrino and anti-neutrino oscillation probabilities can be seen easily if rearranging Eq.2.14 and Eq.2.16 into

$$\begin{aligned} P_{\nu_\alpha \to \nu_\beta}(L,E) = \delta_{\alpha\beta} &- 4 \sum_{k>j} \mathrm{Re}\left[U^*_{\alpha k} U_{\beta k} U_{\alpha j} U^*_{\beta j}\right] \sin^2\Big(\frac{-i\Delta m^2_{kj} L}{4E}\Big) \\ &+ 2 \sum_{k>j} \mathrm{Im}\left[U^*_{\alpha k} U_{\beta k} U_{\alpha j} U^*_{\beta j}\right] \sin\Big(\frac{-i\Delta m^2_{kj} L}{2E}\Big) \end{aligned} \tag{2.17}$$

and

$$\begin{aligned} P_{\bar{\nu}_\alpha \to \bar{\nu}_\beta}(L,E) = \delta_{\alpha\beta} &- 4 \sum_{k>j} \mathrm{Re}\left[U^*_{\alpha k} U_{\beta k} U_{\alpha j} U^*_{\beta j}\right] \sin^2\Big(\frac{-i\Delta m^2_{kj} L}{4E}\Big) \\ &- 2 \sum_{k>j} \mathrm{Im}\left[U^*_{\alpha k} U_{\beta k} U_{\alpha j} U^*_{\beta j}\right] \sin\Big(\frac{-i\Delta m^2_{kj} L}{2E}\Big) \end{aligned} \tag{2.18}$$

As shown in Figure 2.3, the CP transformation changes the $\nu_\alpha \to \nu_\beta$ to $\bar{\nu}_\alpha \to \bar{\nu}_\beta$. Since the PMNS matrix is complex, it will naturally lead to the violation of CP symmetry for $\alpha \neq \beta$ as the imaginary part differs between the $P_{\nu_\alpha \to \nu_\beta}$ and $P_{\bar{\nu}_\alpha \to \bar{\nu}_\beta}$ in Eq.2.17 and Eq.2.18. Such a violation can be checked by comparing the appearance and disappearance of neutrino

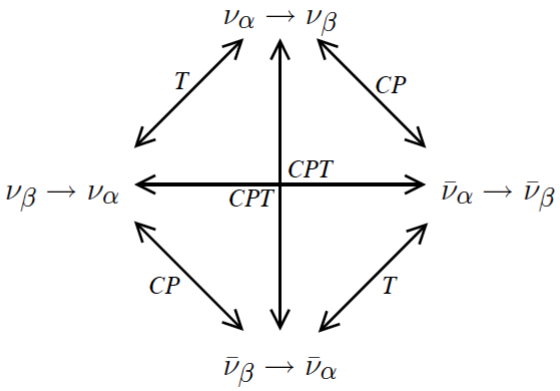

Figure 2.3: CPT, CP, and T transformations that relate different flavor transition channels. [4]

and anti-neutrino in the same flavor transition channel, with precise measurement of the energy and momentum of particles.

The CP asymmetry can be written as

$$A^{CP}_{\alpha\beta} = 4 \sum_{k>j} \mathrm{Im}\left[U^*_{\alpha k} U_{\beta k} U_{\alpha j} U^*_{\beta j}\right] \sin\left(\frac{-i\Delta m^2_{kj} L}{2E}\right) \tag{2.19}$$

which only depends on the Dirac phase δ_{CP} in the mixing matrix since E and L can be controlled as the same for neutrino and anti-neutrino. Therefore it is another mixing parameter that is under intense study at present.

2.2.3 Measurements of Neutrino Oscillations

In general, the current facilities being used for neutrino oscillation measurement can be categorized by the origin of target. One is for the atmospheric, solar, and cosmic neutrinos that are generated in nature, the other is for the artificial neutrinos from nuclear reactor or particle accelerators. For example, Super-K simultaneously collects solar, atmospheric and beamline neutrino data, meanwhile keeps monitoring the neutrino outburst from supernovae, γ-ray bursts, and other cosmic sources. For any of the neutrino sources, the determinant factor of sensitivity to the mass squared difference Δm^2 is the ratio of $\frac{L}{E}$ as shown in Eq.2.14. For example, the transition baseline of solar neutrinos will be the distance between the sun and the earth, which is about 10^{11} m. Meanwhile the solar neutrinos are typically of an energy range of 0.1$\sim$10 MeV [8], which gives a sensitivity to $\Delta m^2 \gtrapprox 10^{-12}\mathrm{eV}^2$.

As mentioned in Section 2.2.2, the mixing angles θ_{ij} and Dirac phase δ_{CP} are sensi-

$\sin^2\theta_{12}$	0.307 ± 0.013
$\sin^2\theta_{13}$	$(2.12 \pm 0.08) \times 10^{-2}$
$\sin^2\theta_{23}$	$0.421^{+0.033}_{-0.025}$ (IH, quad. I)
	$0.592^{+0.023}_{-0.030}$ (IH, quad. II)
	$0.417^{+0.025}_{-0.028}$ (NH, quad. I)
	$0.597^{+0.024}_{-0.030}$ (NH, quad. II)
Δm^2_{21}	$(7.53 \pm 0.18) \times 10^{-5}\text{eV}^2$
Δm^2_{32}	$(-2.56 \pm 0.04) \times 10^{-3}\text{eV}^2$ (IH)
	$(2.51 \pm 0.05) \times 10^{-3}\text{eV}^2$ (NH)

Table 2.1: Latest measurements of the neutrino mixing angles and mass squared difference.

tive to the neutrino oscillations and have been measured by a variety of experiments. Table 2.1 summarizes the latest constraints on the mixing angles and mass squared difference from [9]&[10]. The precise result of the mixing angles θ_{ij} plays a critical role in the determination of neutrino mass hierarchy, i.e. either it is a Normal Hierarchy (NH) where $m_1 < m_2 < m_3$ or an Inverted Hierarchy (IH) $m_3 < m_1 < m_2$. On the other hand, the possible CP violation may be the key to understand the Baryonic asymmetry of the universe. Although still with some ambiguity, recently T2K experiment has excluded the CP-conserving value of δ_{CP} by 2σ confidence level [11].

3 The Super-K and Hyper-K Experiments

This chapter describes the Super-K detector in details and also the design plan of Hyper-K experiment. The two experiments share the same scientific goal—searching for proton decay and observing neutrinos from both natural and artificial sources as mentioned in Section 2.2.3. But Hyper-K is expected to be over 8 times more efficient in statistic accumulation than Super-K.

3.1 Overview of Super-K

The Super-K detector lies about 1000 m beneath the peak of Mt. Ikenoyama, Gifu Prefecture, Japan. The overburden rock shields cosmic rays of energy lower than 1.3 TeV, helping to reduce the background noise in the detector [12]. The stainless steel cylindrical water tank has a diameter of 39 m and height of 42 m, containing in total 50,000 tons of water. Figure 3.1 illustrates the schematic view of the Super-K facilities. To mitigate the geomagnetic field in the tank, which can cause systematic bias in the

measurement, 26 sets of horizontal and vertical Helmholtz coils are mounted to the tank's inner suface. With the current applied in the Helmholtz coils, the average magnetic field inside the tank has been reduced from 450 mG to 50 mG measured in air [12].

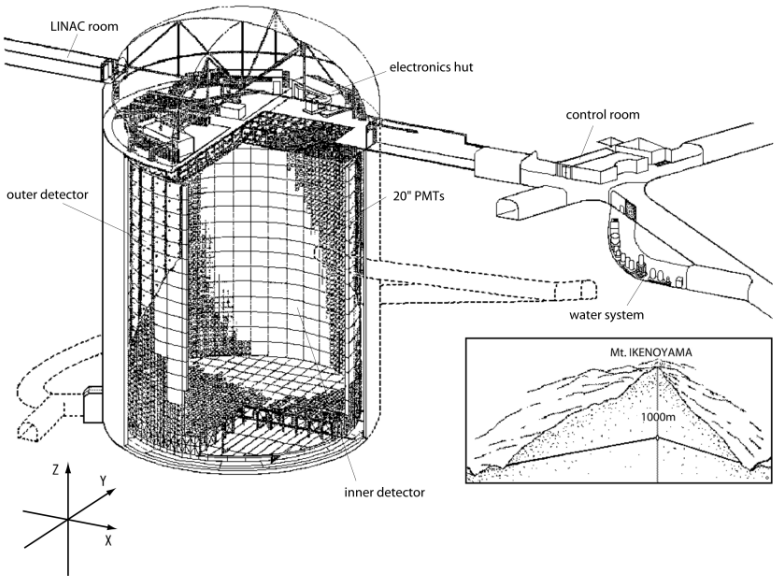

Figure 3.1: Schematic view of Super-K tank and its surroundings [13].

There were 4 running periods done in Super-K and the 5th current one is therefore called SK-V. A chronological summary of the Super-K running period prior to SK-V is given in Table 3.1. During the water refilling in 2002 after the maintenance work, an implosion of a single ID PMT happened under water and destroyed more than half of the PMTs by the shock wave. This caused the ID Photo-Coverage rate dropping to 19% during the SK-II period, during which only about half of the PMTs were operating. The replacement of all broken PMTs was finished by 2006. To prevent such a tragedy from happening again, a Fibre-reinforced plastic (FRP) case was attached to each PMT for protection. In 2008, the front-end electronics has been upgraded from Analog-Timing-Module (ATM) to QTC (charge to time)-Based Electronics with Ethernet (QBEE). The latter is currently in use in SK-V.

3.2 Cherenkov Radiation

To detect the particle interaction happening inside the water tank, Super-K searches for light cones that causes rings of hits in the PMTs. From the topological feature of the ring and its number of photons, the incoming particle's direction, vertex position, and momentum can be reconstructed. Such a light cone that provides crucial information of physics observation originates from the Cherenkov radiation of moving charged particles in water.

SK-I	Apr, 1996 - Jul, 2001	40% ID Photo-Coverage	ATM
SK-II	Oct, 2002 - Oct, 2005	19% ID Photo-Coverage	ATM
SK-III	Jul, 2006 - Sep, 2008	40% ID Photo-Coverage	ATM
SK-IV	Sep, 2008 - Jun, 2018	40% ID Photo-Coverage	QBEE

Table 3.1: The Super-K running periods. The last column shows the corresponding front-end electronic system of each phase.

Although the speed limit of moving objects by the speed of light c in vacuum is well established [14], it is still possible that an ultra-relativistic charged particle can move faster than light in some medium like water since c is reduced in this case. The signature of such a phenomenon is a conical wave front of light emitted from the particle as shown in Figure 3.2, which was first predicted by Oliver Heaviside in the 19th century [15]. The experimental observation was first done by the Soviet physicist Pavel Cherenkov in 1934 [16], and therefore named after him.

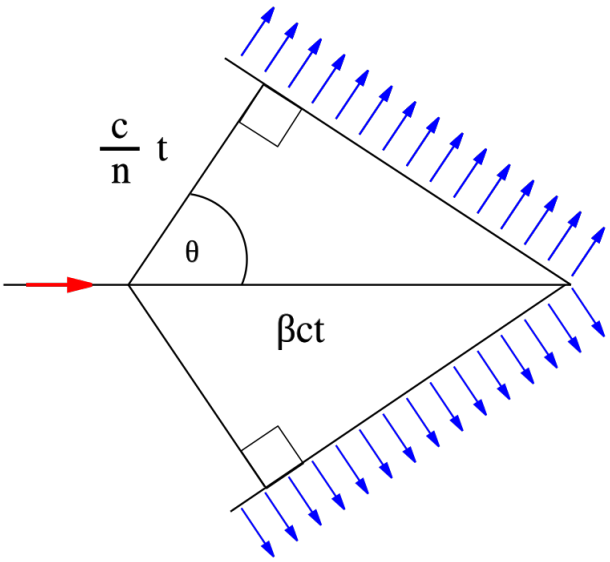

Figure 3.2: A particle moving at speed βc (direction indicated by the red arrow) emits Cherenkov light cone (blue arrows) in a medium with refractive index $n > 1$ [17]

.

From Figure 3.2 the relation of Cherenkov light cone opening angle and the speed of particle can be related as

$$\cos\theta_C = \frac{1}{n\beta} \tag{3.1}$$

where β is the ratio of particle's speed to the speed of light in vacuum. It is clear to see

that opening angle can only be greater than 0 in the limit of

$$n\beta > 1$$

Therefore the ability of a particle to produce Cherenkov radiation in a medium is determined by its own kinetic energy. In the case of pure water whose refractive index is $n \approx 1.34$, the Cherenkov light cone produced by an ultra-relativistic particle with $\beta \approx 1$ is roughly 42°.

The number of photons emitted per unit length per unit wavelength is formulated by

$$\frac{\mathrm{d}^2 N}{\mathrm{d}L\mathrm{d}\lambda} = \frac{2\pi\alpha}{\lambda^2}\Big(1 - \frac{1}{\beta^2 n(\lambda)^2}\Big) = \frac{2\pi\alpha}{\lambda^2}\sin^2\theta_C \tag{3.2}$$

where α is the fine structure constant, L the distance traveled by the particle, and λ the wavelength. The Cherenkov radiation spectrum in water of wavelength range 300∼600 nm is shown in Figure 3.3.

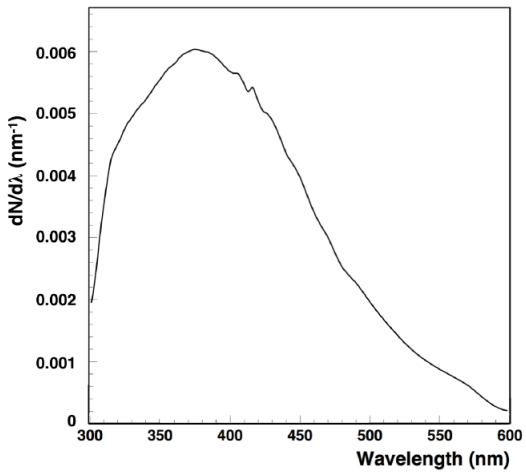

Figure 3.3: Cherenkov radiation spectrum in water from [13].

3.3 ID and OD

The Super-K tank is optically separated into the ID and OD (stands for Outer-Photodetector). This section will discuss the reason of this design and how the ID and OD work together for physics observation. Most of the details in this chapter from this section are taken from ref. [12].

3.3.1 Optically Separated Water Tank

A cylindrical stainless-steel frame, mounted with 11,146 inward-facing 50 cm PMTs (Hamamatsu R3600) called ID and 1885 outward-facing 20 cm PMTs (Hamamatsu R1408,

partially replaced during the 2018 detector upgrade) called OD, divides the tank into 2 sections with water freely flow in between. This is to further improve the selection of Cherenkov radiating particle originated in the tank aprart from the through going cosmic muons, which will be also detected and vetoed by the OD. The inner section is 33.8 m in diameter and 36.2 m in height, meanwhile there is slightly more than 2.5 m of water outside each surface of the frame. The region with more than 2 m away from the frame inside ID is a special section, because only the interactions in this region are "fully contained (FC)" events being used for real physics analysis. The FC section contains 22,000 tons of water. On the other hand, since the PMT-supporting frame itself is about 55 cm thick, it causes a dead zone that is not monitored by either the ID or OD. Figure 3.4 shows the schematic view of ID and OD inside the tank.

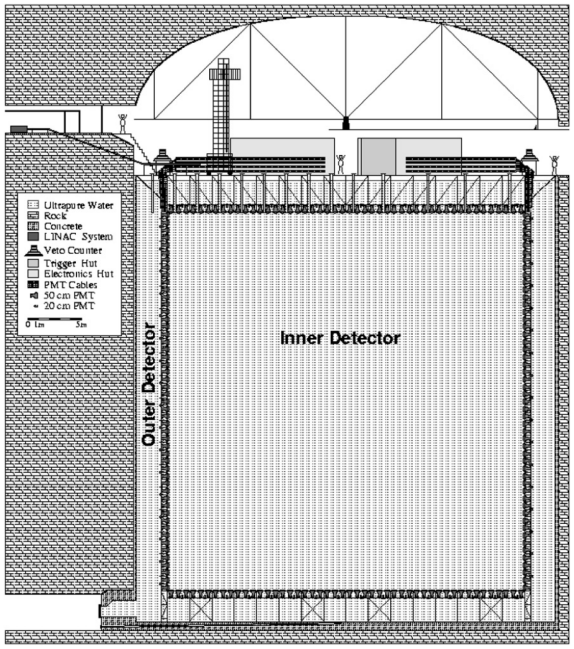

Figure 3.4: Cross section of the Super-K water tank [12]

The ID PMTs are grouped into 3×4 arrays in one super module of the stainless-steel frame as shown in Figure 3.5. On the side of ID PMTs, opaque black polyethylene telephthalate sheets are used to prevent the light leaking from the inner tank into the outer. At the same time they also help to absorb the residual photons from the radioactivity in the back of PMTs. On the side of OD, each PMT is attached with a Wavelength-Shifting (WS) plate made by acrylic to enhance its light collection efficiency. Meanwhile all of the OD frame surface is covered with a reflective layer made from Tyvek® sheets. The reflection rate was measured to be on the order of 90% near the peak wavelength of PMT's sensitivity.

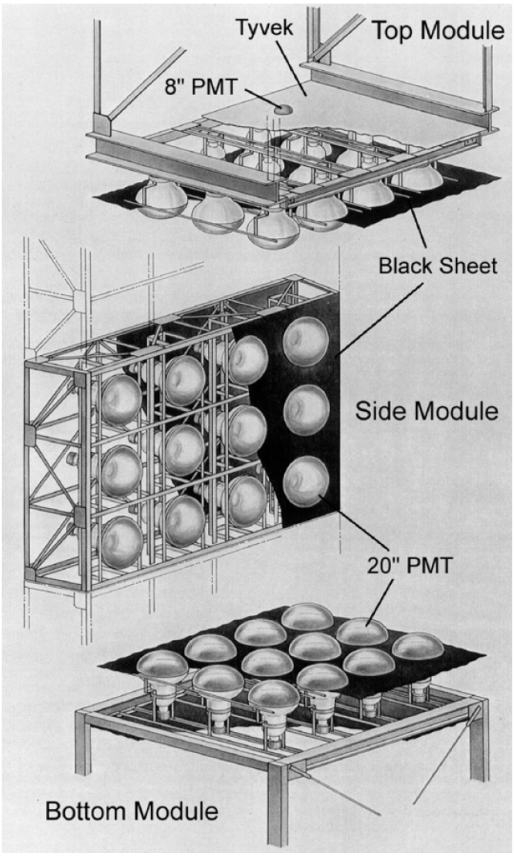

Figure 3.5: Super module of PMTs [12].

3.3.2 The Super-K 50 cm Venetian Blind PMT

A schematic demonstration of the Super-K 50 cm PMT is shown in Figure 3.6 (a). One of the key characters of a PMT is quantum efficiency (QE), which means the probability the photocathode will emit an electron by absorbing an incoming photon. The bialkali (Sb-K-Cs) photocathode used in the Super-K 50 cm PMT was measured to have peak QE of about 21∼22% at 360-400 nm as shown in Figure 3.6 (b).

The phrase "venetian blind" stands for the PMT dynode structure, which is illustrated in Figure 3.7. It was noticed that a venetian blind dynode structure may cause the photoelectron missing the next stage dynode plate and results in the underperformance of a PMT's photon Collection Efficiency (CE). Sophisticated study was done to regularize the electron multiplication process in the Super-K 50 cm PMTs so that its CE was improved by about 50% compared to other venetian PMTs of the similar size [18]. In Super-K, the gain of ID PMTs, i.e. the photon multiplication factor, was set to the order of 10^7 so that they would be sensitive to supernova neutrinos.

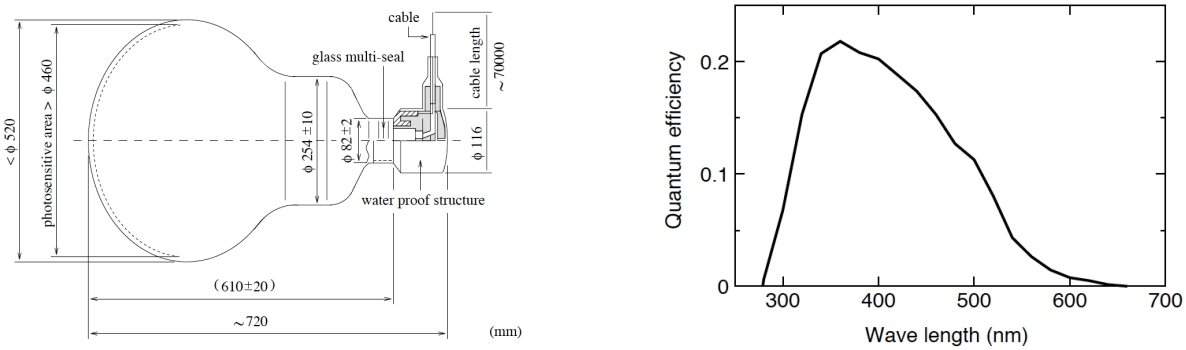

(a) PMT schematic drawing

(b) QE spectrum

Figure 3.6: Super-K 50 cm PMT design and QE spectrum [12].

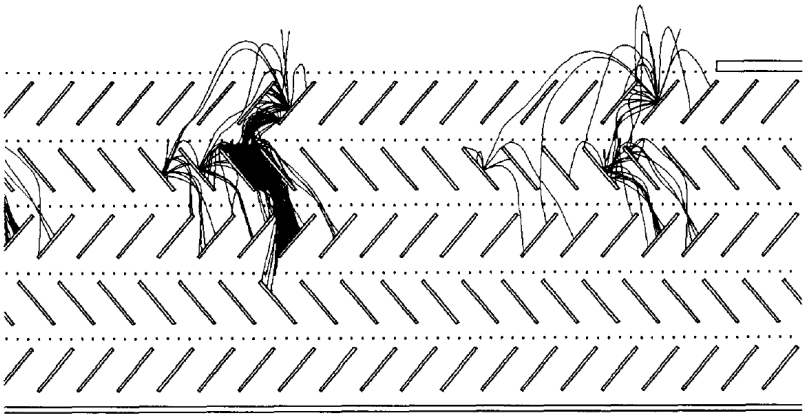

Figure 3.7: Venetian blind dynode display and the Monte Carlo simulation of secondary electron trajectories [18].

3.4 Water

The water quality is essentially critical for the success of Super-K, for an over-abundance of dust in the water will cause too much scattering and absorption of Cherenkov light that decreases the detector sensitivity. Another big contamination in water comes from the dissolved radon gas, which is common for underground facilities and may cause false signal by its radioactivity. Other contaminations include micro creatures and bacterias, as well as heavy particles from the impurity. To remove these contaminations, Super-K adapts both water and air purification systems. The water is circulated in Super-K through series of filters at a rate of 60 tons/hour as shown in Figure 3.8. Meanwhile fresh air from outside is continuously pumped into the tank to reduce the underground radon concentration.

Since the major part of a PMT's dark noise is from its thermal electron emission, it is

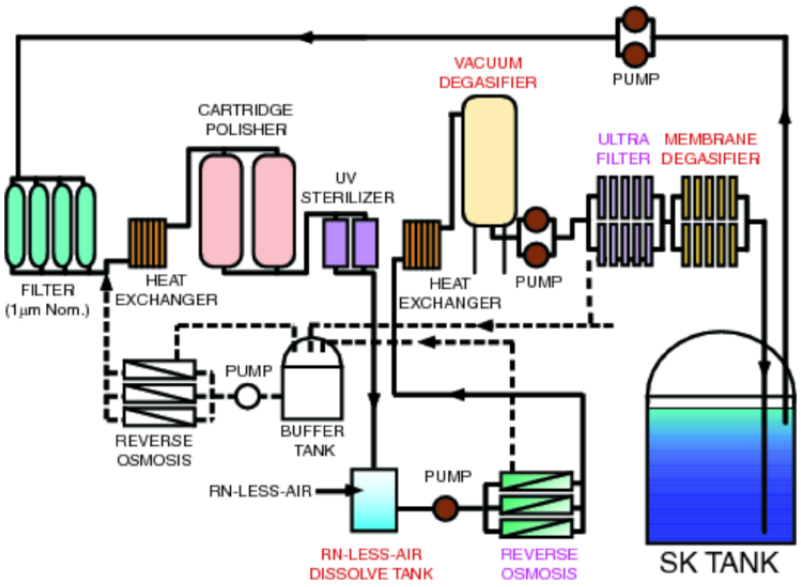

Figure 3.8: The Super-K water purification system [13].

necessary to keep the water temperature low and stable. The heat exchangers in the water purification systems maintain the water temperature at ∼13°C, monitored by the thermometers inside the tank. Meanwhile a full convection is achieved in the bottom ∼10 m, which keeps the temperature uniform in that region. Due to the lack of convection in the higher part of the tank, a 0.2°C top-bottom asymmetry in temperature was observed as shown in Figure 3.9.

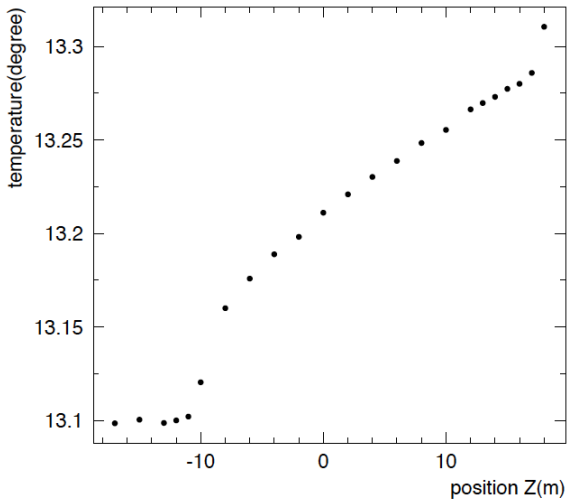

Figure 3.9: Super-K water temperature in vertical direction [19].

Number of inputs	24
Processing speed of QTC	$\sim$ 900 ns/cycle
Number of ranges	3 (small, medium, large)
Discriminator	-0.3 to -14 mV (small range)
Charge dynamic range	0.2 to 2500 pC
Charge resolution	$\sim$0.2 pC (small range)
Charge Linnearity	$<$0.1%
Timing resolution	0.3 ns (2 pC input) $<$ 0.2 ns ($>$ 10 pC input)
Power consumption	$<$ 1 W/ch

Table 3.2: QBEE system specifications [20]

.

3.5 Data Acquisition

At the beginning of SK-IV in 2008, the data acquisition (DAQ) system was updated to QBEE, which can process 100 times more events in a 10 s interval than its predecessor: the ATM system [20]. The specifications of QBEE are listed in Table 3.2. An analog PMT signal is first digitized by the QBEE system to get the hit time and charge information. Meanwhile online PCs continuously collects the "hits" into a software trigger buffer, in which an event trigger will be issued once the total number of PMT hits within 200 ns interval has exceeded a preset threshold. The events accompanied by a trigger are treated as physics data and saved on disk for analyses.

3.6 Prospects for Hyper-K

This section introduces briefly the plan and physics goal of Hyper-K following the description in the 2018 Hyper-K design report [21]. The water tank design of Hyper-K is similar to the Super-K one described in Section 3.3, but much larger—74 m in diameter and 60 m in height. Thus the FC section of real physics analyses in Hyper-K will be 8 times as big as that of Super-K's. As a result Hyper-K is expected to accumulate data much faster, which helps to push forward the neutrino oscillation studies which is currently limited by the lack of statistics. Same with Super-K, Hyper-K will have 40% Photo-Coverage as well.

With the cavern excavation to be started in 2020, Hyper-K is expected to start its first data collection in about a decade from now. It has a great physics potential in neutrino and nucleon decay observation. For neutrino oscillation study, Hyper-K is expected to finalize measuring the mixing angle and Dirac phase mentioned in Section 2.2 and

hence determine the mass hierarchy and CP violation problem. Predictions of Hyper-K's sensitivity to this two quantities are given in Figure 3.10 and Figure 3.11 respectively.

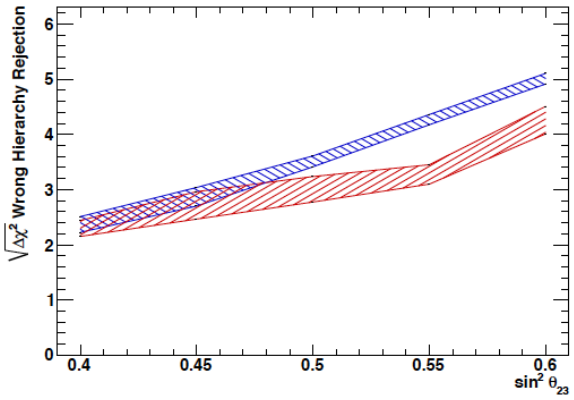

Figure 3.10: Neutrino mass hierarchy sensitivity after as a function of the true value of $\sin^2\theta_{23}$ after10 years of Hyper-K data collection (1.9 Mton·year exposure. The blue (red) band denotes the NH (IH), with the bad width representing the uncertainty from δ_{CP} [21].

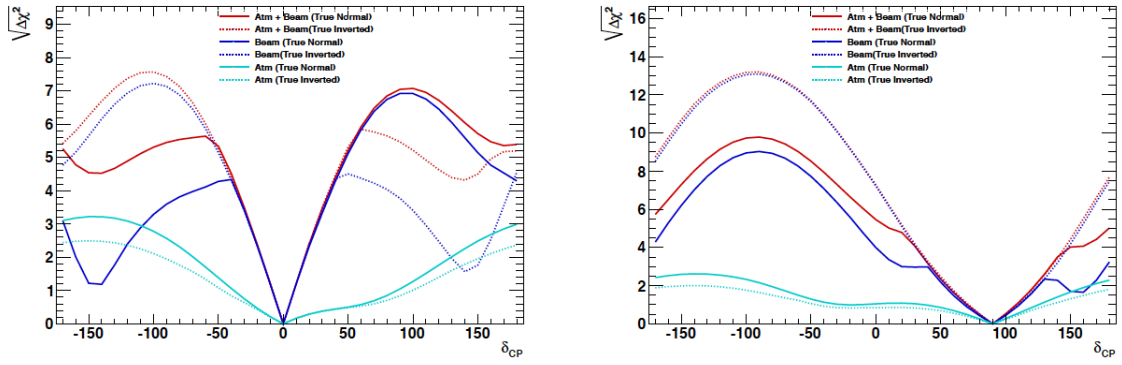

Figure 3.11: Constraints on δ_{CP} after 10-year-long Hyper-K exposure. Different neutrino sources are denoted with different colors. Cyan and blue lines show the constraints from atmospheric neutrino sample and beam neutrino sample individually, The red curve is the combination of the 2. The left (right) figure assumes $\delta_{CP} = 0°$ ($\delta_{CP} = 90°$), with solid (dashed) curves representing NH (IH) [21].

Requirements	Value	Based on	Conditions
Photon detection efficiency	26%	Avg.	QE × CE at wavelength ∼ 400 nm
	(10%)		(including Photo-Coverage on the inner detection area)
Timing Resolution	5.2 ns	FWHM, Avg.	Single Photoelectron (SPE)
Charge resolution	50%	σ, Avg.	SPE
Signal window	200 ns	Max.	Time window covering more than 95% of total integrated charge
Dynamic range	2 photon/cm^2	Min.	Per detection area on wall
Gain	$10^7 \sim 10^8$	Avg.	
Afterpulse rate	5%	Max.	For SPE, relative to the primary pulse
Rate tolerance	10 MHz	Min.	SPE pulse, within 10% change of gain
Magnetic field tolerance	100 mG	Min.	Within 10% degradation
Life time	20 years	Min.	Less than 10% dead rate
Pressure rating	0.8 MPa	Min.	Static, load in water

Table 4.1: Minimum requirements of the Hyper-K ID PMTs from [21].

4 The Hyper-K 50 cm Box&Line PMT

Among the many upgrades of Hyper-K from Super-K, the ID PMT is one of those most important. Aiming to finally solve the mass hierarchy and CP violation problem that has been challenging physicists for decades, Hyper-K is in need of an advanced PMT that is competent for the demanding nature of precise neutrino oscillation observation. The minimum requirements for Hyper-K's photosensors are listed in Table 4.1, There are many candidates, and the Hamamatsu R12860 50 cm Box&Line (B&L) PMT (Figure 4.1) is one of them. This chapter demonstrates some of its key characteristics, most of which can also be found in the ref. [21].

4.1 The Box&Line Dynodes

The Box&Line stands for the specific dynode arrangement of this PMT as shown in Figure 4.2. The first dynode plate, which is larger than any others, is called the "Box"

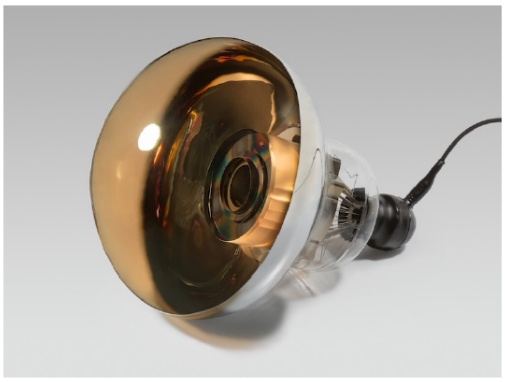

Figure 4.1: Hamamatsu R12600 50 cm B&L PMT

and is known for large photon coverage. Meanwhile the series of small plates is called the "line" and helps to improve PMT's linearity.

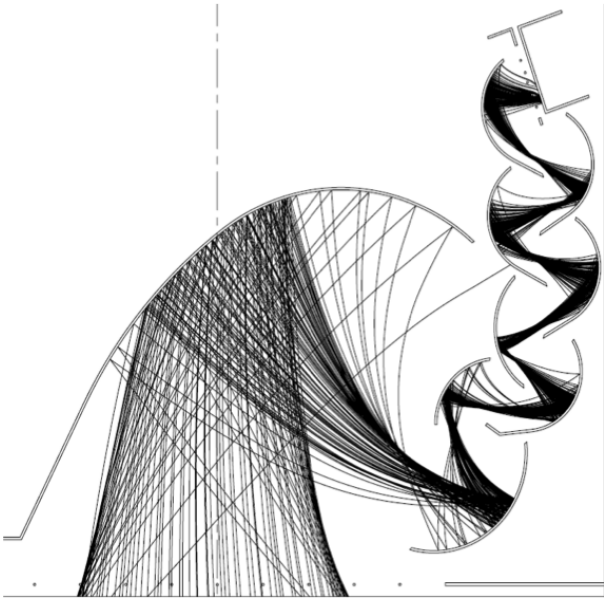

Figure 4.2: Box&Line dynode layout with electron trajectories. Electrons enter from the bottom at where the photocathode locates [21].

4.2 High Photon Detection Efficiency

The profoundest improvement of the B&L PMTs compared to the Super-K Venetian blind ones is its superior photon detection efficiency, which is QE $\times$ CE in Table 4.1. Figure 4.3 compares the QE between the Hyper-K B&L and Super-K Venetian blind PMTs. At the peak wavelength of $\sim$390 nm, the former has a typical QE of 30% whereas the latter has only 21$\sim$22% as aforementioned in Section 3.3.2.

Although great efforts were made to improve the Super-K Venetian blind PMT's CE by

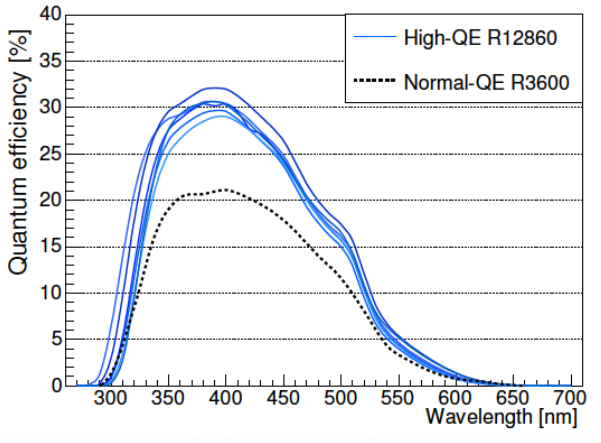

Figure 4.3: Measured QE of six 50cm B&L PMTs (solid lines) and Super-K Venetian Blind PMTs (dashed lines) [21].

large, it still remained at 73% within the 46 cm cross section of the photocathode. In comparison, the Hyper-K B&L PMT has 95% CE in the same area and as high as 87% within the full size of 50 cm. It was achieved by the new B&L dynode structure as well as the optimized glass curvature and focusing electrode. At SPE level, the CE of B&L PMT was measured to be 1.4 times that of the Venetian blind PMT's, and hence resulted in an improvement in QE×CE by a factor of 1.9.

4.3 Charge and Time Responses

Thanks to the large photon coverage of the "Box" dynode, the SPE hit rate has increased in a B&L PMT largely and therefore improved the SPE charge resolution, which is defined by the ratio of SPE pulse width in σ to its peak position. The B&L PMT's SPE charge resolution was measured to be 30.8% and the Venetian blind 60.1% as shown in Figure 4.4(a). On the other hand, the rise time of SPE pulse in a B&L PMT is ∼40% faster than the Venetian blind PMT, meanwhile the former's Transit Time Spread (TTS) caused by different electron traveling time was measured to be 1.23 ns in σ, which is over 50% better than latter's at 2.86 ns (Figure 4.4(b). The aforementioned comparison results of SPE charge resolution and TTS are based on a measurement done in the Super-K site with 145 B&L PMTs and 6 Venetian blinds, at a gain of 1.4×10^7 [22].

4.4 Gain Stability

The PMT's charge response range is crucial for observing a wide energy range of particles. It is possible that a large number of photons hitting the PMT simultaneously may fully dissipate the available electrons in the photocathode and cause saturation in the PMT

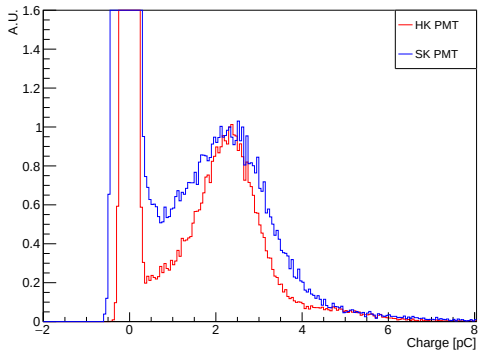

(a) SPE charge resolution in σ

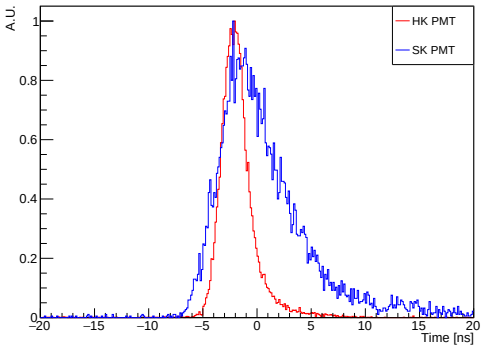

(b) SPE time resolution in σ

Figure 4.4: Hyper-K B&L PMT charge and time resolution, with blue (red) curves denoting the Super-K (Hyper-K) PMT.

output, i.e. charge no longer increases with light intensity. To confirm that the B&L PMT is suitable for the physics tasks of Hyper-K, a measurement on charge linearity was done and verified that the B&L PMT's charge output is in 95% agreement with expected value up to a signal of 470 photo-electrons (PEs) as shown in Figure 4.5. Moreover, the saturation level was measured to be more than 1,000 PEs. Therefore for the signal lower than 1,000 PEs the charge output will be reliable with the correction from the non-linear effect derived from Figure 4.5.

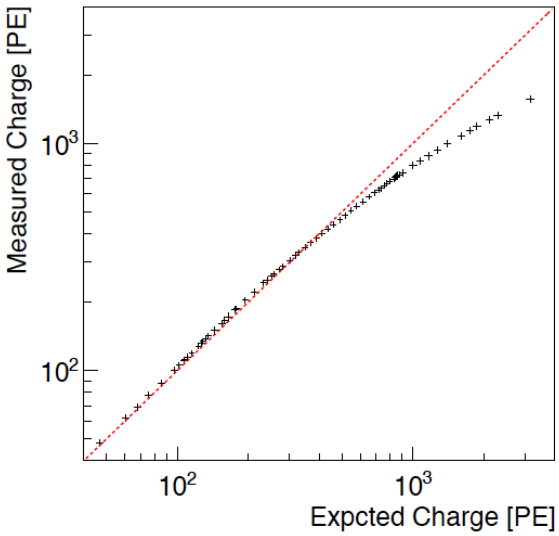

Figure 4.5: Measured charge output linearity of B&L PMT. The red dotted line represents the perfect linear case [21].

Since these PMTs are designed for over 20 years of life span, it is also important to make

sure that the PMT's performance does not degrade too much with aging. To confirm this, the gain of 3 B&L PMT samples was monitored over 2 years in a 200 ton water tank in the Super-K site, which was originally constructed for the feasibility study of Gd dissolved water. The result turned out to be good, with negligible change and only 1% (at RMS) fluctuation in all 3 tubes. A 2-month window snapshot of this monitoring is shown in Figure 4.6.

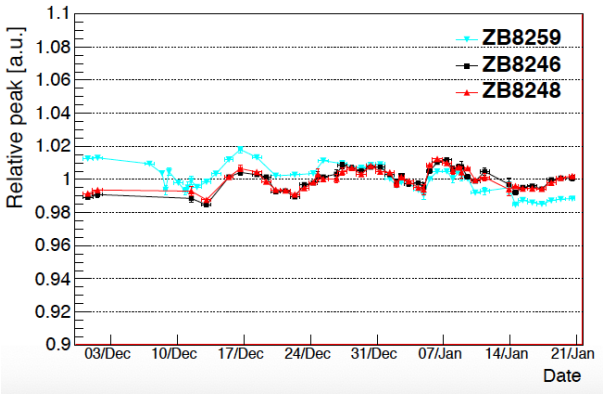

Figure 4.6: The relative charge output of 3 B&L PMTs over 2 months operation. The 3 tubes were monitored inside a 200 tons water tank with a Xenon light source [21].

4.5 Background Noises

There are 2 major sources of background noises that may affect the physics observation. One is the dark hit from the PMT itself through electron thermal emissions at the photocathode. The dark hit may cause fake signals if they happen to be over the signal selection threshold after being integrated. Since the dark hit pulse is usually small in energy, it will affect the most the low energy observation, for example supernova and solar neutrinos. The dark hit rate is sensitive to many factors including the material's working function, the environmental temperature, the voltage applied to the PMT, the time for stabilization with minimum light exposure, etc. For the Hyper-K B&L PMTs, the dark hit rate (8.3 kHz in 15°C water after 1 month stabilization) is higher than the Super-K Venetian blind ones (4.2 kHz) as a side-effect of its higher QE.

It has been noticed that a substantial portion of the dark hit in a B&L PMT is not the usual "singularly-pulsed" electron thermal emission, but some bursting pulses as shown in Figure 4.7. The source of such a feature, suspected to be the radioactive isotopes in the PMT glass, is under investigation. A solution to avoid the false triggering from the bursting dark pulses has already been worked out by [23], meanwhile currently large efforts are being made to suppress such kind of bursting dark hits in the B&L PMTs.

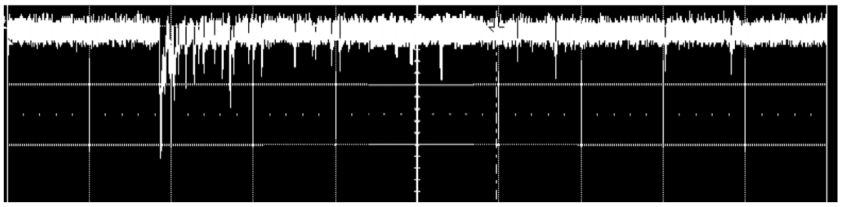

(a) The waveform of bursting dark hits from ref. [23]

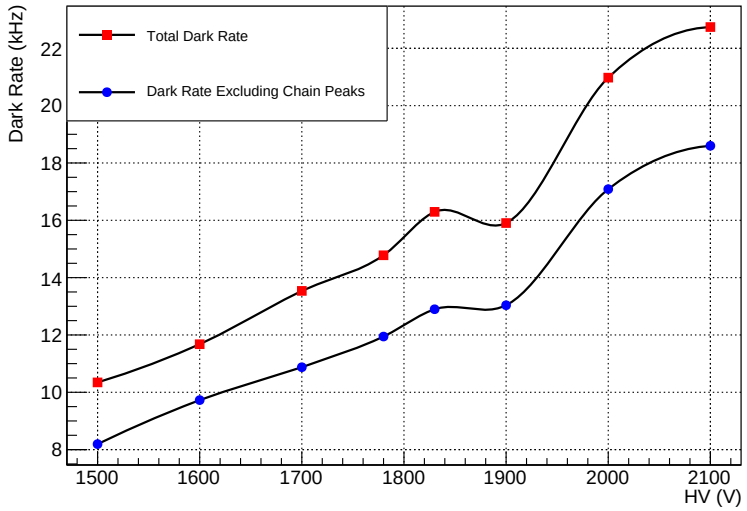

(b) The rates of all dark hits and bursting pulses excluded ones

Figure 4.7: The dark hits of Hyper-K B&L PMT's. In panel (a) is a 1 μs snapshot from oscilloscope showing the typical waveform of the bursting pulses. Panel (b) shows the scanned total dark hit rate and the rate (red) after excluding the bursting pulses (blue) at room temperature after 1 day of stabilization. The x-axis shows the corresponding high voltage (HV) of each measurement.

Another noise source is the PMT afterpulse, which is caused by the ionized residual gases drifting to the photocathode and releasing electrons not related to the incoming photons. Different gas elements will have different delay in time, ranging from tens of ns to several μs. A large afterpulse rate in PMT can result in mis-reconstruction for delayed interactions. The afterpulse rate of the Hyper-K B&L PMTs' was measured to be less than 5% relative to the main pulse at SPE, which is comparable to the Super-K tubes.

5 2018 Detector Upgrade

As mentioned in Chapter 1, Super-K has completed the 2018 detector upgrade by January 2019. A variety of refurbishments have been finished, including a new water cycling system for Gd parallel to the current one as shown in Section 3.4. To make sure that NO Gd from the experiment will leak outside, better leakage proof has been achieved and checked carefully.

Besides the upgrade of water system, there were 136 dead ID channels replaced by the new Hyper-K 50 cm B&L PMTs. After January 2019, a complete calibration for the upgraded Super-K tank started. This work focuses on the refurbishments and calibration tasks related to the ID PMTs, which include both the Super-K and Hyper-K 50 cm PMTs.

5.1 Pre-Calibration of Hyper-K 50 cm B&L PMTs

Before the installation, the Hyper-K 50 cm B&L PMTs have gone through a series of quality checks in the Super-K site with a newly constructed experiment. This section will describe the measurements and results of those new tubes in details. Meanwhile a brief summary can be also found in [24].

5.1.1 Experiment Setting up

In March 2018, 145 newly produced Hyper-K 50 cm B&L PMTs arrived at the Super-K site. An experiment to measure those tubes was set up in an underground laboratory at about 100 m away from the Super-K tank. A dark room large enough for 7 PMTs was constructed using PVC frames and light proof black curtains. The PMTs were placed on the specially designed carts so that all the first dynodes were held facing up at around 60 cm above the floor. Figure 5.1 shows a schematic top-view of the dark room and PMTs in carts denoted as 7 channels.

To mitigate the geo-magnetic field that distorts the photoelectrons inside the PMTs and thus causes systematic uncertainties, 6 Helmholtz coils were divided into 3 pairs surrounding the whole dark room in the x, y, and z directions denoted in Figure 5.1. Furthermore, all the PMTs in the dark room are aligned in the same direction—with the first dynode plate "Box" in +y direction and the second "Line" in the -y. However, the magnetic field inside the dark room was not uniform and large variation by positions was observed. Therefore it was not possible to bring the field distribution inside the dark room to uniform in all 3 spatial directions with the coils being used. Since the PMTs

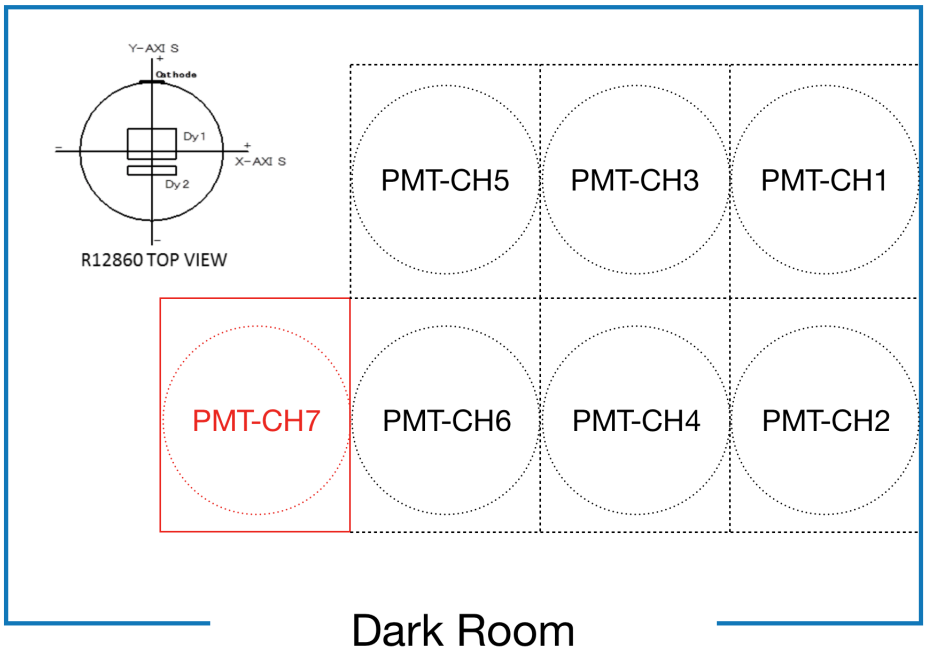

Figure 5.1: Schematic view of the dark room. The entrance is from the bottom in the figure.

were facing upward and thus the photoelectron would propagate in the z direction, most constraints were then applied to the x and y directions in which the magnetic field has the biggest effect on the experiment. Figure 5.2 shows the residual magnetic field at the 7 PMT positions after the correction, with fluctuation less than ±100 mG in the x and y directions. The currents and voltages applied in each pair of coils are shown in Table 5.1.

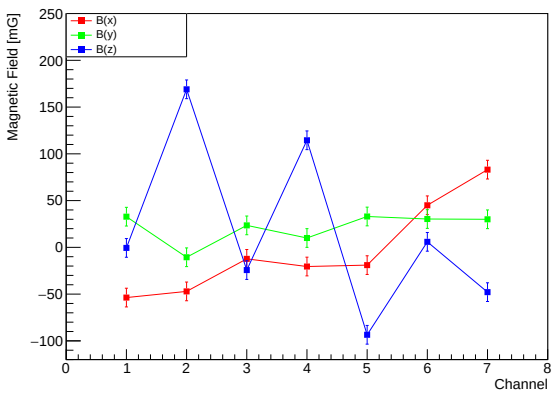

Figure 5.2: Residual magnetic field after correction at the 7 PMT positions.

During the experiment 7 PMTs were measured simultaneously. The correspondence be-

I_x (A)	I_y (A)	I_z (A)
8.49	17.26	4.49
V_x (V)	V_y (V)	V_z (V)
16.10	20.78	9.86

Table 5.1: Currents and voltages applied to each pair of Helmholtz coils in all 3 spatial directions.

tween the channel number in the electronic DAQ system and the PMT positions is shown in Figure 5.1. A NIM Analog-to-Digital Converter (ADC) module was used to record the amplified charge information of the PMTs', meanwhile a Time-to-Digital Converter (TDC) module for timing. At the same time a scaler was used to count the dark hits of each PMT. At the 7 PMT positions, a laser light source was hanging from the ceiling in the dark room at about 50∼60 cm above the PMT glass dome. The laser was set with a 150 mA amplitude and 150 ps width, so the occupancy in each PMT was as low as 0.09 photoelectron/hit and generated almost only SPE signals. A NIM clock was attached to trigger both the laser and DAQ system. A schematic plot of the electronic circuit of the pre-calibration is shown in Figure 5.3.

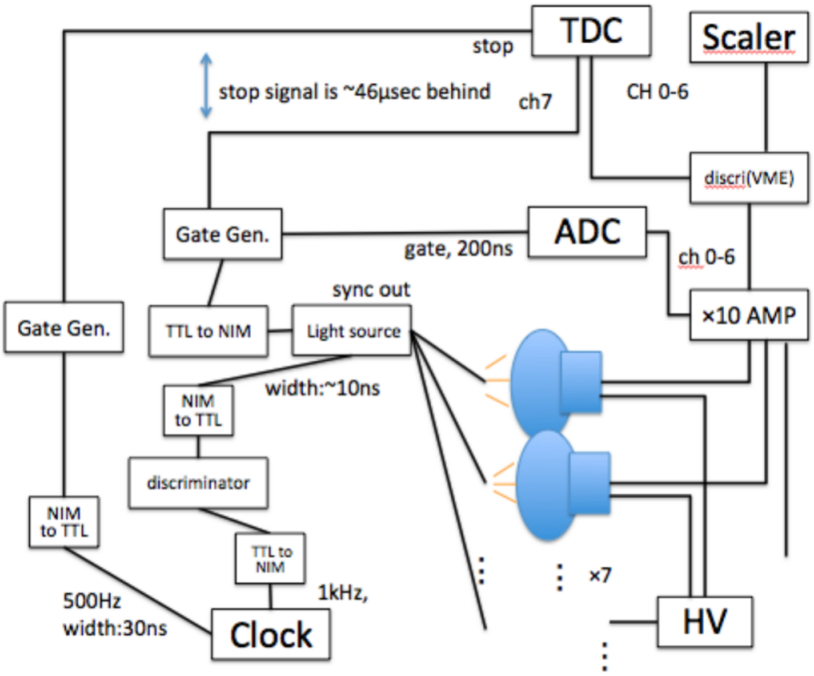

Figure 5.3: Schematic plot of the electronic circuit.

5.1.2 Data Collection

The data collection was done on a daily base by shifts. Everyday in the morning 6 PMTs in the dark room measured on the previous day will be replaced. One PMT was fixed throughout the whole experiment period at channel 7 as marked out in red in Figure 5.1. This reference PMT was used to determine whether if there is any systematic difference between the beginning and end. After 1∼2 hours of stabilization in the dark room with voltage on, the first data would be taken by the shift members. Two voltage settings were tested. One was the value given by the Hamamatsu producer that corresponds to 10^7 gain. The other was the tuned voltage corresponds to 1.4×10^7 gain calculated by the voltage scan conducted during this experiment. For simplicity, the lower voltage at 10^7 gain is called "HK Voltage" in this work, and the higher voltage at 1.4×10^7 is called "SK voltage". Besides the voltage scan, the dark hit rate at different discriminator thresholds was also scanned. Then during the midnight after ∼10 hours of stabilization, the system was designed to automatically take another set of data for comparison. This process was repeated for all 145 Hypre-K PMTs and 6 Super-K ones that were temproarily taken out of the tank during the detector upgrade period. Since those 6 Super-K PMTs would be soon re-installed inside the tank, the FRP covers were kept attached to the PMTs for protection and contamination proof.

The function used to fit the SPE charge distribution was

$$f(x) = \underbrace{p_0 \cdot e^{-\left(\frac{x-p_1}{\sqrt{2}p_2}\right)^2}}_{\text{SPE Gaussian peak}} + \underbrace{0.5 \cdot p_3 \cdot \left(\text{erf}\Big(\frac{x-p_4}{p_5}\Big) - \text{erf}\Big(\frac{x-p_1}{p_2}\Big)\right)}_{\text{Back scattering}} \tag{5.1}$$

where the SPE Gaussian peak and back scattering are represented by the green and cyan curves in Figure 5.4(a) respectively.

On the other hand the equation for timing distribution was

$$f(x) = 0.5 \cdot \lambda \cdot \gamma \cdot e^{0.5 \cdot \lambda \cdot \left(2 \cdot \mu + \lambda \cdot \sigma^2 - 2x\right)} \cdot \left(1 - \text{erf}\Big(\frac{\mu + \lambda \cdot \sigma^2 - x}{\sqrt{2}\sigma}\Big)\right) \tag{5.2}$$

which represents the red dashed curve in Figure 5.4(b).

5.1.3 Systematic Error Corrections

As mentioned in Section 5.1.1, large variation existed in the residual magnetic field among the 7 PMT positions. Meanwhile there were also other uncertainties from the electronics such as the variation of amplification factor at different channels, the different noise

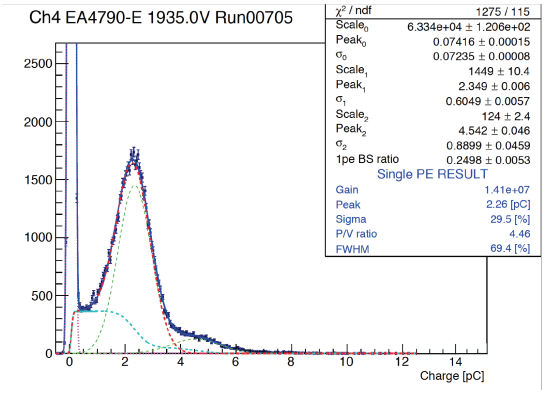

(a) SPE charge distribution with fitting curves

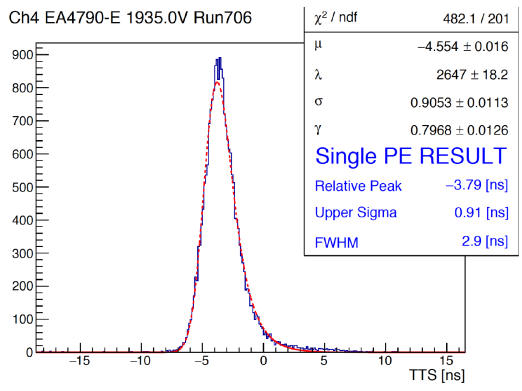

(b) SPE timing distribution with fitting curves

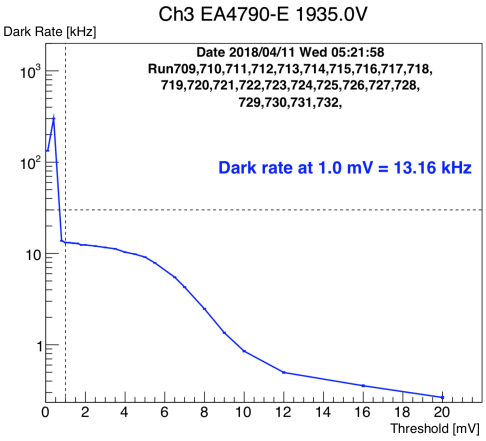

(c) SPE dark hit rate scan

Figure 5.4: Hyper-K 50 cm B&L data samples

levels in TDC channels, etc. that might bias the experimental results. Therefore it was necessary to reduce the systematic errors that arouse from different PMT positions and channels.

This was accomplished by measuring the reference PMT at all other 6 positions and the corresponding channels. The voltage was set to "HK voltage". Figure 5.5 shows the measurement of the gain, TTS, SPE resolution, single photoelectron hit rate (SHR), dark hit rate, and peak-to-valley ratio (PVR) at 7 channels with the reference PMT. The SHR was calculated by the ratio of SPE hits to the integrated hits of SPE + pedestal, meanwhile the PVR was defined as the ratio of SPE peak height to he lowest point between the SPE and pedestal. Multiple measurements were taken at the same position for an estimation of statistical uncertainties. For the charge related quantities like the gain and SHR, a correction by scaling among the 7 channels was applied since it was the amplification factor considered as the major error source. Whereas for TTS a simple offset was added to each channel to correct the different background noise level. For

quantities such as SPE resolution and PVR, no correction was applied since by taking the ratio it was assumed that the error could be cancelled out. Last but not the least, no correction was applied to the dark hit rate either because it is mostly affected by other factors as mentioned in Section 4.5 and in principle should not depend on PMT position or channel.

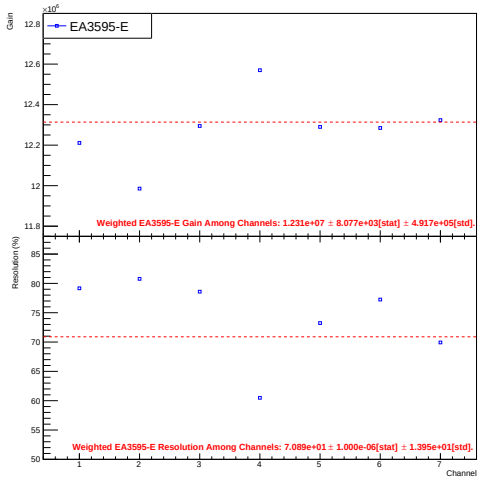

(a) Gain (top) and SPE resolution (bottom)

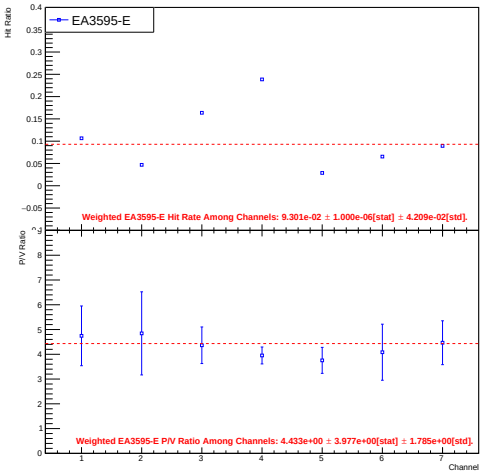

(b) SHR (top) and PVR (bottom)

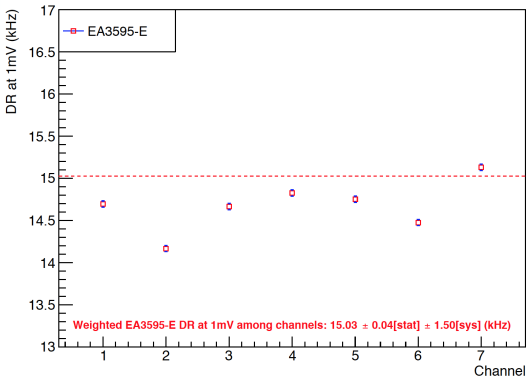

(c) Dark hit rate at 1mV threshold

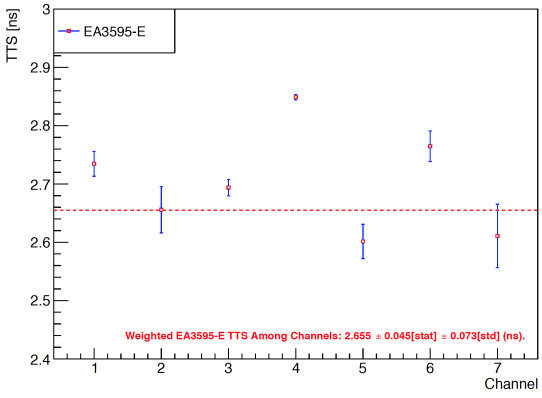

(d) TTS

Figure 5.5: Channel variation measured by the reference PMT. The weighted mean is shown by red dashed line in each panel.

Some big source of uncertainty other than the channel difference is the ADC pedestal fluctuation. The pedestal kept changing over time in all 7 PMT and would cause large uncertainties if not subtracted correctly. This fluctuation is purely caused by uncertainties in the electronics and not related to the photon multiplication process in PMTs, but will affect determining the SPE peak. Figure 5.6 shows the pedestal fluctuation over the whole experiment period, which was about 1 month.

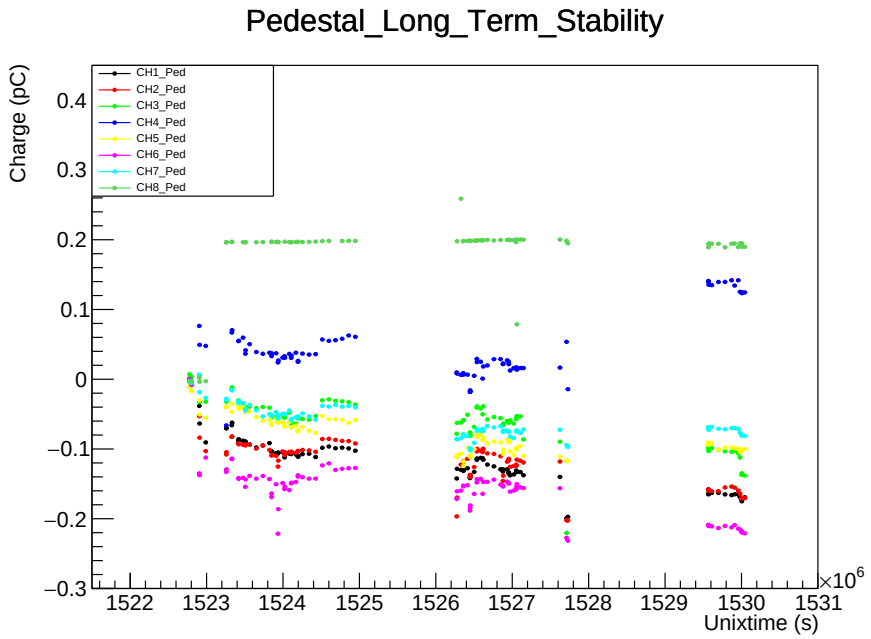

Figure 5.6: Pedestal fluctuation over time with the empty channel 8 (no fluctuation) as a reference.

Since even at the same voltage, a PMT's gain is sensitive to many other factors including environment temperature, stabilization status, etc, it was also necessary to confirm that the gain was stable in this experiment. From the reference PMT, both the long term and day-and-night gain stability were checked. The room temperature was monitored to be stable around 25°C and hence no clear difference was seen in the gain from the daytime and late-night measurements. On the other hand, throughout the 1-month experiment period there appears to be a 0.8% difference in the gain of reference PMT, but it was much smaller than the day-by-day fluctuation and not so convincing for unstable gain as shown in Figure 5.7(a).

The fitting function for long term gain stability check was

$$f(x) = \frac{N}{t - t_{offset}} + A \tag{5.3}$$

A stronger time dependence can be seen in the bottom panel of Figure 5.7(a), which shows the SPE peak position before the pedestal subtraction. The trend resembles what is shown in Figure 5.6 a lot. The gain in the top panel was calculated after subtracting the pedestal from the SPE peak position, and has merely no time dependence. Meanwhile for the day-and-night difference in gain was as small as 0.5%. Therefore, the gain was verified to be stable over both long and short terms by the reference PMT.

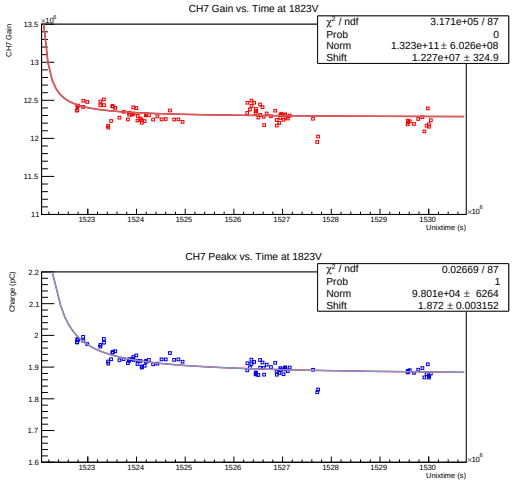

(a) Long term gain stability (top) and SPE peak (bottom) without pedestal subtraction

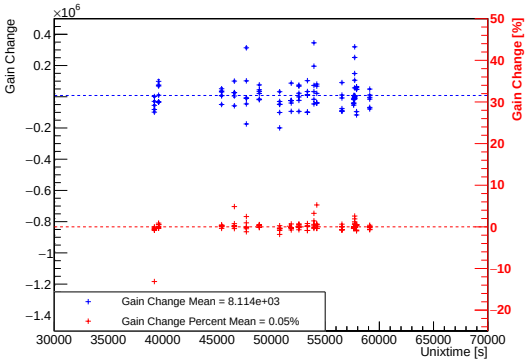

(b) Day-and-night gain difference

Figure 5.7: Gain stability check with the reference PMT.

5.1.4 Measurements

One of the motivations of this experiment was to verify that these Hyper-K 50 cm B&L PMTs were qualified to be installed inside the Super-K tank. According to the operation and detection requirements of Super-K, 4 criteria was made based on the voltage range for the target gain, the TTS that represents timing resolution, the dark hit rate, and the SPE resolution.

In this experiment, we set the target gain to 1.4×10^7. The corresponding "SK Voltage" were found by the voltage scan at 12 points ranging from 1500 V to 2250V. At each voltage, the PMT's SPE peak was recorded and used to fit the peak-voltage relation represented by the function

$$\mu(V) = \alpha \cdot (V - V_{off})^{\beta} \tag{5.4}$$

where μ(V) stands for the corresponding gain at voltage V. An example of Eq 5.4 is shown in Figure 5.8(a). The voltage of all 145 Hyper-K 50 cm PMTs at the "SK Voltage" is shown in Figure 5.8. The results of "HK Voltage" in this experiment were slightly different from the values by the PMT producer. This was because of the different fitting function Eq 5.1 we used, in which the back scattering part will affect the SPE peak position.

Other than these 4 quality checks, a few measurements on different quantities were also made. But the result was not representative and limited by either the hardware or analysis method so that they could not serve for quality checks. For example, the afterpulse

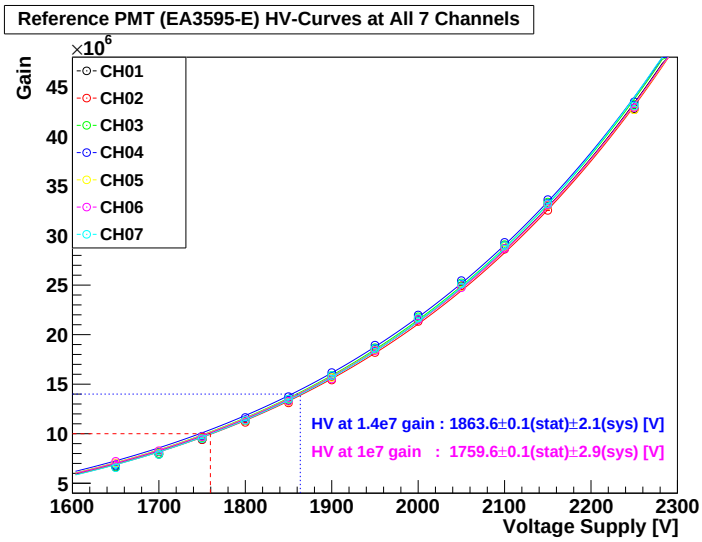

Figure 5.8: Pre-calibration voltage scan example by the reference PMT.

rate was measured in this experiment and turned out to be less than 1%. However, due to the low intensity light source being used, it was unclear whether this low rate is a result of the lack of ionization or residual gas. Moreover, Figure 5.9 shows that with the reference PMT, a 5% afterpulse rate would be observed in some channels whereas 0 in some others such that a channel-by-channel correction was not possible. Given to these reasons, we decided not to include the afterpulse rate as a checking criterion.

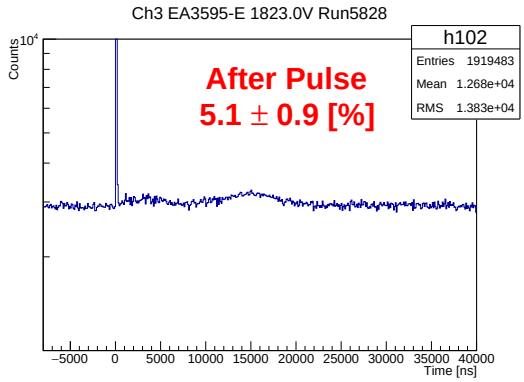

(a) Reference PMT afterpulse at channel 3

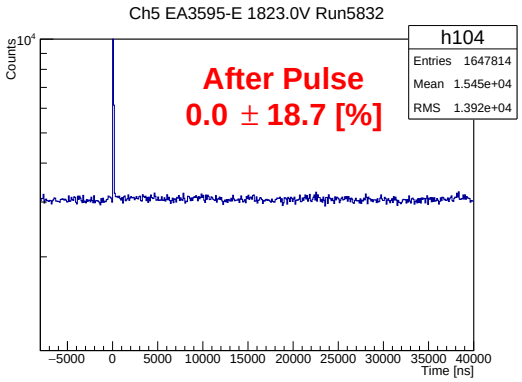

(b) Reference PMT afterpulse at channel 5

Figure 5.9: The afterpulse rate of reference PMT's at different channels.

The other quantity excluded was the PVR. During the analysis we have found that in some PMTs the data points were scattered in the SPE "valley". A larger disagreement between the data and fitting was found compared to the other regions in the charge distribution. More specifically, in such a scattered case the fitting tends to find the lowest point that turned out to be an outlier. This discrepancy between the fitted PVR and

the PVR from the data average is shown in Figure 5.10 where a large portion of PMTs have inconsistent results. Therefore a different PVR in this experiment does not directly mean the PMT's SPE peak is different. Hence the criterion provided by the producer could not be applied.

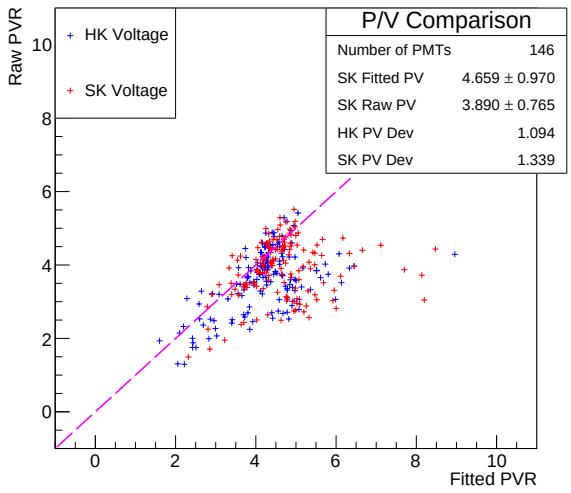

Figure 5.10: The comparison of the fitted and raw data PVR at "HK voltage" and "SK voltage". The entry number is larger by 1 because a PMT was accidentally measured twice.

At last, the selection was then made only based on the aforementioned 4 quantities. The selection range for voltage was determined to be 1500∼2350V, for TTS to be 1∼4 ns in FWHM, for SPE resolution to be 20%∼70% as measured by σ of the peak, and the range for dark hit rate to be 2∼30 kHz. The measured value of these quantities from all 145 PMTs are shown respectively in Figure 5.11, where the selection range is plotted in dotted vertical lines in each panel. All 145 PMTs have satisfied those selections and in the end 136 were randomly picked to be installed in Super-K.

Please note that the allowed range for dark hit rate was significantly large (30 kHz compared to 4.2 kHz in Super-K), but had been used before in the Hyper-K PMT gain stability check that was mentioned in Section 4.4. This was because during the experiment we kept exchanging the PMTs and the stabilization time was only several hours. In addition the room temperature was more than 10°C higher than the Super-K water temperature. The dark hit rate selection made in this experiment does not aim to determine the dark noise level of these Hyper-K PMTs, but just as a quick check for broken or flasher tubes if any.

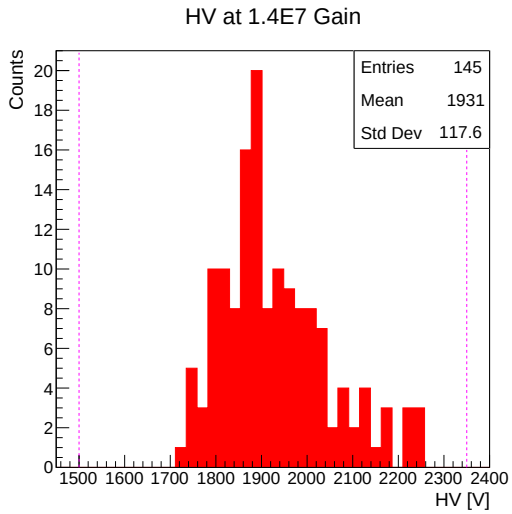

(a) Voltages at 1.4×10^7 gain

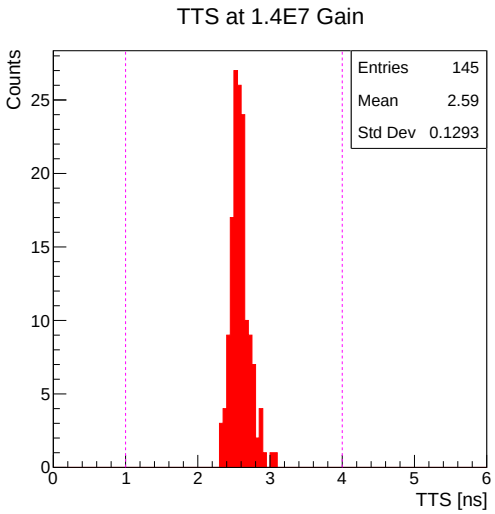

(b) TTS at 1.4×10^7 gain

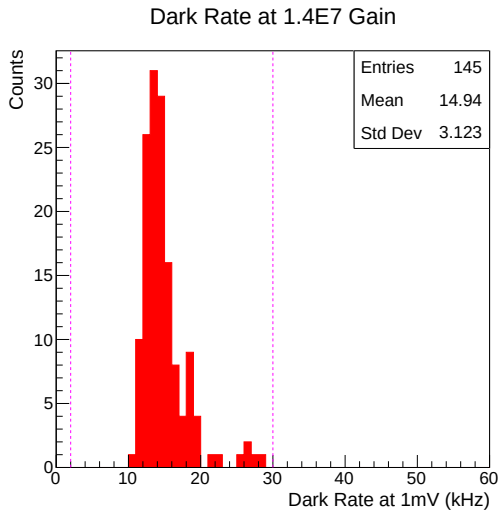

(c) Dark hit rate (1mV threshold) at 1.4×10^7 gain

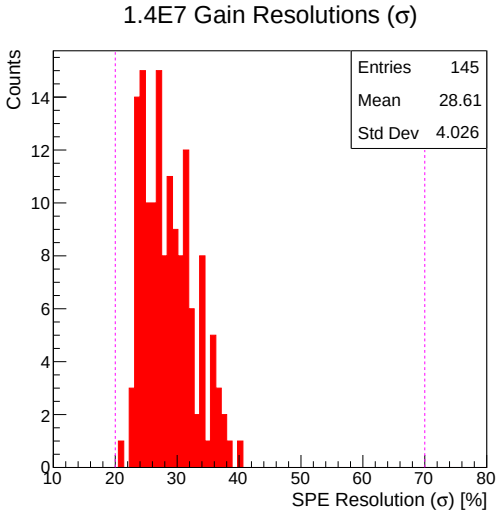

(d) SPE resolution at 1.4×10^7 gain

Figure 5.11: Measurement and selection of 145 Hyper-K 50 cm PMTs.

5.2 Voltage Adjustment

With 136 ID channels in Super-K replaced by the Hyper-K 50 cm B&L PMT, new voltage settings were needed since these PMTs have different charge responses. Meanwhile, it was observed that the ID gain kept drifting during the SK-IV phase. It had been a big concern for a long time since the gain drift would cause larger channel-by-channel variation in charge responses, and hence extra systematic uncertainty in physics analyses. Taking the chance of 2018 detector upgrade and ID PMT replacement, we decided to retune the voltage for all ID PMT channels. This chapter will explain the voltage adjustment with the experimental method, adjustment results, and underlying systematic uncertainties in details.

5.2.1 Data Collection

Previously in Super-K, the voltage of each ID channel was determined using a Xenon source, which emits large intensity of isotropic light triggering multi-PE signals in the PMTs. There were 420 Super-K 50 cm PMTs precisely calibrated outside and evenly distributed in the tank [19]. Those PMTs severed as a reference of the expected charge response for the PMTs at the same distances to the Xenon source. A relation between the number of hits in each PMT and the applied voltage was found to determine the voltage for the target gain.

However, this time there was no such a group of "reference PMT" anymore. Those 420 PMTs' gain has changed along with all the others throughout the SK-IV phase and thus can no longer be used as a guidance. Moreover, the old hanging system for Xenon source was broken and no substitution was available. Therefore we had to find a new method to tune the ID voltages. Meanwhile, there was also another request to investigate the Super-K detector's energy lower limit threshold cut. Hence a weaker light source other than the Xenon is preferred. Taking all of these into account, this time we used a laser diode Hamamatsu PLP-10 that has low intensity and peak wavelength at 404 nm. Since this source was at first used for supernova study, it is also called SN-LD. On the other hand, since both the number of hits and mean value of charge distribution are sensitive to the energy threshold cut, we used the fitted SPE peak as the reference for a PMT's gain similar to the pre-calibration mentioned in Section 5.1. More details about the SPE peak fitting will be discussed in Section 5.2.2.

Figure 5.12 shows a schematic view of the experimental set up for voltage adjustment in the Super-K tank. The SN-LD light was injected into the tank through a diffuser ball

x (cm)	y (cm)	z (cm)
35.35	-70.70	0.00

Table 5.2: The coordinates of the diffuser ball in the tank.

near the center. The coordinates are given in Table 5.2. A NIM clock was used to trigger the SN-LD and the DAQ. The coincidence with the SN-LD signal in channel 15024 was required for triggering the DAQ. Since the LD pulse rate was tuned to 2 kHz, an extra cut was applied to the data selection that any 2 consecutive signals should be separated by ∼0.5 ms. This was to remove the potential false DAQ triggering by other sources. The time window for DAQ was at -400 to 0 ns from the trigger. Moreover, a piece of background (-800 to -400 ns) taken outside of the trigger time window in each PMT was subtracted from the "on-time" signal to reduce the dark noise. On February 7th, 2019 7 sets of data were taken with the SN-LD at different voltages for each PMT as shown in Table 5.3.

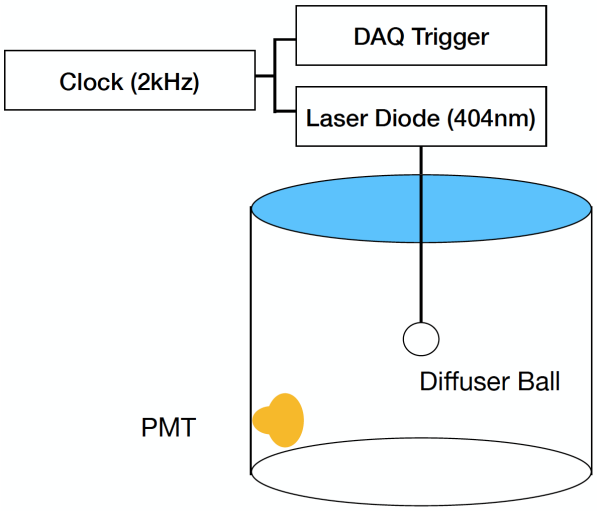

Figure 5.12: Schematic view of voltage adjustment experimental set up.

5.2.2 New Voltage Determination

To find the new voltage for each PMT, a similar method to the pre-calibration of Hyper-K 50 cm PMTs as mentioned in Section 5.1 was used. From the 7 sets of data taken at voltages ranging -75 V to +75 V from the SK-IV value, a relation between a PMT's SPE peak and its gain was found. To extract the charge information from the ADC counts at each channel, a polynomial function representing count-to-charge conversion was applied in the data reduction process of Super-K. Depending on the target charge range, it would either be a linear or higher order function. In addition to that, the temperature effect

Run#	Duration (s)	Voltage
80249	1393	0
80254	994	+75 V
80263	1221	+50 V
80265	1291	+25 V
80269	1087	0
80275	1349	-25 V
80278	1075	-50 V
80282	1082	-75 V

Table 5.3: Run information of the SN-LD data. The 3rd column shows the voltage difference of each PMT from the SK-IV setting.

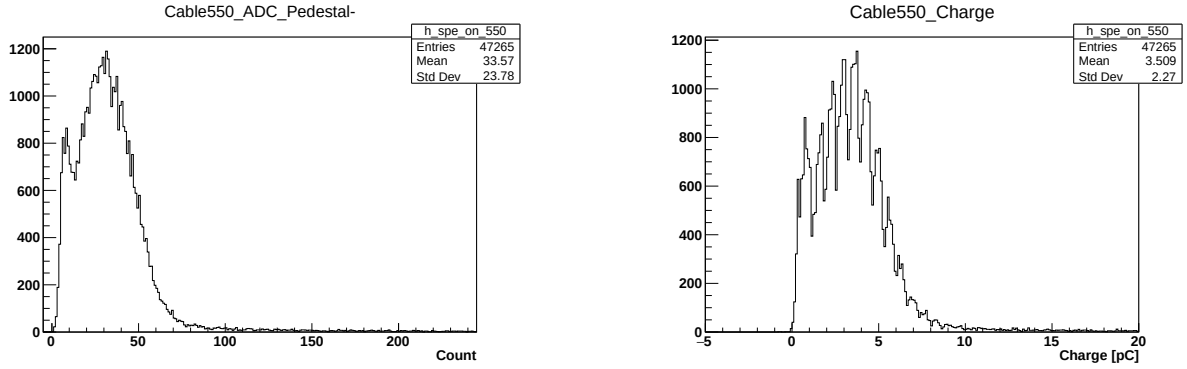

(a) Temperature corrected ADC count distribution (after pedestal subtraction)

(b) Converted SPE charge distribution

Figure 5.13: The spiky feature of SPE charge distribution that comes from the count-to-charge conversion.

of QBEE signal read out was also corrected. However, it was noticed that the resulted charge distribution had some spiky feature as shown in Figure 5.13. The cause of this was considered to be the rounding and binning issue when converting from integer ADC counts to decimals. For each channel 1 ADC count corresponds to some long digits decimal number of charges, i.e. some number like 0.113xxxxxxx... Figure 5.14 shows that by simply changing the bin width from 0.1 to 0.11 pC, such a spiky feature would to some extents disappear. Although the actual count-to-charge correspondence is different for each channel, the 0.11 pC bin width was the leading term in decimals for all channels and thus helped to solve the issue. Then the spikes were further reduced by rebinning the histograms.

Since the Super-K and Hyper-K PMTs have different SPE charge response, the fitting

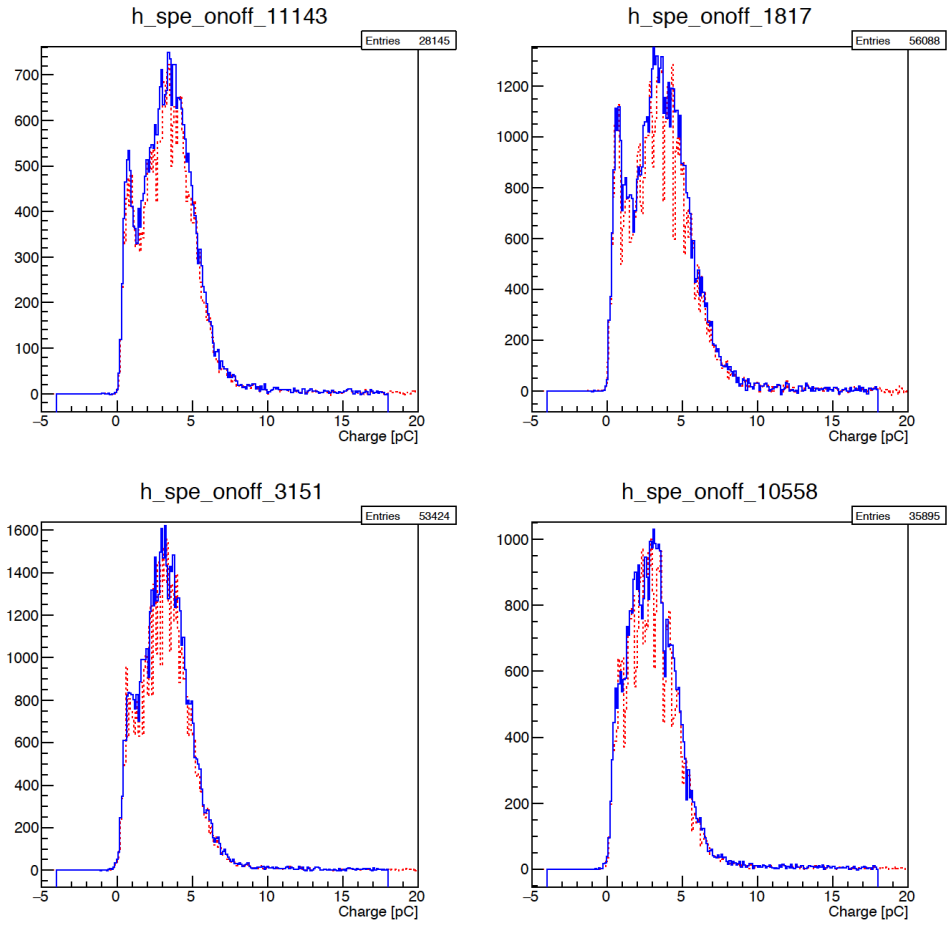

Figure 5.14: By changing the bin width from 0.1 pC (red) to 0.11 pC (blue), the spikes in charge distribution to some extents disappeared.

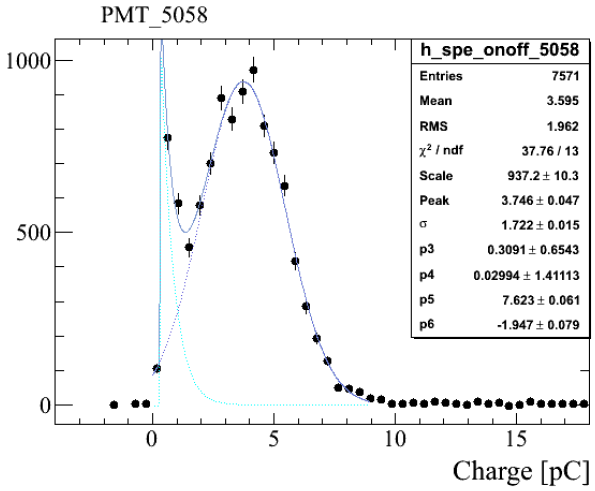

Figure 5.15: An example of Super-K's SPE at SK-IV voltage fitted by Eq. 5.5.

function for their SPE peaks were different. For the Super-K tubes, depending on the SPE spectrum the software was designed to pick the better fit from the 2 options available. The first option with higher priority was a gaussian plus exponentially modified error function as shown in Eq. 5.5

$$f_{gexp}(x) = p_0 \cdot e^{-\frac{(x-p_1)^2}{p_2}} + 0.5 \cdot e^{p_5+p_6 \cdot x} \cdot \Big(\mathrm{erf}\big(\frac{x-p_3}{p_4}\big) - \mathrm{erf}\big(\frac{x-p_1}{p_2}\big)\Big) \tag{5.5}$$

where p_i for i = 0,1,2,3,4,5,6 is the fitting parameter and erf stands for the Gaussian error function. p_1 represents the peak position. An example of this fitting result is shown in Figure 5.15. The upper limit of fitting range was set to 3σ right to the fitted SPE peak. This was to avoid the potential distortion from 2 PE peak.

However, in some cases where the voltage was lowered, a Super-K PMT's SPE peak slightly edged the energy threshold cut that left no visible exponential tail to the left. This would much likely cause the fitting with f_{gexp} in Eq. 5.5 to fail. Under this circumstance, a second fitting function of error function skewed Gaussian as shown by Eq. 5.6 would be used.

$$f_{gskew}(x) = p_0 \cdot e^{-\frac{(x-p_1)^2}{p_2}} \cdot \Big(1 + p_3 \cdot \mathrm{erf}\big(\frac{x-p_1}{p_2}\big)\Big) \tag{5.6}$$

which is demonstrated with an example in Figure 5.16.

It was noticed that the fitted peak p_1 of f_{gskew} from Eq. 5.6 was always much to the left of the actual function peak due to the skewness, therefore in the case of Eq 5.6 the x value corresponding to the function maximum was used as the SPE peak. The fitting

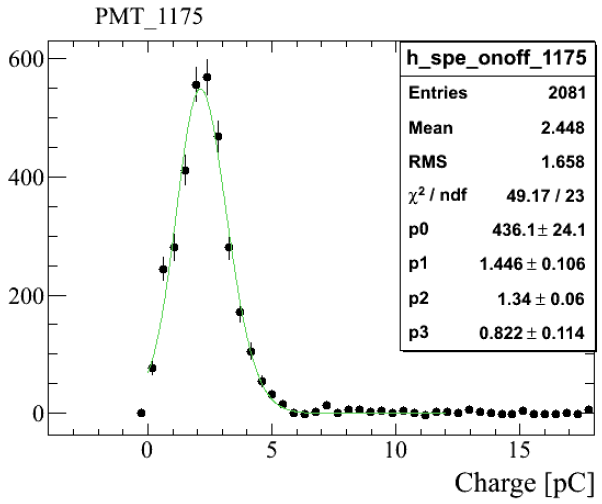

Figure 5.16: An example of Super-K's SPE at -50 V from SK-IV voltage fitted by Eq. 5.6.

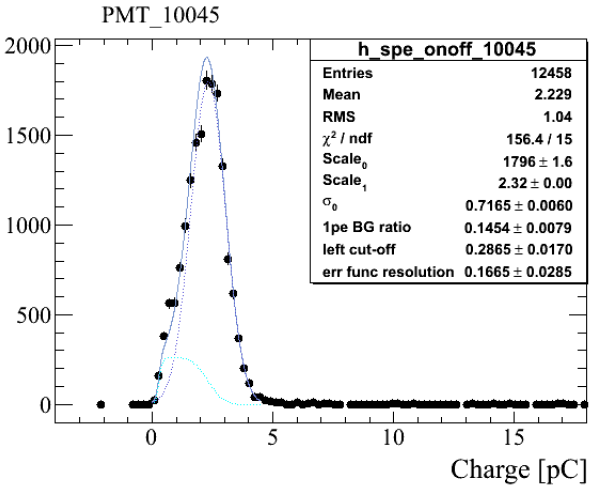

Figure 5.17: An example of Hyper-K's SPE at SK-IV voltage (for the channel) fitted by Eq. 5.7.

range was kept same as 3σ.

On the other hand, the Hyper-K PMTs do not have any exponential tail in their SPE distribution and a fitting function similar to what has been used during the pre-calibration was introduced:

$$f_{HK}(x) = p_0 \cdot e^{-\frac{(x-p_1)^2}{p_2}} \cdot \Big(1 + 0.5 \cdot p_3 \Big(\mathrm{erf}\big(\frac{x-p_4}{p_5}\big) - \cdot \mathrm{erf}\big(\frac{x-p_1}{p_2}\big)\Big)\Big) \tag{5.7}$$

An example of the Hyper-K PMT fitting is given in Figure 5.17.

Dead Channel	Blank Channel	Rejected Fitting	Flasher	Voltage out of Ranges
24	17	11	5	5

Table 5.4: The breakdowns of 62 no change PMTs in the voltage adjustment.

From the fitted SPE peak in units of pC at each voltage in Volts, the correlation was determined by fitting a power function relating the peak with voltage. Because there was a ~ 3 order of magnitude difference between the 2 values, a natural logarithmic function as shown in Eq 5.8 was actually used.

$$\log(p(V)) = \log(\alpha) + \beta \cdot \log(V) \tag{5.8}$$

where $p(V)$ is the SPE peak corresponding to voltage V, and α and β are the normalization factor and power index to be determined.

Inside Super-K, there are actually 3 generations of PMTs including the Hyper-K tubes. The oldest generation is named SK2 PMTs, which were produced in the late 1990s. The second generation is SK3 PMTs that were produced after the accident in 2000s. And the last is Hyper-K (HK) PMTs produced in 2018. Since these 3 generations of PMT have different voltage dependences of gain, they were treated separately this time. Figure 5.18 shows an example of the voltage scan for each generation of PMT. The error in peak was assigned by the fitting error of the corresponding parameter. In general the Hyper-K tubes have the smallest error size.

5.2.3 No Change Channels

The voltage scan and SPE peak fitting results of all ID PMTs were checked individually by eyes. Those tubes with bad fitting results were kept as the same as SK-IV value. An example of the bad fitting is shown in Figure 5.19. Meanwhile we set the safety range of the new target voltage to be 1400$\sim$2450 V, which was 200 V higher than the Super-K safety lower limits and 50 V lower than the upper. Any PMT with the resulted target voltage beyond this range was also not changed. In total 62 channels including those blank ones without a PMT attached were separated from the voltage adjustment. The breakdowns of those tubes are listed in Table 5.4.

5.2.4 New Voltage Results

The target gain for this voltage adjustment was decided to be 1.65×10^7, which was the initial setting for SK-III phase. Multiplied by the elementary charge, the SPE peak

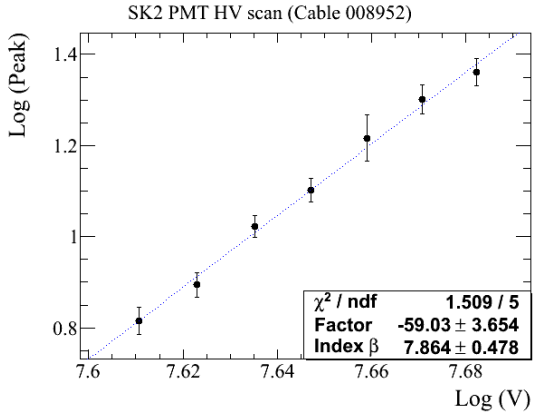

(a) SK2 PMT voltage scan example

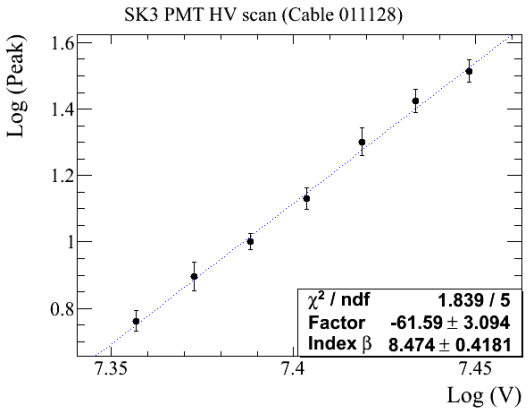

(b) SK3 PMT voltage scan example

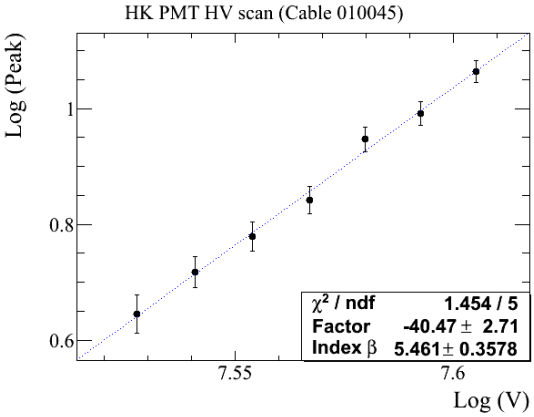

(c) Hyper-K PMT voltage scan example

Figure 5.18: Voltage scan examples for 3 generations of PMT.

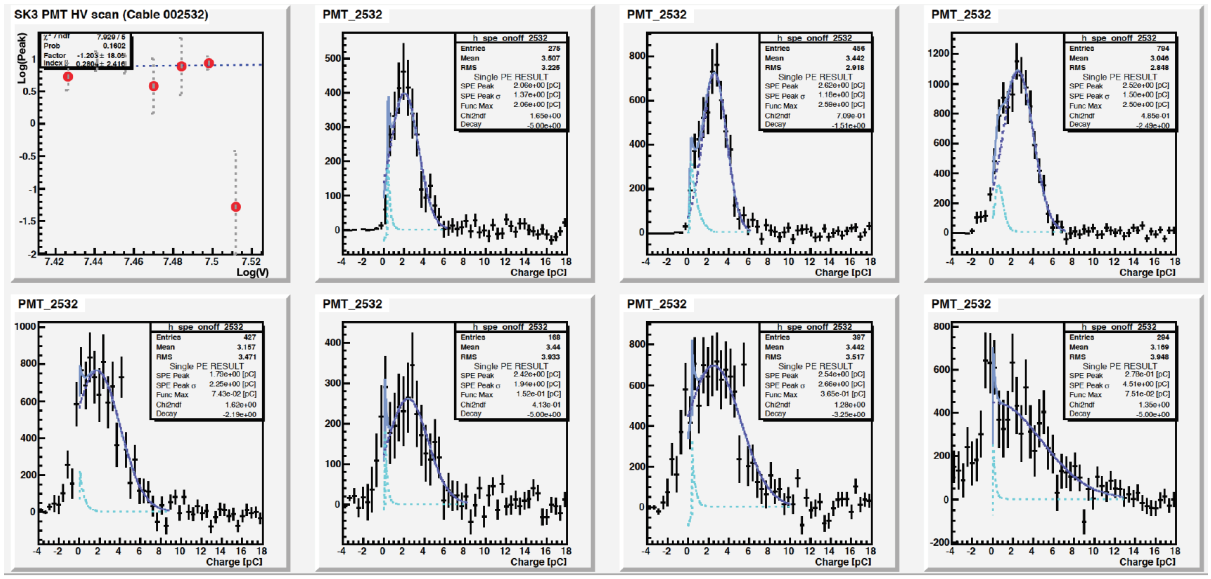

Figure 5.19: This SK3 PMT 2532 merely shows any voltage dependence of the SPE peak, meanwhile large uncertainty can be seen in the fitted result.

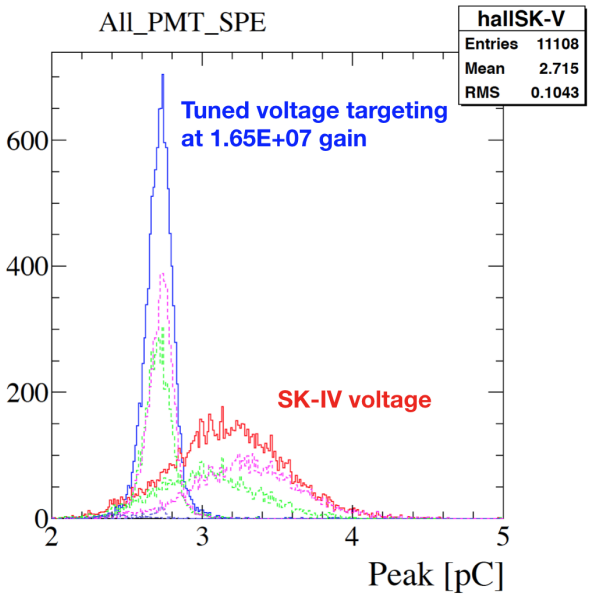

Figure 5.20: The SPE peak for all ID PMTs before the voltage adjustment (red) and after (blue). The peak average has decreased from 3.17 pC to 2.72 pC, corresponding to the gain changes from 1.98×10^7 to 1.70×10^7. The RMS has also decreased from 0.38 pC to 0.10 pC. The dashed lines represent SK2 (green), SK3 (pink), and Hyper-K PMTs (violet).

	α [pC/ V$^\beta$]	β
SK2 PMT	1.977×10^{-26}	7.960
SK3 PMT	1.748×10^{-28}	8.783
Hyper-K PMT	5.721×10^{-20}	5.971

Table 5.5: The voltage curve parameter averages of 3 PMT generations.

position corresponding to the target gain was 2.635 pC. On February 14th, 2019, the first data set at the new voltage was taken with the SN-LD. By checking the new SPE peak position after the voltage adjustment, we have confirmed that the average gain was brought down by 14.3% from the SK-IV phase, which corrected the increment over a decade. Meanwhile the gain difference among individual PMTs was also decreased to only 26.3% of the variance during SK-IV. This result is shown in Figure 5.20.

The voltage curve of each PMT generation is shown in Figure 5.21(a), with the mean value of α and β from Eq. 5.8 listed in Table 5.5. Meanwhile the new voltage settings of all PMTs is shown in Figure 5.21(b). On average the SK2 PMTs' voltage decreased by 31.7 V from the SK-IV value and SK3 40.5.V.

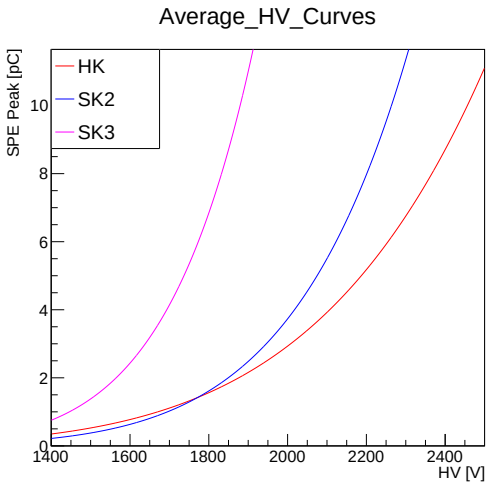

(a) Average voltage curve of 3 PMT generations

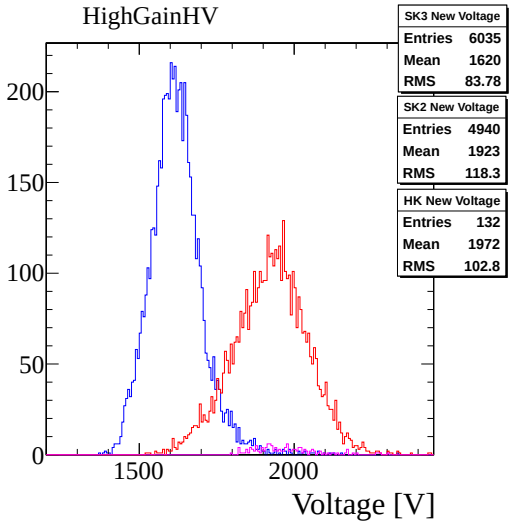

(b) Tuned result of SK-V voltages for 3 PMT generations

Figure 5.21: The average voltage curves of 3 PMT generations and the resulted SK-V voltages. In the right panel the SK2 PMTs are plotted in red, SK3 in blue, and Hyper-K in pink.

5.2.5 Uncertainties

In Super-K, the charge response of each PMT is corrected by the average gain in the tank and the relative difference of each individual tube, both of which were determined separately by other calibrations. Thus the uncertainties in the voltage adjustment result would be covered. Therefore this section does not aim to reduce the systematic uncertainties arouse in the voltage adjustment, but just to clarify the possible sources and estimate the scale.

As aforementioned in Section 5.2.1, previously in Super-K the voltage of each PMT channel was determined by the number of ADC counts. However, this old method would have a large systematic uncertainty from the water quality since the number of photon reaching each PMT is sensitive to absorption and scattering rate and the light source is not at the exact center of tank. It was noticed before that there was a $\sim$4% asymmetry in the horizontal angle ϕ for QE, which means the number of photon in the far end is $\sim$4% smaller than the near end. This asymmetry would then cause a systematic bias in the gain tuning. Nevertheless this time the SPE peak was used instead, which is in principal not affected by water quality. Although we did not know about the water transparency when this work was done, Figure 5.22 hardly shows any ϕ dependence of the SPE peak. In addition, a sinusoidal function was fitted to the ϕ distribution of SPE peaks. The

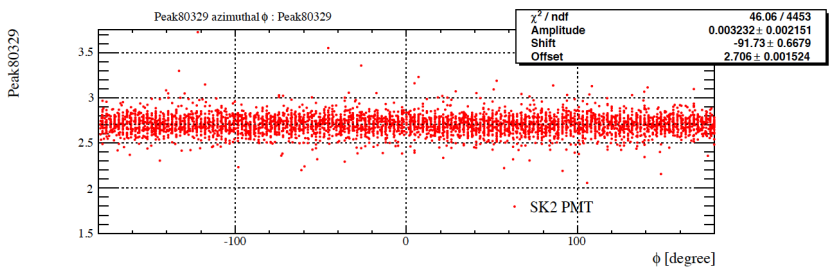

(a) SK2 PMT SPE peak ϕ dependence

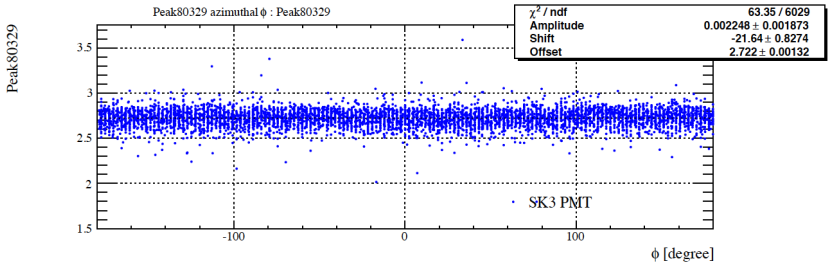

(b) SK3 PMT SPE peak ϕ dependence

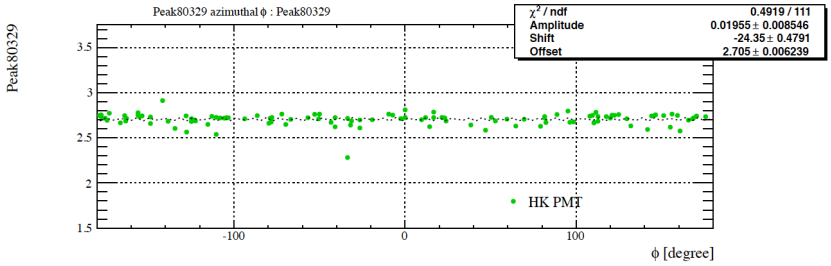

(c) Hyper-K PMT SPE peak ϕ dependence

Figure 5.22: The SPE peak of all 3 PMT generations merely shows any ϕ dependence.

	Amplitude [pC]	Phase [°]	Y-axis Offset [pC]
SK2 PMT	0.003 ± 0.002	-91.73 ± 0.67	2.706 ± 0.001
SK3 PMT	0.002 ± 0.002	-21.64 ± 0.83	2.722 ± 0.001
Hyper-K PMT	0.020 ± 0.008	-24.35 ± 0.48	2.705 ± 0.006

Table 5.6: Sinusoidal function fitting results of SPE peak ϕ dependences.

fitting results are summarized in Table 5.6.

Another potential source of distortion to a PMT's SPE charge spectrum is the occasional multiple hits, which can be checked by the PMT occupancy. If by coincidence 2 or more photons are absorbed by a PMT's photocathode within a short time window, the PMT occupancy will be enlarged and the resulted photoelectron will have the sum of photon energy if neglecting loss in photoelectric process. This will result in a higher charge in

the PMT signal output and thus distort the charge spectrum. But since we have strictly limited the fitting range as discussed in Section 5.2.2, the multi-PE hits should not to affect our SPE peak result. To verify this 3 sets of data with different light intensities were taken with the SN-LD, from which we fitted a linear function relating SPE peak to occupancy. The fitted slope of each PMT is plotted in Figure 5.23. As expected there is no systematic occupancy dependence.

Besides the potential bias in data, another source of systematic uncertainties is from the fitting and measurement errors. To estimate the uncertainty of voltage curve, the covariance matrix of parameter α and β was generated for each PMT. Since the voltage was set by other systems with high precision, the V in Eq. 5.8 was assumed to be a constant with negligible error. Therefore, the variance from the fitting uncertainty of SPE peak at a certain voltage can then be written as

$$\sigma^2_{\log(p(V))} = \sigma^2_\alpha + \log^2(V)\sigma^2_\beta + 2 \cdot \log(V)\sigma_{\alpha\beta} \tag{5.9}$$

where $\sigma_{\alpha\beta}$ stands for the covariance of the 2 parameters. Due to the error propagation of

$$\sigma_{\log(p(V))} = \frac{\partial \log(p(V))}{\partial p(V)}\sigma_{p(V)} = \frac{\sigma_{p(V)}}{p(V)}$$

the result from Eq. 5.9 directly represents the percentage of peak variance. The data at the adjusted new voltage taken on February 14th, 2019 was used to generate Figure 5.24(a). On average the voltage curve uncertainty resulted in a $\sim$5.07% variance in the fitted peak, which corresponds to $\sim$0.14 pC.

On the other hand, the statistical uncertainty was checked by 2 sets of data at the new voltage taken more than 1 week apart. Figure 5.24(b) shows this comparison. No systematic difference was observed since the mean was as small as 0.004 %. Meanwhile the individual uncertainty was RMS/$\sqrt{2}$ = 2.58% that corresponds to 0.07 pC. The details of 3 PMT generations are summarized in Table 5.7.

Last but not the least, the binning effect shown in Figure 5.13(b) may have also caused a systematic error in the fitting even though it had been to some extents removed. To check such a possibility, the same fitting functions of SPE peak were first applied to the temperature corrected ADC count profile, which was "spike-free" as shown in Figure 5.13(a). The ADC count to charge conversion was then applied to the fitted peak. Such a process did not involve the uncertainties from the spiky structures and rebinning of the PMT signal spectrum. Figure 5.25 shows the comparison of the peak from the 2 different

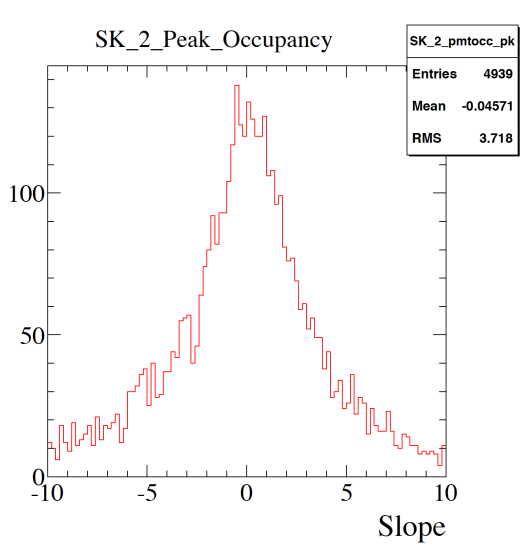

(a) SK2 PMT SPE peak occupancy dependence

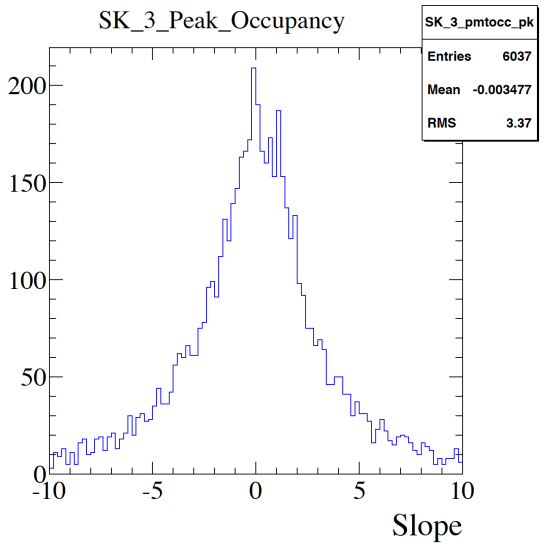

(b) SK3 PMT SPE peak occupancy dependence

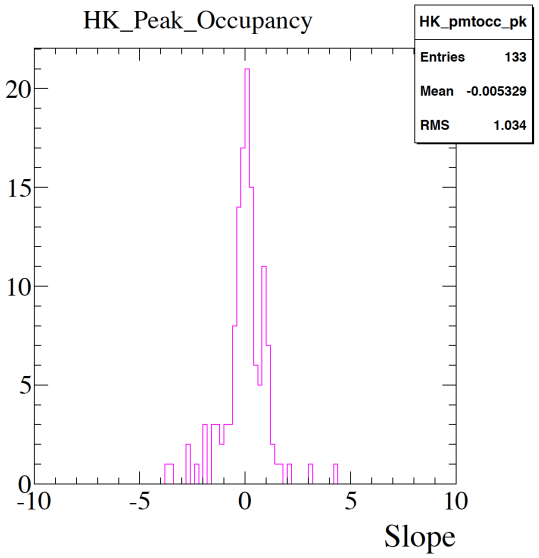

(c) Hyper-K PMT SPE peak occupancy dependence

Figure 5.23: The systematic occupancy dependence for SPE peak is verified to be negligible with the slope of peak-occupancy relation averaging at 0. The spread comes from the larger uncertainties in lower occupancy tubes.

PMT Type	Systematic Error	Statistical Error
Hyper-K	3.80%	1.33%
SK2	4.07%	2.75%
SK3	5.94%	2.45%

Table 5.7: Systematic and statistical uncertainties in SPE peak for the 3 PMT generations.

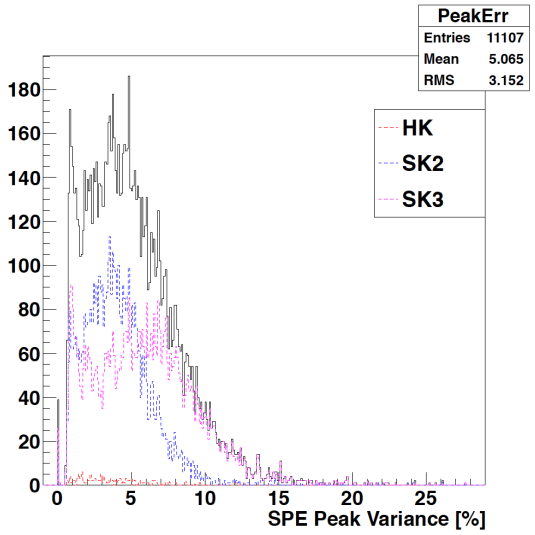

(a) Peak variance from the voltage curve uncertainty

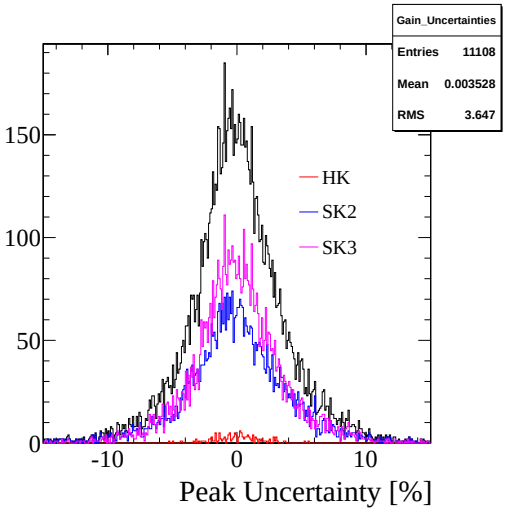

(b) Statistical uncertainty of SPE peak

Figure 5.24: The systematic and statistical uncertainties from fitting of SPE peak. The SK2, SK3, and Hyper-K PMTs are in blue, pink, and red respectively.

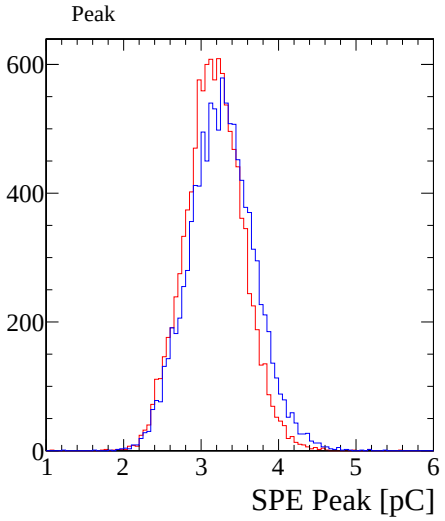

(a) SPE peak from charge (ADC count) in red (blue)

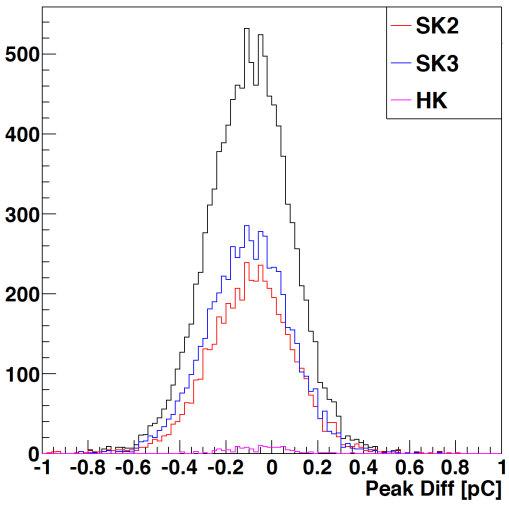

(b) Peak differences between the 2 processes

Figure 5.25: SPE peak check from the 2 different processes.

processes on the data taken at SK-IV voltages.

Several data at different points of voltage scan was checked as well as the data taken at the new SK-V voltage. The result is summarized in Table 5.8. It shows that the discrepancy in the peak was larger at higher voltage than the lower, which would give rise to a

	All	SK2	SK3	Hyper-K
SK-IV -75 V	-0.082	-0.068	-0.094	-0.029
SK-IV +0 V	-0.098	-0.092	-0.105	-0.057
SK-IV +75 V	-0.101	-0.101	-0.102	-0.070
SK-V	-0.009	-0.006	-0.012	0.009

Table 5.8: The differences in average SPE peak calculated by charge peak - ADC count converted peak. The first column represents the voltage setting for each row. The 3 generations of PMT are also listed. The peak differences are written in units of pC.

smaller slope in the fitted voltage curve. Nevertheless the difference in the peaks at the new voltage was surprisingly small. Therefore the discrepancy at the high voltage in the peaks fitted from charge and ADC count may help to explain the offset in the resulted peak average of the tank. Since the slope of voltage curve was underestimated, it would result in an insufficient correction in the voltage to achieve the target gain and thus a larger average peak value.

5.3 Timing Calibration

The timing of each ID PMT is essential to event reconstruction and various physics analyses. To understand whether the hits in multiple PMTs are connected to a single interaction, one needs a precise time measurement free of systematic biases. In Super-K, this is achieved by applying a correction in time for different signal charges. The analysis framework of timing calibration was first developed by [25], with several modifications and updates from this work. This chapter describes in details how the timing calibration was done for SK-V.

5.3.1 Overview

The 2 major sources of timing systematic biases are the differences in electronics processing time and the time walk effect at the timing gate threshold in TDC. As shown in Figure 5.26, the time walk effect originates from the difference in signal charges since the higher charger signal will rise more rapidly and causes a fake "early arrival" relative to the lower charge signal.

Figure 5.27 shows the experimental set ups for timing calibration. A USHO-KEC100 nitrogen-dye laser was used as the light source. The wavelength was shifted from 337 nm to 398 nm by the dye, which is roughly the peak wavelength of PMTs. There were 2

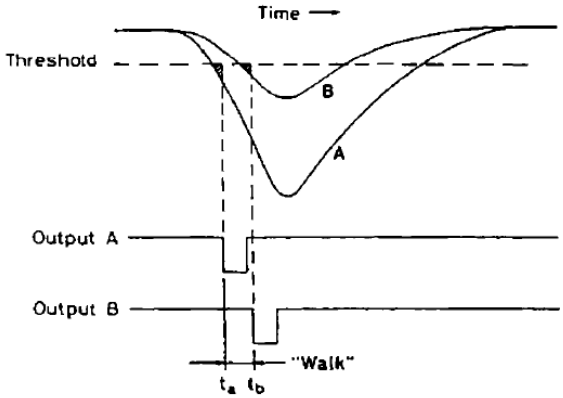

Figure 5.26: The time walk effect caused by different pulse amplitudes at the threshold [26].

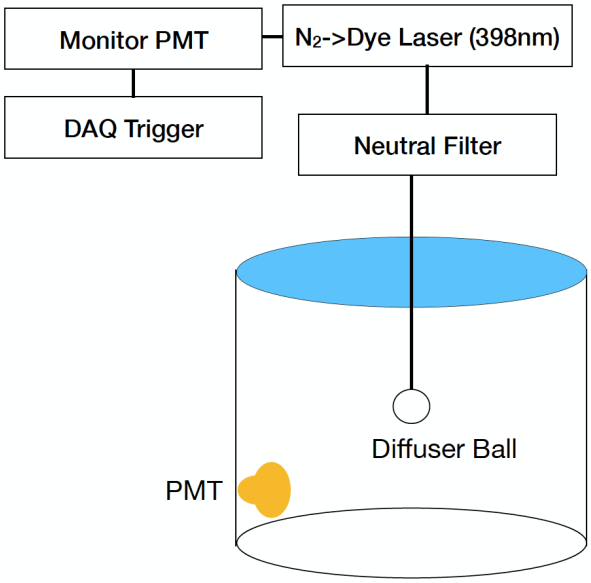

Figure 5.27: The set ups for timing calibration.

signal outputs from the laser. One was going into a 2-inch monitor PMT placed outside the tank. To trigger a DAQ from the laser pulse one and only one hit in the monitor PMT was required. The charge and timing from the monitor PMT were separately recorded in QBEE channel 15001 and 15009. In the other output, the laser light passed a neutral filter before entering the tank via the diffuser ball. The filter is a rotating plate of differential transparency that allowed us to control the intensity of light being injected into the tank remotely. The position of the diffuser ball was the same as in Table 5.2.

The relative time in each PMT can be then written as

$$T_i = -t_i + tof_i + t_{lsr} \tag{5.10}$$

where the t_{lsr} is the time stamp of a laser signal, tof_i is the "time-of-flight" that needed by light to travel from the diffuser ball to PMT i in water, and t_i is the time stamp of the hit in that PMT in response to the laser light. An implicit term in Eq. 5.10 is the time for signal traveling in each cable and being processed in each QBEE channel, which are contained by t_i. Meanwhile to correct for the time walk, the relative timing T_i was calculated at different charges of signal ranging from 0 to 3981 pC. It was found that the filter position ∼3500 would give the maximum light intensity, meanwhile 3950 the minimum. A piecewise polynomial function so-called "T-Q curve" was fitted for each PMT so that the delay caused by the time walk effect at different charges can be estimated. Then, by applying the relative timing correction T_i to the real data given their charge information we can trace back on the interaction vertex and time with improved precision.

5.3.2 Time Peak Fitting

The time and charge information of each PMT were first used to generate a 2-D display as shown by Figure 5.28. As a Super-K convention, the earlier hits are of larger numbers in the y-axis. There are 384 time bins between 1100 and 1300 ns. Each time bin spans 1/1.92 ns, which is the same as the TDC resolution. Along the x-axis the charge is grouped into 180 Q bins. The conversion is linear in the low charge region and logarithmic in the high as denoted in Eq. 5.11.

$$\#\ \mathrm{Q\ bin} = \begin{cases} 5 \cdot \mathrm{Q} & (0 < Q \leq 10\ \mathrm{pC}) \\ 50 \cdot \log_{10}(\mathrm{Q}) & (10 < \mathrm{Q} \leq 3981\ \mathrm{pC}) \end{cases} \tag{5.11}$$

In this work, the charge in each PMT channel was calculated directly from its raw ADC counts. To find the peak in time, a time slice was taken from each Q bin and re-plotted into a 1-D histogram. Due to the distortion from scattered hits, pre-, and late pulses, the time distribution turned out to be an asymmetric peak. A damped Gaussian function was used for fitting as shown by Eq. 5.12.

$$f(T) = max \cdot \exp\Big(\frac{1 + tmp - \exp(tmp)}{effAsy^2}\Big) \tag{5.12}$$

where

$$tmp = effAsy \cdot \frac{T - T_{peak}}{\sigma_T}$$

In Eq. 5.12, the amplitude max, peak T_{peak}, width σ_T, and damping factor $effAsy$ are the fitting parameters. In the limit of small damping factor that corresponds to the nearly

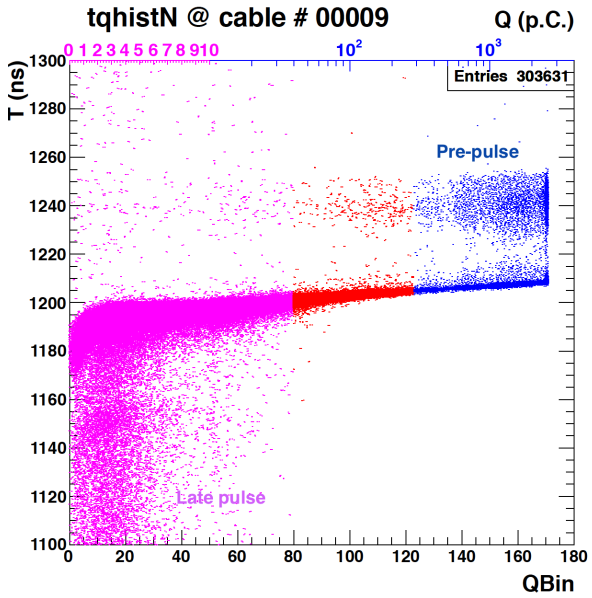

Figure 5.28: An example of the time-charge 2-D display. The low (medium, high) charge range is plotted in pink (red, blue). The scattering such as pre-pulses and late pulses were excluded from this analysis.

symmetric case, the fitting approximates to a pure Gaussian function if only considering up to the 2nd order derivative in Taylor expansion. For asymmetric cases, practically derivatives up to 4th order were included in calculation.

Previously in SK-IV, a smearing was applied (Figure 5.29) to the time distribution in each Q bin before fitting. The smearing was first introduced to solve the pedestal fluctuation problem happened to the ATM modules. It was then done by summing over the time bins' entries assuming gaussian distributions. However, this would, especially in the low charge region, cause the smeared peak deviated from the original one, as well as a broadening effect that would affect the determination of detector time resolution. Figure 5.30 shows the difference between the raw data peak and smeared peak against Q bins.

Since there is no pedestal fluctuation issue in the QBEE system meanwhile the raw data had no problem with the fitting, the smearing process was removed from the timing calibration this time. As a result, the fitted time peaks in the small Q bins were expected to be more accurate. An example of the fitting on raw data is given in Figure 5.31. Meanwhile due to finite time bin width, the peak in the histogram can be differed from the true peak by up to 0.5/1.92 ns. Such a shift was estimated and corrected by checking the change in mean every time an entry was added.

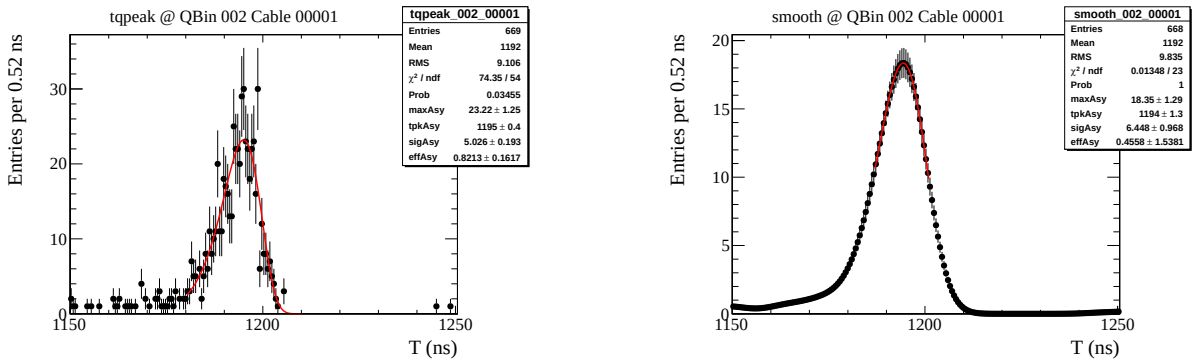

(a) Raw data without smearing

(b) Smeared data

Figure 5.29: The smearing effect to the time peak in the 2nd Q bin.

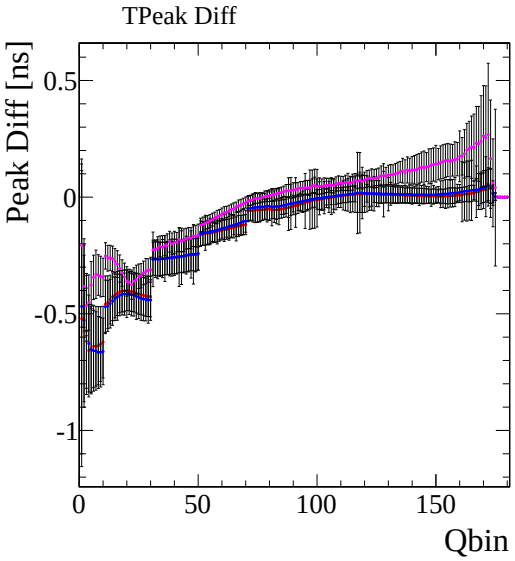

Figure 5.30: The average peak difference from $T_{raw} - T_{smear}$ across the Q bins. Error bars stand for the standard deviation among ID PMTs. The red (blue, pink) dots represent SK2 (SK3, Hyper-K) PMTs.

5.3.3 T-Q Curve Fitting

From the binning shift corrected T_{peak}'s, a polynomial curve as defined in Eq. 5.13 was used to determine the charge dependence of relative hit time in each PMT.

$$T(x) = \begin{cases} \text{pol3}(x) & 0 \leq x \leq 10 \\ T(10) + (x-10)[T'(10)|_{x=10^-} + (x-10)\text{pol3}(x-10)] & 10 < x \leq 50 \\ T(50) + (x-50)\text{pol6}(x-50) & 50 < x \leq 180 \end{cases} \tag{5.13}$$

where x is the Q bin number and pol$N(x)$ represents the polynomial function of order

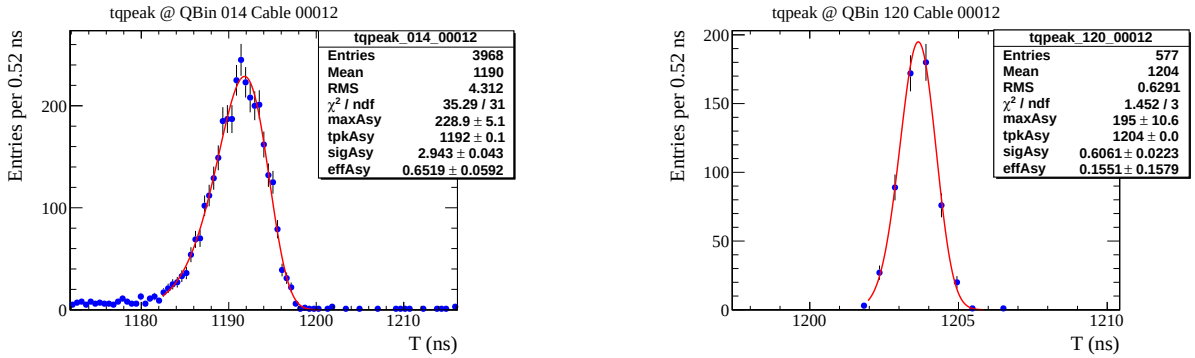

(a) Fitting on raw data in Q bin #14

(b) Fitting on raw data in Q bin #120

Figure 5.31: An example of raw time data peak fitting.

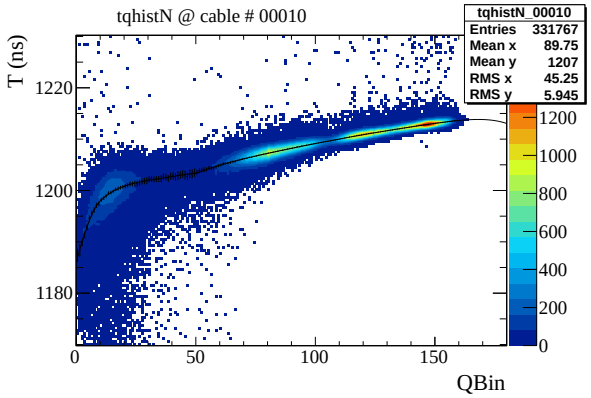

Figure 5.32: In the empty Q bins the T-Q curve tended to bend down. Attempts were made to extend the data tail over Q bin 170 but the issue still remained.

N. However, it happened that the data could not span full 180 Q bins even with the maximum light intensity passing through the neutral filter. This caused a difficulty in the fitting of the largest 5∼10 Q bins. As shown in Figure 5.32, the high order polynomial tended to bend down in the empty Q bins, which causes a big uncertainty in the fitted T-Q curve.

A solution to this issue was extrapolation. A Spline5 and Newton series were applied respectively to predict the data points in the empty Q bins based on the existing ones. First a Spline5 interpolation was applied to the full dataset in each PMT, which assumes differentiability and same curvature at each junction point as

$$\begin{cases} q_i'(x_i) = q_{i+1}'(x_i) \\ q_i''(x_i) = q_{i+1}''(x_i) \end{cases} \tag{5.14}$$

where $1 \leq i \leq n-1$ is the ith point in a total set of n. Based on the right most data

point, an extrapolation was done assuming the derivative does not change. However, due to the natural fluctuation in the data points the derivative between 2 consecutive points is usually much different from the average trend of the group. Since the data usually saturated in the large charge region that caused a "shooting up" in the last several points, the Spline5 extrapolation would easily exaggerate the real case. Therefore a second hand was introduced to kill the divergent effect from the large derivatives.

Newton's series can be written as

$$f(x) = \sum_{k=0} \binom{x-a}{k!} \Delta^k |f|(a) \tag{5.15}$$

where Δ^k is the kth order difference counted backward from the point a and

$$\binom{x-a}{k!} = \frac{(x-a)(x-a-1)(x-a-2)...(x-a-k+1)}{k!}$$

Thanks to the fact that the data points had integer uniform step sizes in x-axis: 1 Q bin, the binomial coefficient and $k!$ are cancelled out since we always considered the case where $x = a + 1$ for extrapolation. Meanwhile to suppress the extreme derivatives in the extrapolation, a weight negatively related to each Δ^k term was included. The maximum order of difference was taken to be 4. Effectively, the Newton series extrapolation as given by Eq. 5.16 would lead to a "flatter" prediction than the real case. Therefore by taking the average of the 2 extrema: Spline5 and Newton series extrapolations, it was hoped that the extrapolated points would approximate the reality better.

$$f(x) = \sum_{k=0}^{4} \frac{(1 - \Delta^k |f|(x_k))\Delta^k |f|(x_k)}{2 \cdot \sum_{j=0}^{4} \Delta^j |f|(x_j)} \tag{5.16}$$

Moreover, since a larger charge will have faster rising and hence "fake" earlier hit, it is unnatural for the extrapolated points to curve down. Thus in such a case where a negative slope was extrapolated in the empty Q bins, a linear extrapolation based on the data of Q bin range 120∼end would be used instead. Figure 5.33 gives an example of the extrapolation to Q bin 180.

On the other hand, another problem rouse in the low charge region. Due to this time the average gain has been lowered in the tank as discussed in Section 5.2.4, it was difficult to accumulate enough statistics for Q bin #1, which is close to the 0.25 PE energy threshold cut. Many channels did not have a time peak fitted in this Q bin because of the low signal-to-noise ratio. In such cases, similarly a Spline5 extrapolation was applied

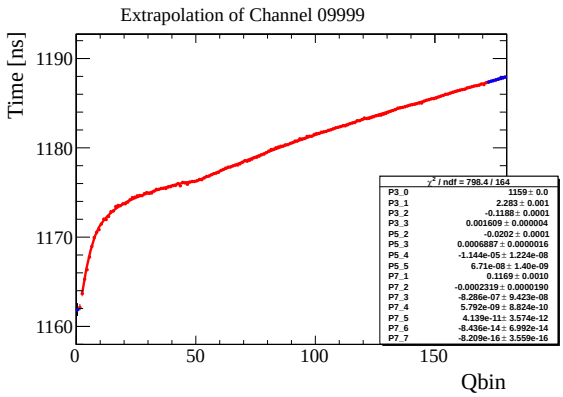

Figure 5.33: An example of extrapolation. The fitted time peak from the original data is plotted in red, while the extrapolated prediction is in blue.

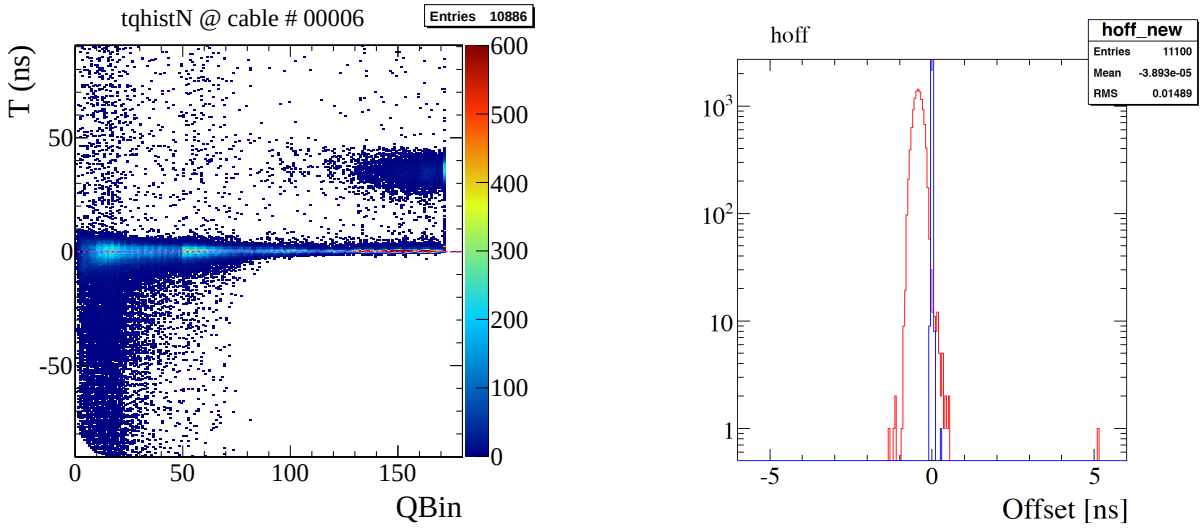

(a) 2-D display after T-Q curve subtraction

(b) In the right panel the timing averages of the subtracted 2-D display

Figure 5.34: The time axis offsets after subtracting the preliminary T-Q curve for all channels is plotted in red. The result after offset correction with the final T-Q curve is plotted in blue.

(as shown in Figure 5.33 and when the extrapolated slope was not positive a linear fit based on the average trend was instead used. Another problem about Q bin #1 was that the low statistics caused a large uncertainty in determining the constant term in the T-Q curve function Eq. 5.13. To solve it a preliminarily fitted T-Q curve was at first subtracted from the raw data. After doing so the time-charge 2-D display would become a flat curve centering around 0 in the time axis. Then the offset in time was calculated and added into the preliminary T-Q curve. Figure 5.34 illustrates this process.

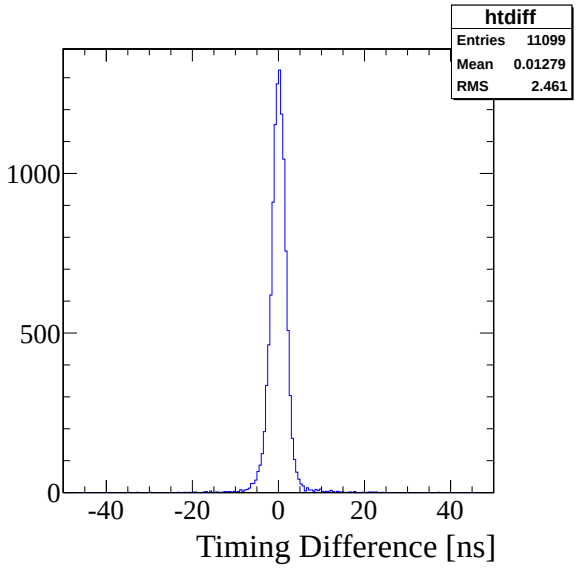

Figure 5.35: An agreement up to 0.01 ns was achieved between the 2 TQ maps after the global timing offset correction.

From the final T-Q curve, a list called "TQ map" of the 15 parameters used in the fitting was made for all ID PMT channels. The "TQ map" is what would be used in the upcoming various physics analyses and new Monte Carlo simulations (MC).

5.3.4 Global Timing Offset

Besides the relative timing difference in each individual PMT channel, there was a global timing offset in all channels first observed when upgrading from ATM to QBEE in Super-K. However, unfortunately the source of such a time shift in the QBEE system remained unclear. As a temporary solution, a constant shift was added to the 0 order term in the SK-IV TQ map so that it matched up with the previous one in SK-III. And this has also been done this time. A shift averaged at 52.8 ns was observed between the SK-V and SK-IV TQ maps. Comparing to the previous value at 40 ns, the major part in the difference may be the time offset caused by the new discriminator for the monitor PMT. Figure 5.35 shows the global timing difference between the new TQ map and the previous one of SK-IV after a correction of 52.8 ns.

However, this correction by aligning the 2 generations of TQ maps will carry the errors from the previous to the next. Since the alignment is based on the 0 order constants that has the lowest statistics, this error propagation may be a severe problem. Thus a detailed investigation on the global timing offset in the electronics is urgently needed. An independent method (from the TQ map itself) to correct this shift will prevent the accumulation of errors after many generations.

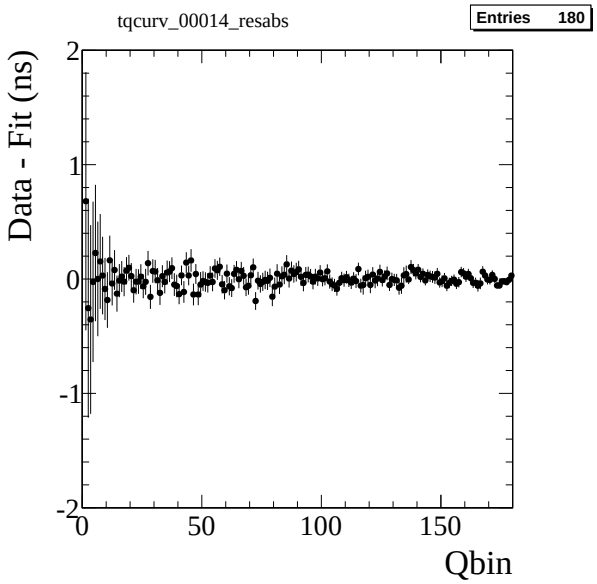

Figure 5.36: The difference between data and fitting in all Q bins of PMT 00014. Larger discrepancy exists in the low charge region.

5.3.5 Timing Correction Quality Checks

The T-Q curve fitting quality was checked by the difference in the time peak and fitted value as shown in Figure 5.36. Except for the slightly larger discrepancy in the charge region < 1 pC due to the low statistics, the data and fitted curves agreed with each other within 1 time bin width. Figure 5.37 shows the average and standard deviation of the data&fitting difference in Q bin range 5∼end for all ID PMTs.

To verify that the time walk effect has been successfully corrected in all ID PMTs, a pol6 function was used to fit the T-Q curve subtracted 2-D display for each PMT as shown in Figure 5.34(a) as an example. The fitted results have confirmed that the subtracted 2-D displays were flat with negligible curvature as shown in Figure 5.38 and Table 5.9.

For the consistency check of TQ maps, the time peak in this data set T_{peak}^{corr} corrected by the SK-V TQ map was compared to the previous Linear Accelerator (LINAC) data hit times corrected by the SK-IV TQ map. A discrepancy was seen in the charge range < 1 PE, which corresponds to the first few Q bins. Figure 5.39 gives a few examples of this comparison at several charge ranges.

It remained unsolved why the USHO-KEC100 laser data has broader width in the time distribution compared to the LINAC data as shown in Figure 5.39a. The PMT time

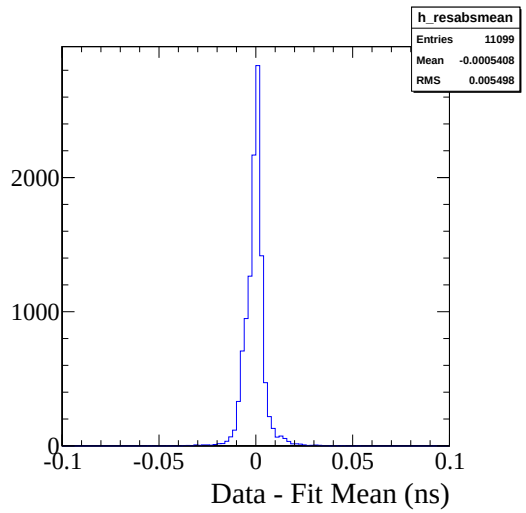

(a) Average data-fitting differences of all ID PMTs

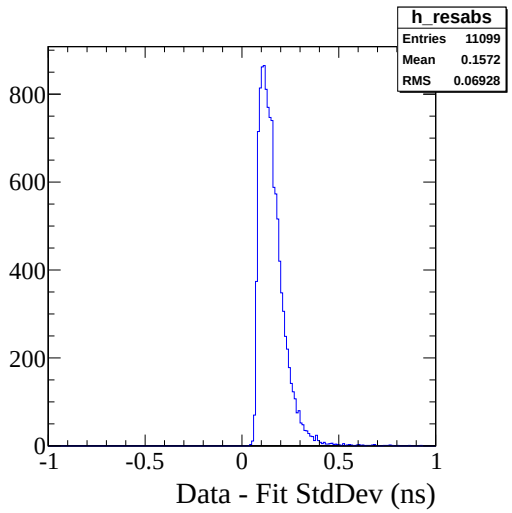

(b) Standard deviation of data-fitting difference of all ID PMTs

Figure 5.37: The data and fitted results show good agreement in Q bin 5∼end.

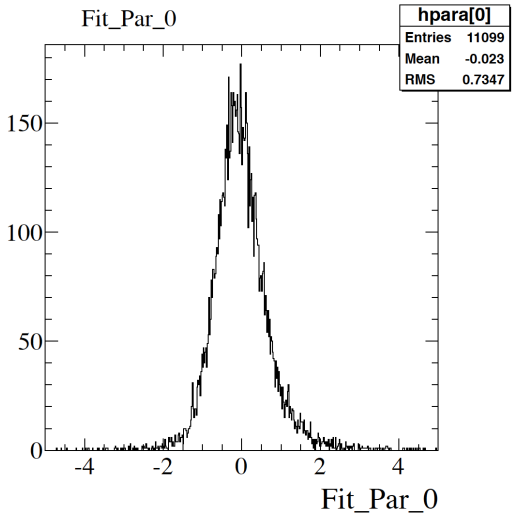

(a) 0 order constant of the pol6 fitting

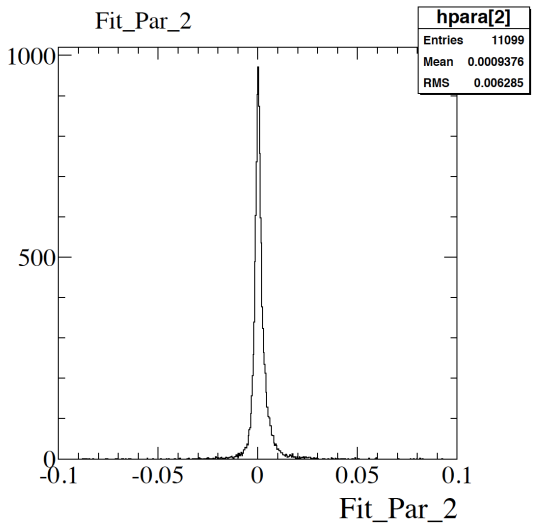

(b) coefficient of the 2nd order term in the pol6 fitting

Figure 5.38: The fitting on the T-Q curve subtracted 2-D display shows flat distribution. All 7 coefficients are centered at 0.

p_0	-0.02 ± 0.73
p_1	-0.02 ± 0.09
p_2	$(0.09 \pm 0.6) \times 10^{-2}$
p_3	$(-0.02 \pm 0.37) \times 10^{-3}$
p_4	$(0.16 \pm 0.90) \times 10^{-5}$
p_5	$(-0.02 \pm 1.19) \times 10^{-7}$
p_6	$(0.06 \pm 4.67) \times 10^{-10}$

Table 5.9: Averages of the fitted parameters from the time walk effect corrected T-Q data of all ID PMTs. The standard deviation in each parameter was assigned as the uncertainty.

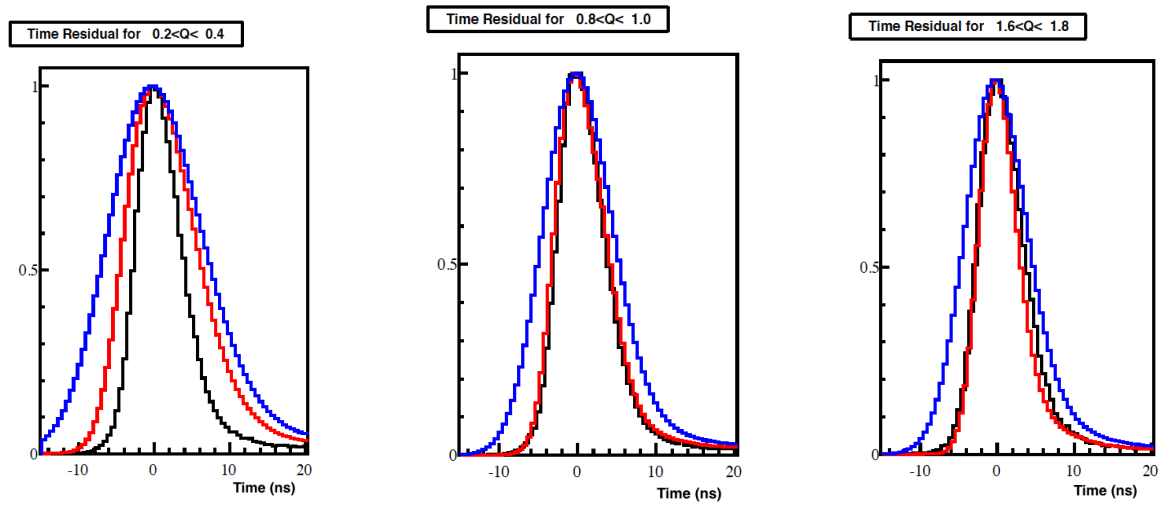

(a) Hit time comparison for 0.2 < Q < 0.4 PE

(b) Hit time comparison for 0.8 < Q < 1.0 PE

(c) Hit time comparison for 1.6 < Q < 1.8 PE

Figure 5.39: The black curves are the LINAC corrected hit times. The red represent the T_{peak}^{corr} taken this time. The blue are the corrected time peak from the smeared data that were NOT used for the timing calibration but plotted just to show the broadening in the timing resolution.

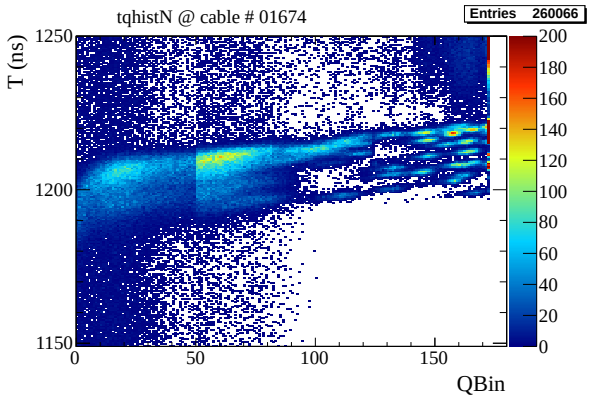

Figure 5.40: An example of scattered distribution in T-Q 2-D display.

Largely Scattered		Less Severe		
202	1674	4418	4641	4778
2267	2532	4825	5336	6744
2882	4070	7404	9061	9195
4572		9506	9691	10356

Table 5.10: PMT channels with similar feature to Figure 5.40. In the "largely scatterd" case the data were too scattered that no T-Q curve could be fitted. In the "less severe" case there were some small "blobs" of scatter but still a usable T-Q curve could be fitted.

resolution is related to the signal charge and for low charges the resolution tends to be worsen. But this feature was not seen in the LINAC data. An investigation on this issue will be carried out soon. Nevertheless, the 2 data sets still showed great consistency for Q $>$ 1 PE.

5.3.6 Bad Channels

In total 47 PMT channels (including the 17 blank ones with no PMT) were identified to be bad channels. Those PMTs either showed no response to the laser light or had a narrow charge output range up to only $\sim$ 100 PE. Most of them have also been identified by other studies. These channels will not be used in the physics analyses during SK-V.

Besides the already known bad channels, there were some others having scattered distribution in the 2-D display that no clear T-Q curve can be fitted as shown by the example in Figure 5.40. These PMTs have not been listed as bad channels yet since attempts to recover them are to be made. A list of this kind of PMT channels is summarized in Table 5.10.

6 Inputs to Super-K Detector Simulation

The Super-K Detector Simulation (SKDETSIM) is a GEANT3 based Monte Carlo simulation program. With the calibration results, SKDETSIM was tuned to match the environmental set-ups of each Super-K phase. In the new SK-V environment, the major contributions from this work to SKDETSIM are the Hyper-K PMT charge response and the new Super-K detector timing resolution.

6.1 SPE Charge Distribution for Hyper-K PMTs

To determine Hyper-K PMT's SPE charge model, a Ni-Cf source that can emit isotropic γ-rays stably at SPE level was used. As mentioned before, the actual charge response in PE of each PMT channel was determined by 2 constants: the average conversion factor from pC to PE in the tank and the relative ratios among PMTs. The average conversion factor was found to be 2.447 pC/PE for Hyper-K PMTs.

There were 2 sets of data taken at different gains and energy threshold cuts with the Ni-Cf source. One was at the gain after the voltage adjustment as mentioned in Section 5.2.4 with the default energy threshold at -0.69 mV, which corresponds to roughly 0.25 PE. The other was at a higher gain level about 1.6 time larger and energy threshold at -0.40 mV. The reason for the second data set at higher gain lower threshold was to check the SPE profile being cut out below the -0.69 mV threshold. In the case of Super-K PMTs, the higher gain data set would have a more profound exponential peak around 0 that helped the extrapolation below the energy threshold. However, in the case of Hyper-K PMT as shown by Figure 6.1, no clear peak was seen around 0 even after the gain was increased.

Based on the data shown in Figure 6.1(b), a preliminary fit without considering the threshold effect was generated using Eq. 6.1. Since the gain was increased, the 2PE peak was also taken into account. The fitting result is shown in Figure 6.2. In SKDETSIM, the SPE charge distribution model was sliced into 5000 bins in the range of 0$\sim$50 PE and the integrated area of each slice was used to decide whether to keep the randomly generated charge for downstream simulation or not.

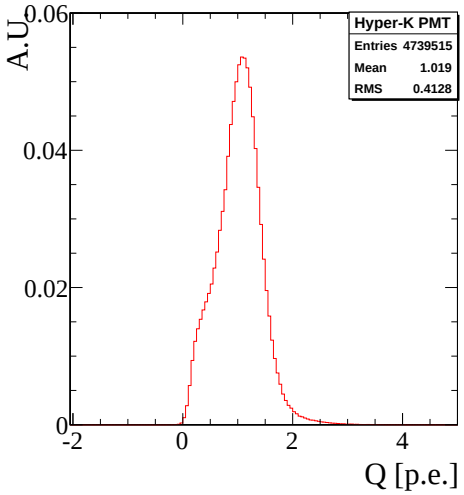

(a) Hyper-K PMT Ni-Cf data at normal gain normal threshold

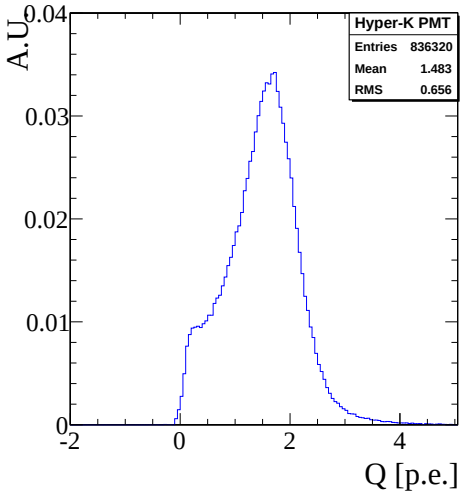

(b) Hyper-K PMT Ni-Cf data at higher gain lower threshold

Figure 6.1: No clear peak emerged at around 0 after increasing the gain and lowering the threshold cut. Both peaks were normalized by the number of events.

$$
\begin{aligned}
f(x) = & \underbrace{p_0 \cdot e^{-\left(\frac{x-p_1}{\sqrt{2}p_2}\right)^2}}_{\text{SPE Gaussian peak}} + \underbrace{p_3 \cdot e^{-\left(\frac{x-p_4}{\sqrt{2}p_5}\right)^2}}_{\text{2PE Gaussian peak}} \\
& \underbrace{+ 0.5 \cdot p_6 \cdot p_0 \cdot \left(\operatorname{erf}\left(\frac{x-p_7}{p_8}\right) - \operatorname{erf}\left(\frac{x-p_{11}}{p_{12}}\right) \right)}_{\text{SPE Back scattering}} \\
& \underbrace{+ 0.5 \cdot p_9 \cdot p_3 \cdot \left(\operatorname{erf}\left(\frac{x-p_{11}}{p_{12}}\right) - \operatorname{erf}\left(\frac{x-p_{13}}{p_{14}}\right) \right)}_{\text{SPE-2PE Back scattering}} \\
& \underbrace{+ 0.5 \cdot p_{10} \cdot p_3 \cdot \left(\operatorname{erf}\left(\frac{x-p_7}{p_8}\right) - \operatorname{erf}\left(\frac{x-p_{13}}{p_{14}}\right) \right)}_{\text{2PE Back scattering}}
\end{aligned}
\tag{6.1}
$$

Besides the missing part below the energy threshold, another correction to the SPE charge model is the smearing effect due to the QBEE channel resolution around the edge of threshold cut. This effect can be seen in Figure 6.1(a)&(b) as the left side of the SPE profiles are not perfectly vertical. Previously in SK-IV, this smearing effect was estimated by comparing difference in the data taken by ATM module and QBEE system. However, for Hyper-K PMTs no ATM data is available. Thus a new method to determine

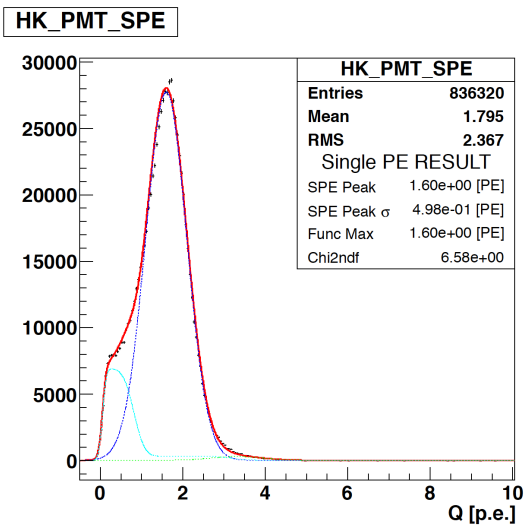

(a) Fitting on the Hyper-K SPE charge distribution from Ni-Cf data

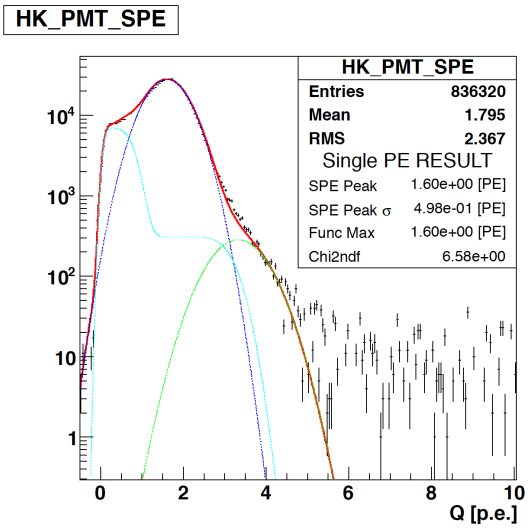

(b) Fitting on the Hyper-K SPE charge distribution from Ni-Cf data in logarithmic scale

Figure 6.2: The fitting of the SPE charge distribution of Hyper-K PMTs with Ni-Cf data. The blue curve represents the SPE peak, green the 2PE peak, and cyan the integrated back scattering components. The red curve shows the overall fitting result.

the energy threshold smearing effect as well as the extrapolation below that threshold is currently under investigation.

6.2 Timing Resolution

At each Q bin, the timing resolution of ID PMTs was determined by integrating all relative timing corrected on-time hits triggered by the USHO-KEC100 laser. Similar to SK-IV, this time the integrated timing distributions were fitted by an asymmetric Gaussian function as defined in Eq. 6.2.

$$f(t) = \begin{cases} A_1 \cdot \exp(-(t - T_{peak})^2/\sigma_1^2) + B_1 & (t > T_{peak}) \\ A_2 \cdot \exp(-(t - T_{peak})^2/\sigma_2^2) + B_2 & (t \leq T_{peak}) \end{cases} \tag{6.2}$$

where the A_i, B_i and σ_i $(i = 1, 2)$ are the fitting parameters. Continuity and differentiability are also required at the boundary $t = T_{peak}$. SInce the Super-K and Hyper-K PMTs are very different in timing resolution, they were treated separately this time. To avoid the potential bias from different statistical sizes, i.e. the number of hits gets larger when light intensity gets larger, the integrated timing distributions were normalized by their number of events respectively. Figure 6.3 shows the examples of fitting with Eq 6.2. The new timing resolution at SPE (Q bin = 14) agreed with the SK-IV value for Super-K

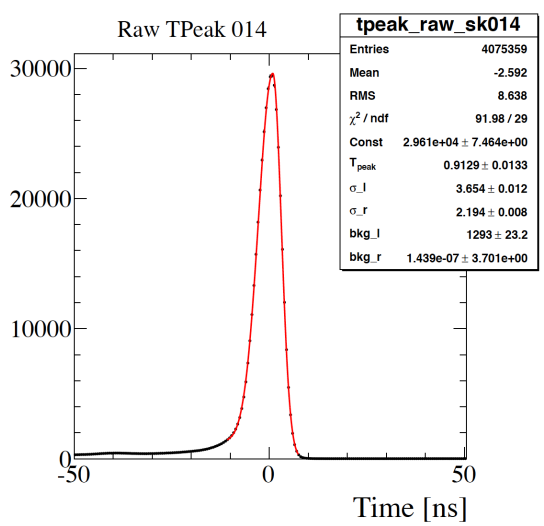

(a) Integrated Super-K PMTs' timing distribution and fitting at Q bin = 14

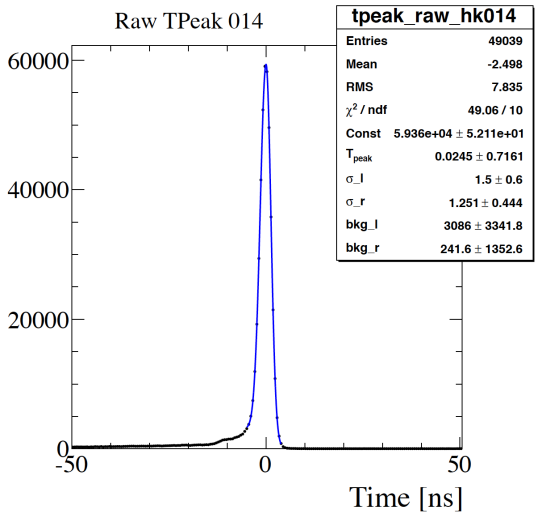

(b) Integrated Hyper-K PMTs' timing distribution and fitting at Q bin = 14

Figure 6.3: Fitting of the integrated timing distribution of Super-K and Hyper-K PMTs. The events from each PMT were corrected by the TQ map before being summed up. The x-axis has the reversed time direction, i.e. larger number means earlier hit in time. σ_r ($_l$) is the parameter σ_1 (σ_2) in Eq. 6.2.

PMTs within the range of TDC resolution. But since the voltage setting of SK-V is lower than SK-IV, this agreement means that the SK-V timing resolution is effectively better since a PMT's time response will degrade with lower voltage.

The σ_i's of the Super-K and Hyper-K PMTs' in the charge range if 0.01∼1000 PE are shown in Figure 6.4. Compared to the Super-K PMT, the Hyper-K one has stronger pre-pulses in the large charge $>$ 1000 PE and are closer to the main peak in time. Therefore the contamination from the pre-pulses is severer for the Hyper-K tubes, which is the reason of an increment in their σ_1 in the large charge region. Meanwhile another feature of Hyper-K PMTs different from the Super-K ones is the "bump" at Q∼2 PE. At this charge region, the timing resolution does not improve with increasing signal strength but goes in the opposite direction. Such a trend can also be seen in the Super-K tubes, but instead of totally reversing the trend it only results in a slower decrement. The cause of such a "bumpy" feature in the timing resolution is still under investigation.

The timing resolutions shown in Figure 6.4 are input into SKDETSIM to generate the PMT response time using the probability density function

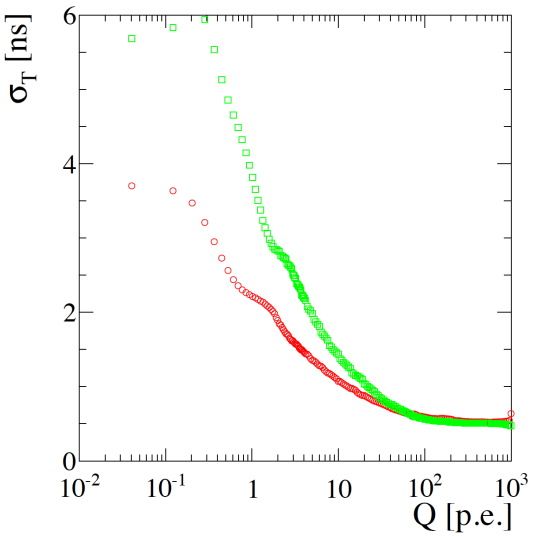

(a) The timing resolution of Super-K PMTs

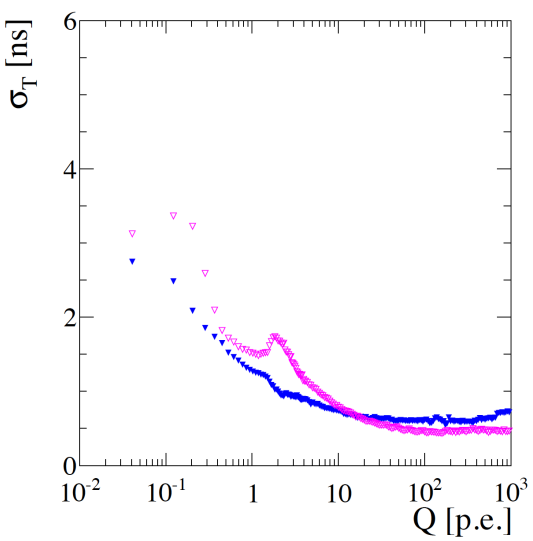

(b) The timing resolution of Hyper-K PMTs

Figure 6.4: The timing resolution of Super-K and Hyper-K PMTs with respect to charge Q in PE.

$$f(t) = \begin{cases} \sqrt{\frac{2}{\pi(\sigma_1+\sigma_2)^2}}\exp\left(-\frac{(t-t_0)^2}{2\sigma_1^2}\right) & (t < t_0) \\ \sqrt{\frac{2}{\pi(\sigma_1+\sigma_2)^2}}\exp\left(-\frac{(t-t_0)^2}{2\sigma_2^2}\right) & (t \geq t_0) \end{cases} \tag{6.3}$$

where t_0 is the injection time of a photon into a PMT. To verify the validity of the new timing resolutions for SK-V environment, the MC simulated events will be compared to various data samples including the LINAC and the thru-going cosmic muons. On the other hand, due to a discrepancy between the MC and LINAC event in the timing of low charge hits, some fitting method other than Eq. 6.2 to generate the timing resolution parameters is also under studies. These tests are expected to be done after when the upgrades of LINAC and SKDETSIM are finished.

7 Conclusions and Outlook

In the year 2018-19, Super-K has completed a full scale detector upgrade to SK-V. A variety of refurbishments were done, for example, a new water cycling system was installed in parallel to the existing one. This new system will be used to add Gd into the Super-K tank in a year or two. Regarding this work, many improvements and updates were made to the ID PMTs, among which were the 136 50 cm Hyper-K B&L PMTs used to replace the dead channels from SK-IV. Before the installation, each Hyper-K tube was checked carefully in an underground laboratory neighboring the Super-K tank. Those PMTs were

confirmed to be of good quality by the measurement done in the air. The charge and timing resolutions of Hyper-K PMTs were roughly twice as good as that of Super-K ones. Meanwhile the measurements after installation in Super-K water also verified this. This result and the future data of Hyper-K PMTs will serve a critical role in realizing the upcoming Hyper-K project.

The 2 major calibration tasks done by this work are the adjustment of all ID PMTs' voltages and the new correction table of relative timing difference in each ID PMT channel. Throughout the SK-IV running phase, it was noticed that the average gain of ID PMTs continuously drifted up. Meanwhile the gain increment varied among individual PMTs, which resulted a larger spread in the PMT charge responses. To correct this systematic uncertainty, the new voltages targeting at the SK-III initial gain of 1.65×10^7 was determined by a voltage scan for each PMT using a laser diode at the center of the tank. At each voltage in the scan, the SPE charge peak of each PMT was fitted. It was the first time in Super-K that the SPE charge peak of each individual PMT's is used to determine the voltage setting. Such a method is independent of the water quality and has less bias from the occasional multi-PE signal contamination. After the adjustment, the Super-K ID gain average has decreased down to 1.70×10^7, which is $\sim$85.6% of the gain before adjustment. The $\sim$3% offset in gain average from the target value was due to the uncertainty when converting the ADC count into charges, which resulted in a slightly insufficient adjustment. On the other hand, the spread among ID PMTs has decreased from 12% to 4% of the average value. The remaining 4% individual difference comes from the systematic and statistical error in the voltage curve fitting, which was on average 5.07% and 2.58% respectively. Nevertheless, the real gain and individual difference of each ID PMT were further measured by some other works and will be taken into account in the data reduction and analyses of Super-K.

The relative timing difference in each ID PMT mainly comes from the electronics processing time. Meanwhile the PMT time response is different by signal strengths, which is known as the time walk effect. These 2 systematic uncertainties were corrected by the T-Q curves. To generate a T-Q curve, a laser source was enlightened at the tank center and the timing of each PMT at a certain charge in the range of 0$\sim$3981 pC was fitted. Then in total $\sim$180 of such points were used to find the relation between PMT's charge and timing, or so-called T-Q curve. By applying the T-Q correction, the PMT's timing of an event free of the time walk effect can be predicted from its charge. Meanwhile the difference in electronics processing time was also measured and corrected by calculating the time lag between the laser flash and PMT hits. Moreover, the detector timing resolu-

tion was also calculated from the T-Q curve corrected laser data. Super-K and Hyper-K PMTs were treated separately this time. In the case of Super-K PMTs, the new timing resolution is roughly equivalent to the previous value in SK-IV. However since the voltage setting has been decreased, the detector timing resolution is effectively improved.

With a lower average voltage, the ID PMTs are expected to have lower dark hit rate that strongly affect the study of low energy physics. There lies a possibility that Super-K may lower its energy threshold, which improves its sensitivity to multiple target particles such as solar and supernova neutrinos. At the mean time, the data collected during this calibration will be used to update SKDETSIM to SK-V environment, which helps to improve the physics event reconstruction and neutrino oscillation analyses. Last but no the least, the calibration framework and software developed this time will be a great sample for the upcoming calibration of SK-Gd phase, which will happen in 1$\sim$2 years. All of these updates and improvements combined together will help to evolve this 20-year-long experiment to a higher stage of physics studies.

References

[1] K. Hirata, T. Kajita, M. Koshiba, et al. Observation of a neutrino burst from the supernova sn1987a. *Phys. Rev. Lett.*, 58:1490–1493, Apr 1987.

[2] Y. Fukuda, T. Hayakawa, E. Ichihara, et al. Evidence for oscillation of atmospheric neutrinos. *Phys. Rev. Lett.*, 81:1562–1567, Aug 1998.

[3] Q. R. Ahmad, R. C. Allen, T. C. Andersen, et al. Measurement of the rate of $\nu_e + d \rightarrow p + p + e^-$ interactions produced by ^8b solar neutrinos at the sudbury neutrino observatory. *Phys. Rev. Lett.*, 87:071301, Jul 2001.

[4] Carlo Giunti and Chung W. Kim. *Fundamentals of Neutrino Physics and Astrophysics*. Oxford University Press, 2007.

[5] Mark Srednicki. *Quantum Field Theory*. Cambridge University Press, 2007.

[6] Mark Thomson. *Modern Particle Physics*. Cambridge University Press, 2013.

[7] The standard model of elementary particles. `https://en.wikipedia.org/wiki/File:Standard_Model_of_Elementary_Particles.svg`. Accessed: 2019-06-01.

[8] V. Castellani, S. Degl'Innocenti, G. Fiorentini, M. Lissia, and B. Ricci. Solar neutrinos: beyond standard solar models. *Physics Reports*, 281(5):309 – 398, 1997.

[9] M. Tanabashi, K. Hagiwara, K. Hikasa, et al. Review of particle physics. *Phys. Rev. D*, 98:030001, Aug 2018.

[10] Xiaoyue Li. *A Joint Analysis of T2K Beam Neutrino and Super-Kamiokande Sub-GeV Atmospheric Neutrino Data*. PhD thesis, SUNY, Stony Brook, 2018.

[11] K. Abe, R. Akutsu, A. Ali, et al. Search for *cp* violation in neutrino and antineutrino oscillations by the t2k experiment with 2.2×10^{21} protons on target. *Phys. Rev. Lett.*, 121:171802, Oct 2018.

[12] Y. Fukuda et al. The Super-Kamiokande detector. *Nucl. Instrum. Meth.*, A501:418–462, 2003.

[13] Pablo Fernandez Menendez. *Neutrino Physics in Present and Future Kamioka Water-Cherenkov Detectors with Neutron Tagging*. PhD thesis, University Autonomous of Madrid, 2017.

[14] Albert Einstein. On the electrodynamics of moving bodies. *Annalen Phys.*, 17:891–921, 1905. [Annalen Phys.14,194(2005)].

[15] O. Heaviside. *Electromagnetic Theory*, volume 2. Cosimo, Incorporated, 2007.

[16] P. A. Čerenkov. Visible radiation produced by electrons moving in a medium with velocities exceeding that of light. *Phys. Rev.*, 52:378–379, Aug 1937.

[17] Cherenkov radiation as a light cone. `https://en.wikipedia.org/wiki/File:Cherenkov.svg`. Accessed: 2019-06-03.

[18] A. Suzuki, M. Mori, K. Kaneyuki, et al. Improvement of 20 in. diameter photomultiplier tubes. *Nuclear Instruments and Methods in Physics Research Section A: Accelerators, Spectrometers, Detectors and Associated Equipment*, 329(1):299 – 313, 1993.

[19] K. Abe et al. Calibration of the Super-Kamiokande Detector. *Nucl. Instrum. Meth.*, A737:253–272, 2014.

[20] S. Yamada, K. Awai, Y. Hayato, et al. Commissioning of the new electronics and online system for the super-kamiokande experiment. *IEEE Transactions on Nuclear Science*, 57(2):428–432, April 2010.

[21] K. Abe et al. Hyper-Kamiokande Design Report. 2018.

[22] J. Xia et al. The Initial Calibration of the New Super-Kamiokande Inner Photodetectors in the Year 2018-2019. Japan Physics Society Conference (Spring), 2019.

[23] T. Mochizuki. Development of 50 cm Diameter Photomultiplier Tubes and a Neutron Tagging Algorithm for Hyper-Kamiokande. Master's thesis, University of Tokyo, 2019.

[24] J. Xia, Y. Nishimura, C. Bronner, and T. Mochizuki. The Calibration and Evaluation of 140 20-inch Box and Line Photomultiplier Tubes Designed for Hyper-Kamiokande. Proceedings of the 5th International Photo-detector Workshop, in preparation, 2019.

[25] Y. Heng. A Direct Search for Weakly Interacting Massive Particles in the Super-Kamiokande Experiment. Master's thesis, Tsinghua University, 2010.

[26] W. R. Leo. *Techniques for Nuclear and Particle Physics Experiments: A How to Approach*. 1987.